

EMPLOYING SURFACE PLASMON RESONANCES TO BOOST EFFECTIVENESS
OF MULTIPLE EXCITON GENERATION IN LEAD-BASED QUANTUM DOTS

by

Kathleen Mary Dipple

A dissertation submitted to the faculty of
The University of North Carolina at Charlotte
in partial fulfillment of the requirements
for the degree of Doctor of Philosophy in
Nanoscale Science

Charlotte

2019

Approved by:

Dr. Thomas A. Schmedake

Dr. Marcus Jones

Dr. Christopher Bejger

Dr. Haitao Zhang

Dr. Yuri E. Nesmelov

©2019
Kathleen Mary Dipple
ALL RIGHTS RESERVED

ABSTRACT

KATHLEEN MARY DIPPLE. Employing Surface Plasmon Resonances to Boost Effectiveness of Multiple Exciton Generation in Lead-Based Quantum Dots. (Under the direction of DR. THOMAS A. SCHMEDAKE)

Harvesting the sun's energy at a high efficiency and low cost is a vital step towards replacing fossil fuels. Colloidal quantum dots (QDs) are promising materials that have great potential for solar applications due to their size dependent optical properties and high-absorption cross-sections.¹ Lead-chalcogenide QDs can be tuned so that their band gap is close to optimal for light absorber in a single junction solar cell. Moreover, these near IR-absorbing QDs can generate multiple excitons after absorption of a suitably energetic photon, enabling external quantum efficiencies in excess of 100 % EQE for blue and UV light.²

Light harvesting is most efficient for optically thick materials that are physically thin. That way, all incoming light is absorbed, and the resulting excitons and charge carriers do not have far to travel to reach an electrode. In addition, for cells that utilize multiple exciton generation, it is critical that they absorb as much UV and blue light as possible. One way to boost the optical density of QD solar cells is to take advantage of the optical antenna effect of plasmonic metal nanoparticles (NPs). These NPs support surface plasmon resonances that generate very large local electric fields and increase photo-absorption in nearby chromophores.

The goal of this work, was to take advantage of this effect to demonstrate increased light absorption in QDs, especially above the energy threshold for multiple

exciton generation (MEG). My principal aim has been to unravel the factors that control the coupling between QD excitons and plasmon resonances in Ag NPs by controlling the size and shape of the NPs as well as the interaction distance between NPs and QDs (Figure 1). I observed energy transfer between NPs and QDs using time-resolved and steady state photoluminescence studies, and, ultimately, demonstrated that Ag NPs could effectively increase QD photoabsorption for photons with energies both above and below the MEG threshold. This is a vital step toward enhancing QD solar cells and boosting the importance of MEG in metal-coupled QD systems. This research is important for the development of low cost, high efficiency solar cells in addition to a wide range of optoelectronic applications.

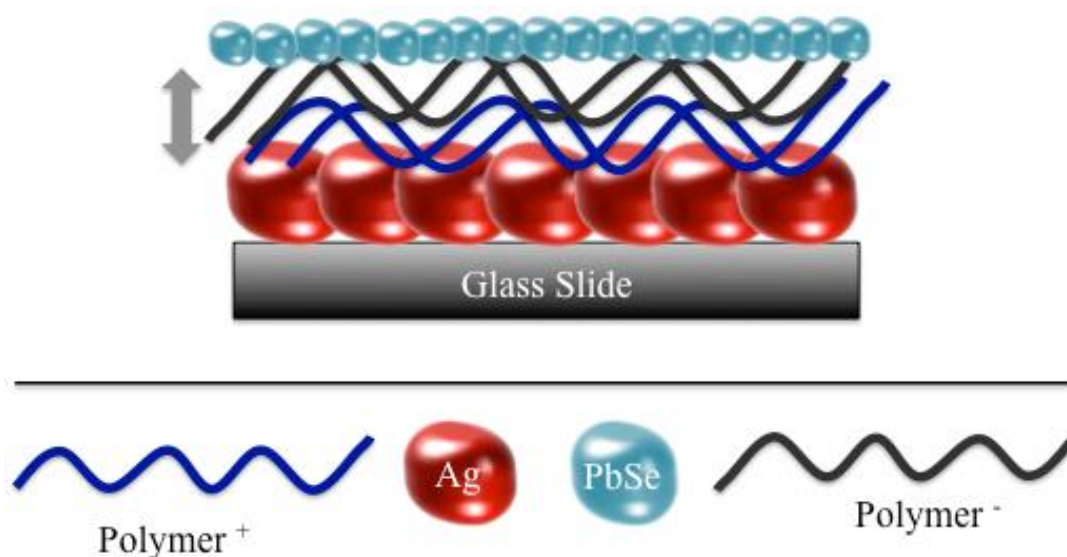


Figure 1: Layered approach to studying SPR effect on PbSe QD emission. The blue and black lines represent the positively and negatively charged polymer spacer layers, respectively. The red and blue spheres represent silver nanoparticles and lead selenide quantum dots, respectively. The double-sided arrow represents the changing of polymer spacer thicknesses.

DEDICATION

I dedicate this to my amazing and loving parents, Jennifer and Sean Dipple. To my sisters Kelsey Dipple and Margaret Cronkhite. Their love and support along the way has helped me tremendously. I would also like to mention my nephew, A. J. Cronkhite. He was born during my studies here at UNC Charlotte (July 6, 2017) and has brought immense joy into my life ever since.

ACKNOWLEDGEMENTS

I would first like to acknowledge my Ph. D. advisor, Dr. Marcus Jones. I have progressed so much as a scientist and I have become a stronger person because of his mentorship. I truly appreciate his close attention to detail, high standards for science, integrity, and his passion to teach others. He encouraged and allowed me to do research alongside another graduate student and Charlotte Mecklenburg School Teachers on their own projects for two summers. My passion for scientific outreach and scientific communication skills grew so much stronger from that experience. He trusted me as a leader of our wet chemistry lab, laser lab and numerous undergraduates. His trust and mentorship have allowed me to grow more than I ever thought possible. Even though he had to relocate to New Zealand, he always made sure that I had all the support that I needed during my last year. I would also like to thank my committee members: Dr. Thomas A. Schmedake, Dr. Christopher Bejger, Dr. Haitao Zhang and Dr. Yuri A. Nesmelov for taking the time to learn about my project and offer any help that I may need.

I would like to especially thank Andrew (Drew) Tobias for being a close friend and a mentor for many years. He started as my mentor when I was an undergraduate NanoSure REU student back in 2012, and he has continued in that role while I was in graduate school. Even though he has graduated years ago, we still talk about science and life regularly. I will forever be grateful for Drew's research feedback when I needed it. Other previous members of the Marcus Jones group have also helped me with regards to

science and by being great friends: Gaurav Singh, Jose Castaneda, and Danielle Wooddall.

I would like to thank individuals in the UNC Charlotte Chemistry department. Dr. Jon Merkert was always willing to make time to help me with any instrumentation or equipment problem that I had. He always made a point to teach me about the problem or how he was fixing something. He is a funny and kind person and I have learned a lot from him. I would like to thank Dr. Bernadette Donovan-Merkert for being there for me when I needed letters of reference and support for my research. Thank you, Vladimir Kubalik, for fixing various electronics in our lab. I would like to thank Linda Spurrier for always ordering our supplies right away and all the great conversations that we had in her office before she retired. You made me laugh often and it always meant a lot to me. I would like to thank the people in the front office who always made sure that my academic needs were met: Nancy Queen, Rebecca Hawes, Deborah Howard, Lisa Carlin, Robin Burns, and Caroline Kennedy. I would like to thank Dr. Terry Xu in Engineering for allowing me to use the TEM anytime I needed to.

I would like to thank my best friend, Jay Voorhies who was always there to take my mind off research and stresses when I needed him. My girlfriend, Kenia Rios has been a huge source of support for me since the day I have met her.

Lastly, I would like to thank my family again. Thank you for always making me laugh, smile, and realize life is so much more than work. Shawny has never hesitated to support me, let me live in his house, and even gave me a summer job when I needed it. I will always be grateful for that. Lara Smith, thank you for always being there for me to

talk to when I needed. My family has always believed in me and I would not have been able to complete this degree without their love and support.

TABLE OF CONTENTS

LIST OF TABLES	xii
LIST OF FIGURES	xiii
LIST OF ABBREVIATIONS	xxix
SECTION 1 INTRODUCTION	1
CHAPTER 1.1 WHY RESEARCH SOLAR ENERGY?	2
1.1.1 Current state-of-the-art	2
1.1.1.2 Silicon Solar Cells	3
1.1.1.3 Perovskite Solar Cells	5
1.1.1.4 Polycrystalline Thin Film Solar Cells	8
1.1.1.5 Why are we interested in QDs for Solar Cells?	11
1.1.2 Research in the Past 10 Years	12
CHAPTER 1.2 HOW CAN WE UTILIZE MORE OF THE SOLAR SPECTRUM?	14
1.2.1 Near-Infrared Quantum Dots (Near IR QDs)	15
1.2.2 Lead Selenide Quantum Dots (PbSe QDs)	15
1.2.3 Lead Sulfide Quantum Dots (PbS QDs)	16
1.2.4 PbSe QDs versus PbS QDs	18
CHAPTER 1.3 CORE/SHELL QDs	20
1.3.1 PbSe/CdSe Core/Shell QDs	21
1.3.1.1 Fabricating PbSe/CdSe QDs	23
1.3.1.1.1 Determining the Optimal CdSe Shell Thickness	27
CHAPTER 1.4 HOW CAN WE EXCEED THE SHOCKLEY-QUEISSER LIMIT?	29

	x
1.4.1 Multiple Exciton Generation (MEG)	29
1.4.1.1 Possible Quantum Mechanisms of MEG	31
1.4.1.2 MEG in PbSe QDs	33
CHAPTER 1.5 HOW CAN WE IMPROVE SOLAR CELL EFFICIENCY WITH MEG?	35
1.5.1 Boosting MEG with Nanoparticle (NP) Confinement	35
CHAPTER 1.6 CAN WE INCREASE LIGHT ABSORPTION ABOVE THE MEG THRESHOLD?	37
1.6.1 Metallic NPs and Surface Plasmon Resonances (SPRs)	37
1.6.2 Purcell Effect	42
1.6.3 Increasing the Optical Path Length with SPR Light Scattering	43
1.6.4 Coupling of Metal Nanoparticles to Quantum Dots	45
1.6.4.1 Role of NP Scattering Efficiency in QD Absorption Enhancement	46
1.6.4.2 Silver: The Best Nanoparticle for the Job	47
1.6.4.3 SPR Effects on Fluorophores Lifetime	48
1.6.5 Plasmonic Enhanced Multiple Exciton Generation	50
CHAPTER 1.7 SUMMATION/RESEARCH AIMS	51
SECTION 2 RESEARCH	52
CHAPTER 2.1 OVERALL GOALS	53
2.1.1 Mechanism of Plasmonic MEG Enhancement	54
2.1.2 Two Approaches	57
CHAPTER 2.2 PROJECT I: HYBRID CORE/SHELL/SHELL NPS	59

	xi
2.2.1 Synthesis and Characterization of Core/Shell/Shell Hybrid NPs	61
2.2.2 Effects of Lattice Strain on the Photoluminescence of PbX (X = S or Se)	73
CHAPTER 2.3 PROJECT II: LAYERED THIN FILMS	75
2.3.1 Introduction to Facile Synthesis of Highly Loaded Silver NP Films with Tunable Scattering	76
2.3.2 Tuning Silver NP Synthesis	76
2.3.3 Applying and Characterizing Silver NP Monolayer Films	82
2.3.3.1 Photoaging of Silver Nanoparticles	84
2.3.3.2 Scattering and Absorbance of Silver NP Films	85
2.3.3.3 Optical SPR Dependence on Interparticle Spacing	91
2.3.4 Applying Dielectric Spacer and Determining Thicknesses	96
2.3.5 Air Stable PbSe QD Synthesis for Films	101
2.3.6 Complete Film Series Study Example	105
2.3.6.1 Integrating Sphere Experiments	107
2.3.6.2 Steady State Emission	124
2.3.6.3 Photoluminescence Excitation Studies	126
2.3.6.4 Time Resolved Photoluminescence Studies	132
2.3.7 Excitation Enhancement Calculations	134
CHAPTER 2.4 SUMMARY/CONCLUSIONS	141
CHAPTER 2.5 FUTURE WORK	143
2.5.1 Measure Biexciton Lifetimes	143
REFERENCES	14

LIST OF TABLES

TABLE 1: Most Recent (2019) Reported Solar Cell/Module Efficiencies Measured Under the Global Air Mass 1.5 Spectrum (1000 Wm^{-2}) at 25°C	3
TABLE 2: QD film series sample details. The sample names and corresponding layer contents are shown in the table. The blue sample labels represent the control samples since no silver monolayer is present, only PbSe QDs on glass or polymer layers.	101

LIST OF FIGURES

- FIGURE 1: Layered approach to studying SPR effect on PbSe QD emission. The blue and black lines represent the positively and negatively charged polymer spacer layers, respectively. The red and blue spheres represent silver nanoparticles and lead selenide quantum dots, respectively. The double-sided arrow represents the changing of polymer spacer thicknesses. iv
- FIGURE 2: Schematic of the highly efficient Perovskite solar cell. The grey, light green, and dark green spheres represent lead atoms, methylammonium ions, and iodine atoms, respectively. The arrows represent the one-step charge carrier generation.²¹ From [Collavini, S.; Volker, S. F.; Delgado, J. L., Understanding the Outstanding Power Conversion Efficiency of Perovskite-Based Solar Cells. *Angewandte Chemie International Edition* 2015, 54 (34), 9757-9759.] Reprinted with permission from John Wiley and Sons. 5
- FIGURE 3: Perovskite device with a >19 % power conversion efficiency. A) labeled SEM cross-section of perovskite solar device B) Energy level diagram (relative to vacuum) of each layer of device From [Zhou, H. P.; Chen, Q.; Li, G.; Luo, S.; Song, T. B.; Duan, H. S.; Hong, Z. R.; You, J. B.; Liu, Y. S.; Yang, Y., Interface engineering of highly efficient perovskite solar cells. *Science* 2014, 345 (6196), 542-546.] Reprinted with permission from AAAS. A) SEM cross-section of perovskite solar device with efficiency of > 19 % B) Energy level diagram (relative to vacuum) of each layer of device 6
- FIGURE 4: Hysteresis in current density versus voltage curve of planar heterojunction perovskite solar cell (shown in Figure 2) under AM 1.5, 100 mWcm⁻². The black and red curves represent the forward and reverse directions, respectively. ²⁴ From [Zhou, H. P.; Chen, Q.; Li, G.; Luo, S.; Song, T. B.; Duan, H. S.; Hong, Z. R.; You, J. B.; Liu, Y. S.; Yang, Y., Interface engineering of highly efficient perovskite solar cells. *Science* 2014, 345 (6196), 542-546.] Reprinted with permission from AAAS. 7
- FIGURE 5: Perovskite stability study of non-encapsulated perovskite solar cells in ambient air, dry air, and N₂ atmosphere (10 devices were 8

studied per condition) over 6 days. The black, red, and blue curves represent devices in ambient air, dry air, and nitrogen gas, respectively. From [Zhou, H. P.; Chen, Q.; Li, G.; Luo, S.; Song, T. B.; Duan, H. S.; Hong, Z. R.; You, J. B.; Liu, Y. S.; Yang, Y., Interface engineering of highly efficient perovskite solar cells. *Science* 2014, 345 (6196), 542-546.] Reprinted with permission from AAAS.

FIGURE 6: Schematic of a layered, CdS/CdTe thin film solar cell. Reprinted from *Solar Energy* 2004, 77 (6), Ferekides, C. S.; Balasubramanian, U.; Mamazza, R.; Viswanathan, V.; Zhao, H.; Morel, D. L., CdTe thin film solar cells: device and technology issues. 823-830. Copyright (2004), with permissions from Elsevier. 10

FIGURE 7: Trends in solar: number of records versus publication year of various topics in solar (per Web of Science). The blue, black, red, yellow, green, and purple curves represent the number of publication records in silicon, quantum dot, polymer, perovskite, CIGS, and plasmonic solar versus year, respectively. 13

FIGURE 8: Solar energy absorbed (red) by a 2 μm thick Si wafer (assuming no reflection) versus solar spectrum at air mass 1.5 (blue). The inset reveals the relative depth that certain colors of light make it through a Si device. Reprinted by permission from [Atwater, H. A.; Polman, A., Plasmonics for improved photovoltaic devices. *Nature Materials* 2010, 9 (3), 205-213.] [COPYRIGHT] (2010). 14

FIGURE 9: Absorbance (solid), steady state emission (dashed), and time resolved lifetime decay (inset) of PbSe QDs ($E_g = 0.88 \mu\text{s}$) Reprinted (adapted) with permission from (Wehrenberg, B. L.; Wang, C. J.; Guyot-Sionnest, P., Interband and intraband optical studies of PbSe colloidal quantum dots. *Journal of Physical Chemistry B* 2002, 106 (41), 10634-10640.). Copyright (2002) American Chemical Society. 16

FIGURE 10: Normalized absorbance spectra of a PbS QD series with E_g ranging from 970-1740 nm (red-black curves). There is an absorbance peak red shift with increasing QD size due to the quantum confinement effects.³ Reprinted (adapted) with permission from (Moreels, I.; Lambert, K.; Smeets, D.; De Muynck, D.; Nollet, T.; Martins, J. C.; Vanhaecke, F.; Vantomme, A.; Delerue, C.; Allan, G.; Hens, Z., Size-Dependent Optical Properties of Colloidal PbS Quantum 17

Dots. *ACS Nano* 2009, 3 (10), 3023-3030.) Copyright (2009) American Chemical Society.

FIGURE 11: Published (red and solid black), and tight binding calculations (open black diamond) of PbS E_g versus particle size relationship. The dotted line is the bulk E_g (0.41 eV). Reprinted (adapted) with permission from (Moreels, I.; Lambert, K.; Smeets, D.; De Muynck, D.; Nollet, T.; Martins, J. C.; Vanhaecke, F.; Vantomme, A.; Delerue, C.; Allan, G.; Hens, Z., Size-Dependent Optical Properties of Colloidal PbS Quantum Dots. *ACS Nano* 2009, 3 (10), 3023-3030.) Copyright (2009) American Chemical Society. 18

FIGURE 12: Calculated (solid markers) and experimental (open markers) relationship between oscillator strength and particle size of PbS (black) versus PbSe (red). Overall, lead selenide QDs have a greater oscillator strength than lead sulfide. Reprinted (adapted) with permission from (Moreels, I.; Lambert, K.; Smeets, D.; De Muynck, D.; Nollet, T.; Martins, J. C.; Vanhaecke, F.; Vantomme, A.; Delerue, C.; Allan, G.; Hens, Z., Size-Dependent Optical Properties of Colloidal PbS Quantum Dots. *ACS Nano* 2009, 3 (10), 3023-3030.) Copyright (2009) American Chemical Society. 19

FIGURE 13: Types of core/shell heterostructures with the corresponding electron and hole wave-function distributions below. The quasi-type-II core/shell structures have wavefunctions more promising for charge separation. Reprinted (adapted) with permission from (Zaiats, G.; Yanover, D.; Vaxenburg, R.; Tilchin, J.; Sashchiuk, A.; Lifshitz, E., PbSe-Based Colloidal Core/Shell Heterostructures for Optoelectronic Applications. *Materials* 2014, 7 (11), 7243-7275.) Copyright (2014) MDPI. 20

FIGURE 14: Effective electron (black) and hole (red) masses and energy bands versus radial coordinate in PbSe/CdSe core/shell QDs generated by using the FEA software (COMSOL). The valence and conduction band energies change from the core to the shell. Reprinted (adapted) with permission from (Zaiats, G.; Yanover, D.; Vaxenburg, R.; Tilchin, J.; Sashchiuk, A.; Lifshitz, E., PbSe-Based Colloidal Core/Shell Heterostructures for Optoelectronic Applications. *Materials* 2014, 7 (11), 7243-7275.) Copyright (2014) MDPI. 22

- FIGURE 15: Zoomed out (A) and in (B) TEM image of PbSe QDs taken 954 seconds after hot injection. The scale bar in A) and B) are 100 and 5 nm, respectively. Here, the average QD diameter is approximately 5 nm. A) reveals the monodisperse size distribution. In image B), the lattice fringes and crystallinity of the two quantum dots are clear. 23
- FIGURE 16: Absorbance versus wavelength, nm of PbSe QDs (black) and near IR dye (IR1061) standard (blue). The absorbance peaks of the two samples are very similar in wavelength. The IR1061 dye was used to determine the relative quantum yield of the QDs. 24
- FIGURE 17: Calculated quantum yield of PbSe QDs taken out at various times after the hot injection. The x-axis represents the PbSe QD synthesis time in seconds. In every case, the reaction was quenched by a rapid injection of a cold solvent mixture. 25
- FIGURE 18: Normalized absorbance of PbSe/CdSe QDs taken during the cation exchange reaction between lead and cadmium. The PbSe core only sample is shown in red. The times correspond to exposure time to the cadmium oleate solution. The increase in the reaction time (black to light blue) means an increase in the lead and cadmium cation exchange and thus the increase in the CdSe shell growth. 26
- FIGURE 19: Calculated relative QY versus CdSe shell growth time at 625 nm excitation ($1.5E_g$) as the PbSe/CdSe QDs age in air for 0 weeks (black), 1 week (blue) and 2 weeks (red). Larger CdSe shells (longer growth times) have greater quantum yields. 27
- FIGURE 20: TEM and EDX elemental analysis of PbSe/CdSe core/shell QDs (60 min shell growth). In the TEM image, the scale bar is 5 nm and the yellow rectangle represents the area which the energy dispersive x-ray (EDX) elemental analysis was taken on. The copper, silicon, chromium, carbon, oxygen and chlorine signals arise from the sample grid and detector. 28
- FIGURE 21: A) Impact ionization, B) Auger recombination, C) dynamic carrier populations following the excitation of PbSe QDs with photon of energy $> 3 E_g$. Filled and open red circles represent electrons and holes, respectively. C and V represent the 32

conduction and valence bands. η_x and η_{xx} represent the fraction of the population that generate single excitons, and undergo II to generate biexciton, respectively D) dynamics schematic of time resolved data blue trace (excitation above MEG threshold) red trace (excitation below MEG threshold. Reprinted (figure) with permission from (Schaller, R. D.; Klimov, V. I., High efficiency carrier multiplication in PbSe nanocrystals: Implications for solar energy conversion. *Physical Review Letters* 2004, 92 (18), 4.) Copyright (2004) by the American Physical Society.

FIGURE 22: Incoherent multiple exciton generation model in PbSe QDs at 3Eg excitation energy.2 Reprinted (adapted) with permission from (Ellingson, R. J.; Beard, M. C.; Johnson, J. C.; Yu, P. R.; Micic, O. I.; Nozik, A. J.; Shabaev, A.; Efros, A. L., Highly efficient multiple exciton generation in colloidal PbSe and PbS quantum dots. *Nano Letters* 2005, 5 (5), 865-871). Copyright (2005) American Chemical Society. 33

FIGURE 23: MEG in PbSe nanorods (red curve) and QDs (black curve); QY versus excitation energy. The horizontal dashed line represents where the NPs exhibit a 100 % QY. Anything above that line represents MEG. The point at which the energy (x-axis) and the dotted line intersect represents the minimum threshold energy for MEG to occur. Reprinted (adapted) with permission from (Cunningham, P. D.; Boercker, J. E.; Foos, E. E.; Lumb, M. P.; Smith, A. R.; Tischler, J. G.; Melinger, J. S., Enhanced Multiple Exciton Generation in Quasi-One-Dimensional Semiconductors. *Nano Letters* 2011, 11 (8), 3476-3481) Copyright (2011) American Chemical Society. 36

FIGURE 24: Illustration of a surface plasmon resonance for a spherical nanoparticle where electron charge is displaced. The red curve represents the strong localized electric field caused by the coherent oscillation of electrons. The grey and green spheres represent the metal NP and electron cloud, respectively. Reprinted (adapted) with permission from (Kelly, K. L.; Coronado, E.; Zhao, L. L.; Schatz, G. C., The optical properties of metal nanoparticles: The influence of size, shape, and dielectric environment. *Journal of Physical Chemistry B* 2003, 107 (3), 668-677). Copyright (2003) American Chemical Society. 38

FIGURE 25: Mie theory calculated electric field contours of 30 nm (A and C) and 60 nm (B and D) Ag spheres with 369 nm and 358 nm 39

light, respectively. The different colors (blue to red) represent an increase in electric field strength.⁴ Reprinted (adapted) with permission from (Kelly, K. L.; Coronado, E.; Zhao, L. L.; Schatz, G. C., The optical properties of metal nanoparticles: The influence of size, shape, and dielectric environment. *Journal of Physical Chemistry B* 2003, 107 (3), 668-677). Copyright (2003) American Chemical Society.

FIGURE 26: Configuration of Smill-Purcell experiment. The lower area represents a grating with a periodicity of D . The arrows represent the path of an electron (e^-) traveling at velocity, V and at an angle, ψ across the grating. Reprinted from Haerberle, O., Reciprocity theorem for Smith-Purcell radiation. *Optics Communications* 1997, 141 (5-6), 237-242. Copyright (1997), with permission from Elsevier. 42

FIGURE 27: Light trapping geometry of plasmonic nanoparticles (grey sphere) in a layered (glue and orange) thin film solar cell. The arrows represent the path of the incident light. The presence of metal nanoparticles caused an increase in optical pathlength through the device. Reprinted by permission from [Atwater, H. A.; Polman, A., Plasmonics for improved photovoltaic devices. *Nature Materials* 2010, 9 (3), 205-213.] [COPYRIGHT] (2010). 44

FIGURE 28: A) External quantum efficiency enhancements of Si wafers due to the presence of 50 nm Ag nanoparticles for samples with different top layers: SiO₂ on sample A, Si₃N₄ on sample B, and TiO₂ on sample C. The solid curves represent when the samples were irradiated from the front and the dashed were irradiated from the rear.¹⁴² Reprinted from [Beck, F. J.; Polman, A.; Catchpole, K. R., Tunable light trapping for solar cells using localized surface plasmons. *Journal of Applied Physics* 2009, 105 (11)], with the permission of AIP Publishing. 44

FIGURE 29: TCSPC curve of a single molecule fluorophore a) near Ag metal nano-shell versus b) on glass alone and corresponding histograms of decay times (c-d). Reproduced from Fu, Y.; Zhang, J.; Lakowicz, J. R., Large enhancement of single molecule fluorescence by coupling to hollow silver nanoshells. *Chemical Communications* 2012, 48 (78), 9726-9728. with permission from the Royal Society of Chemistry. 50

FIGURE 30: Comparison of silicon absorption (black line) to our system (PbSe QDs and Au) and the spectral irradiance at air mass 1.5 global (green curve) versus wavelength (nm). The dark blue range represents the range that PbSe QDs bandgap can be tuned to absorb. PbSe QDs have the potential to absorb more of the solar spectrum than conventional silicon can. The light blue range represents the energies that are suitable for MEG in PbSe QDs. There are plenty of photons from the sun (green curve) with energies suitable to generation multiple excitons in PbSe QDs. The red curve represents the Mie theorized absorbance of 50 nm diameter silver nanoparticles. The red curve is to show that the surface plasmon resonance of silver NPs can boost absorption rates in the QDs; even above the MEG threshold.

54

FIGURE 31: Potential Effect of SPRs on e⁻ and h⁺ generation after MEG. Number of charge carriers per absorbed photon versus proportion of photons above MEG threshold. The red and blue curves represent MEG in QDs alone and MEG in QDs when a surface plasmon resonance is present, respectively.

57

FIGURE 32: The two approaches to employ surface plasmon resonances to boost effectiveness of MEG in lead-based quantum dots: one colloidal and one layered. The left portion of the figure represents the colloidal, hybrid core/shell/shell approach. There is a metal core (red) with a wide bandgap shell (purple) and a near IR outer shell (blue). The right portion represents the layered approach where a monolayer of silver nanoparticles is separated from PbSe QDs by charged polymer spacer layers of varying thicknesses.

59

FIGURE 33: Schematic of rationale of our hybrid Au/CdX/PbX (X = S or Se) NPs. The hybrid NP includes Au (red circle), a CdX layer (purple), and a PbX layer (teal). The idea is to use the MEG and near IR absorption capabilities of the PbX layer along with the surface plasmon resonance modes of the metal nanoparticle. The idea is to boost the absorption and possibly MEG of the PbX layer with the SPR of the metal. The wide bandgap spacer (purple = CdX) was placed to minimize energy loss into the metal.

60

FIGURE 34: Vital aspects to ensure that this approach worked. The wide bandgap spacer (purple = CdX) was placed to minimize energy loss into the metal. We chose a non-epitaxial growth mechanism of the core/shell/shell NPs to minimize the defects that act as trap states.

61

- FIGURE 35: TEM image of cetyltrimethylammonium chloride coated gold nanoparticles. The scale bar is 5 nm and the image is of two NPs stuck together. The atomic lattice and the facets of the Au NPs are clearly visible. 63
- FIGURE 36: Absorption versus wavelength of gold nanoparticles as growth of a 20 nm thick silver shell proceeds (red to purple). The black curve represents the absorbance of gold nanoparticles before the reaction occurs. As the Ag shell growth proceeds (red to purple) in time, the spectrum shifts and begins to look like the characteristic silver NP plasmon alone. 64
- FIGURE 37: A) TEM and B) EDX elemental analysis of a single Au/CdSe hybrid nanoparticle. In the TEM image, the scale bar is 10 nm and the yellow rectangle represents the area which the energy dispersive x-ray (EDX) elemental analysis was taken on. The copper, silicon, chromium, carbon, oxygen and chlorine signals arise from the sample grid and detector. 67
- FIGURE 38: Absorbance changes versus wavelength of Au/CdS hybrid nanoparticles during “cation exchange” using exposure to lead oleate. The absorbance of the initial Au/CdS nanoparticles is shown in black. The blue and red curves show the absorbance as the cation exchange reaction proceeds for 4 and 15 hours, respectively. 70
- FIGURE 39: A) TEM and B) EDX elemental analysis of Au/CdS/PbS after 15 hr exposure to Pb oleate. In the TEM image, the scale bar is 20 nm and the yellow rectangle represents the area which the energy dispersive x-ray (EDX) elemental analysis was taken on. The copper, silicon, chromium, carbon, oxygen and chlorine signals arise from the sample grid and detector. The atomic % of lead and cadmium present in the yellow area were 1.84 and 4.96 %, respectively. 72
- FIGURE 40: Absorbance changes versus wavelength of Au/CdS hybrid nanoparticles during “cation exchange” using exposure to lead nitrate with tributylphosphine as a transport agent. The absorbance of the initial Au/CdS nanoparticles is shown in black. The red curve shows the absorbance as the cation exchange reaction proceeded for 3 hours. The grey curve shows the absorbance of the control sample (at $\frac{3}{4}$ the intensity for clarity). The control sample was exposed to everything 74

that the (red curve) was (including heat and solvents) except lead nitrate.

FIGURE 41: High contrast, close-up TEM images revealing polycrystalline shell of a single Au/CdSe core/shell NP. The scale bar is 10 nm. The light gray area represents the shell and the dark circle represents the Au core. 76

FIGURE 42: Configuration of layered system in the second approach. In this approach, a monolayer of silver nanoparticles (red spheres on glass slide) is separated from a PbSe QD monolayer (blue spheres) by charged polymer spacer layers (blue and black lines) of varying thicknesses. 77

FIGURE 43: TEM image of silver nanoparticles fabricated with a 3:1 Ag:NaBH₄ ratio. The scale bar is 100 nm. 81

FIGURE 44: Average silver nanoparticle size determined by TEM versus the Ag:NaBH₄ ratio used in the synthesis. As the ratio increases, the average TEM size increased too. For each ratio, there were at least 60 nanoparticles diameters measured (error bars). 82

FIGURE 45: Colloidal Ag NPs normalized absorbance changes versus wavelength, nm with changing Ag:NaBH₄ ratio. The blue arrow represents the absorbance trend as this ratio increases. The red spheres show the relative nanoparticle size as this ratio changes. The decrease in absorbance shoulder as the particles get smaller corresponds to the decrease in higher order plasmon modes. 83

FIGURE 46: Scanning electron microscope image of a Au NP covered glass slides with PAA and PSS polymer layers. The scale bar is 500 nm. 85

FIGURE 47: Evolution of a photoaging Ag NP. a) Represents the decrease in the SPR extinction maximum as the NPs photooxidize in the presence (red) and absence (blue) of oxygen over time. b) Represents the TEM image of the (top) non-oxidized and (bottom) oxidized surface. 174 Reprinted (adapted) with permission from (Grillet, N.; Manchon, D.; Cottancin, E.; Bertorelle, F.; Bonnet, C.; 86

Broyer, M.; Lerme, J.; Pellarin, M., Photo-Oxidation of Individual Silver Nanoparticles: A Real-Time Tracking of Optical and Morphological Changes. *Journal of Physical Chemistry C* 2013, 117 (5), 2274-2282.). Copyright (2013) American Chemical Society.

FIGURE 48: Integrating sphere set-up for direct absorption and scattering measurements, For the absorbance measurements, a white plug was placed behind the sample (orange rectangle). For the scattering, a black light trap was placed behind the sample so that only the scattering off the NPs were measured by the spectrometer fiber (blue port). The grey rhombus on each set up represents the open, entrance port for the incoming light. The white oval represents the baffle which prevents light coming directly off the sample into the detection fiber. 88

FIGURE 49: Scattering (left axis, black curve) and absorbance (right axis, blue curve) versus energy (eV) of Ag monolayer films made of washed NPs. The single scattering peak corresponds to the lower energy mode of the NPs absorbance. This may be due to the coherent plasmon resonance. 89

FIGURE 50: Lowest energy scattering (blue) and absorbance (red) peaks versus Ag:NaBH₄ ratio. A linear fit was performed on each data set highlighting the trend, which is a red shift with increasing ratio and thus the NP size. 91

FIGURE 51: Scattering spectra of film series made with different sizes of Ag NPs. From black to yellow represents an increase in Ag:NaBH₄ ratio and thus the increase in size. There is a red shift in scattering as the NP sizes increase. 92

FIGURE 52: Atomic Force Microscopy (AFM) images of Ag NP films with increasing soak times A) 10 seconds B) 600 seconds and C) 2700 seconds. The AFM area for each film was 500 nm². The particles in each area were counted, and then the particle density was calculated (NP/nm²). 94

FIGURE 53: Particle density (NP/nm²) as determined by AFM versus soaking time (seconds) of films with the same size NPs. As the soaking time increased, the particle density increased. 95

- FIGURE 54: Film absorbance with different NP soaking times: (black) 10 seconds (blue) 600 seconds and (red) 2700 seconds. As the soaking time increases (from black to blue to red) the appearance of a higher order mode appears. This mode may be due to the formation of a coherent plasmon resonance as the interparticle distances decrease. 96
- FIGURE 55: Film scattering with different NP soaking times: (black) 10 seconds (blue) 600 seconds and (red) 2700 seconds. As the soaking time increases (from black to blue to red) the appearance of a higher order mode appears. This mode may be due to the formation of a coherent plasmon resonance as the interparticle distances decrease. 97
- FIGURE 56: Structure of PSS, poly(sodium 4-styrene-sulfonate). The negatively charged sulfate group provides the polymer charge. The sodium ions are removed from the films by rinsing with water. 99
- FIGURE 57: Structure of PAA before A) and after B) protonation by HCl. The pH of the polyallylamine was brought to 5.5 by the addition of HCl. The chlorine ions were washed away from the films by rinsing with water. 99
- FIGURE 58: Example of the step-height measurement with AFM. The bottom left image represents the top-down view of the area that was measured. Here, the dark area is where the film was scratched away and the light, bumpy area is the polymer coated NP film. The red and green lines are the areas where the step differential was measured, revealing the thickness of the film. 101
- FIGURE 59: Average film thickness vs number of applied polymer layers. Measurements with error bars are shown in red and a power-law fit function was used to fit these (weighted) data. The gray shaded region indicates a confidence region \pm one standard deviation. The fit function is provided in the bottom right corner. 102
- FIGURE 60: TEM image of air stable PbSe QDs. The scale bar is 50 nm. From this image, the average PbSe QD size was determined to be 3.306 ± 0.428 nm. 105

- FIGURE 61: Close-up TEM image of air stable PbSe QDs. The scale bar is 10 nm. The green circle highlights a single QD. The lattice fringes are visible. 106
- FIGURE 62: Lifetime decay of PbSe QDs suspended in anhydrous hexanes at 1014 nm emission. The left and right decays are in a small (700 ns) and large (10 μ s) time window, respectively. 107
- FIGURE 63: Average absorbance (black) and scattering (red) versus energy (eV) of 15 different Ag NP films made with the same size Ag NPs before polymer and QD application. The shading represents \pm one standard deviation. 109
- FIGURE 64: Scattering proportion versus energy (eV) of Ag NP films before polymer and QD application. The shading represents \pm one standard deviation. The areas at which the scattering proportion are greater than 0.5 mean that light at those energies is more likely to be scattered than absorbed by the Ag NPs. 110
- FIGURE 65: Average absorbance (black) and scattering (blue) versus energy (eV) of plain polymer films of varying thicknesses. The shading represents \pm one standard deviation. 112
- FIGURE 66: Average absorption (dark) and scattering (light) before (light and dark pink) and after (dark and light blue) two polymer layers added (in triplicate). The shading represents \pm one standard deviation. 113
- FIGURE 67: Average scattering proportion changes upon two polymer layer additions. The black curve represents the scattering proportion before polymers were added and the blue curve represents the scattering proportion after 2 polymer layers were added. The shading represents \pm one standard deviation. The change in scattering proportions can be attributed to the change in the NPs surrounding dielectric environment. 114
- FIGURE 68: Average scattering proportion of films with different # of polymer layers. The black curve represents the scattering proportion of 115

the Ag NP film before polymer addition. The curves from light blue to pink represent an increase in number of polymer layers.

FIGURE 69: Average absorbance (purple) and scattering (black) versus energy (eV) of QD control films (on 0, 2, 4, 6, and 8 polymer layers). The shading represents \pm one standard deviation. 116

FIGURE 70: Mie theorized extinction versus energy (eV) of 20 nm diameter Ag NPs in the presence of air (black) PAA and PSS polymer layers (purple) and PbSe QDs (light blue). 117

FIGURE 71: Theoretical absorption changes of Ag NPs in the presence of PbS QDs. Each trace represents a different Ag NP concentration (C) and thus different QD-NP distances. The C values 1.5-4 represent area densities of 20-5 %, respectively. The insets show the respective calculated gain. 118
© de Arquer, F. P. G.; Beck, F. J.; Konstantatos, G., Absorption Enhancement in Solution Processed Metal-Semiconductor Nanocomposites. [2011] Optical Society of America.

FIGURE 72: Calculated scattering gain versus energy. From black to light blue represents an increase in NP-QD distance. The red curve corresponds to the right axis and represents the average Ag NP scattering. 119

FIGURE 73: Calculated absorbance gain versus energy. From black to light blue represents an increase in NP-QD distance. The red curve corresponds to the right axis and represents the average Ag NP scattering. 120

FIGURE 74: Change in film scattering versus energy (eV) with increasing polymer spacer thickness. The red curve corresponds to the right axis and represents the average Ag NP scattering. The black, dark blue, and light blue curves represent 0, 4, and 8 polymer spacer layers between QD and NP, respectively. 122

FIGURE 75: Change in film absorbance versus energy (eV) with increasing polymer spacer thickness. The black and dark blue curves represent 0 and 8 polymer spacer layers between QD and NP, 123

respectively. The red curve corresponds to the right axis and represents the average PbSe QD absorbance.

FIGURE 76: Change in film absorbance versus energy (eV) with increasing polymer spacer thickness. The black and dark blue curves represent 0 and 8 polymer spacer layers between QD and NP, respectively. The red curve corresponds to the right axis and represents the average Ag NP absorbance. 124

FIGURE 77: Scattering proportion versus energy (eV) of total films as the QD-NP distances get smaller (light blue to black). The red curve corresponds to the right axis and represents the average Ag NP scattering proportion. 125

FIGURE 78: Steady state emission of PbSe QD films in the absence (black) and presence (blue) of Ag NPs. The dashed curves represent the respective PL when excited at energies below the MEG threshold (565 nm), while the solid curves represent the PL when excited at energies above the MEG threshold (410 nm, capable of generating multiple excitons). 127

FIGURE 79: PLE of QD films in the absence (black) and presence (blue) of Ag NPs. The dark blue curve represents an 8-polymer layer QD-NP distance and the light blue curve represents a shorter, 2-polymer layer distance. 129

FIGURE 80: Normalized PLE of QD films in the absence (black) and presence (blue) of Ag NPs. The dark blue curve represents an 8-polymer layer QD-NP distance and the light blue curve represents a shorter, 2-polymer layer distance. The red curve corresponds to the right axis and represents the average Ag NP scattering proportion. 130

FIGURE 81: [PLE of QDs with Ag/PLE of QDs alone] The curves from black to light blue represent an increase in Ag-QD spacing. The PLE ratio data were smoothed with a boxcar width of 5 and the background was subtracted for clarity purpose. The red curve corresponds to the right axis and represents the Ag NP scattering proportion. 131

FIGURE 82: Comparison of PL enhancement versus photon energy (eV) in triplicate) of different Ag-QD distances: 0 (light blue), 2 (medium blue), 4 (dark blue), 6 (purple) and 8 layers (pink). Ratio values above 1 would be indicative of enhancement. These values are all less than 1 because the energy transfer from QDs into the metal have not been accounted for. 132

FIGURE 83: Comparison average PL enhancement averages of different Ag-QD distances: 0 (light blue), 2 (medium blue), 4 (dark blue), 6 (purple) and 8 layers (pink). For clarity, the number of polymer layers are next to the respective curves. Ratio values above 1 would be indicative of enhancement. These values are all less than 1 because the energy transfer from QDs into the metal have not been accounted for. 133

FIGURE 84: Distance-dependent time resolved photoluminescence decays of NP-QD films. The blue curves represent the lifetimes of PbSe QDs on polymer alone, and the red curves represent different polymer spacings between QD and NP. The shortness of lifetime with increasing proximity from QD-NP corresponds to more energy transfer into the metal. 134

FIGURE 85: Fluorescence lifetime of QDs versus distance between NP and QD (red) and QDs alone (blue). The shortness of lifetime with increasing proximity from QD-NP corresponds to more energy transfer into the metal. 135

FIGURE 86: Calculated excitation enhancement vs energy of 0 (light blue), 2 (blue), 4 (dark blue), 6 (purple) and 8 (pink) layers of polymer between QD and NP. If there is no excitation enhancement, the value for excitation enhancement is 1. If the value on the y-axis is greater than one, then there is an absorption enhancement caused by the presence of Ag NPs. 139

FIGURE 87: Calculated average excitation enhancement vs energy of 0 (light blue), 2 (blue), 4 (dark blue), 6 (purple) and 8 (pink) layers of polymer between QD and NP. For clarity, the number of polymer layers is next to each respective curve. If there is no excitation enhancement, the value for excitation enhancement is 1. If the value on the y-axis is greater than one, then there is an absorption enhancement caused by the presence of Ag NPs. 140

FIGURE 88: Excitation enhancement values versus film thickness (nm). The enhancement values were taken at different excitation energies: 2.0 eV (red), 2.5 eV (yellow), 3.0 eV (green), and 3.5 eV (blue). The MEG threshold for the QDs is around 2.75 eV. 141

FIGURE 89: An example of multi pulse time-resolved fluorescence decays (CdSe QDs).¹⁸⁰ Reprinted (adapted) with permission from (Singh, G.; Guericke, M. A.; Song, Q.; Jones, M., A Multipulse Time-Resolved Fluorescence Method for Probing Second-Order Recombination Dynamics in Colloidal Quantum Dots. *Journal of Physical Chemistry C* 2014, 118 (26), 14692-14702.). Copyright (2014) American Chemical Society. 145

LIST OF ABBREVIATIONS

μm	Micrometer
AFM	Atomic Force Microscopy
AIST	National Institute of Advanced Industrial Science and Technology
AM	Air Mass
Cd_2SSe	Cadmium Selenide Sulfide
CdS	Cadmium Sulfide
CdSe	Cadmium Selenide
CdTe	Cadmium Telluride
CIGS	Copper Indium Gallium Diselenide
CO_2	Carbon Dioxide
$\text{Cu}_2\text{ZnSnS}_4$	Copper Zinc Tin Sulfide
CuTe	Copper Telluride
EDX	Energy Dispersive X-ray
E_g	Band Gap
EQE	External Quantum Efficiency
FhG-ISE	Fraunhofer Institute for Solar Energy Systems
GaInP	Gallium Indium Phosphide
II	Impact Ionization
InAs	Indium Arsenide
ITO	Indium Tin Oxide
J-V	Current-Voltage

LG	Lucky Goldstar Electronics
MEF	Metal-enhanced Fluorescence
MEG	Multiple Exciton Generation
MgZnO	Magnesium Zinc Oxide
N ₂	Nitrogen Gas
NIR	Near Infrared
Nm	Nanometer
NP	Nanoparticle
NREL	National Renewable Energy Laboratory
PbS	Lead Sulfide
PbSe	Lead Selenide
PCE	Power Conversion Efficiency
PL	Photoluminescence
PLE	Photoluminescence Excitation
PSC	Perovskite Solar Cell
PV	Photovoltaic
QD	Quantum Dot
QY	Quantum Yield
SEM	Scanning Electron Microscopy
Si	Silicon
SnO ₂	Tin Dioxide
SPR	Surface Plasmon Resonance
TEM	Transmission Electron Microscopy

TOPSe Trioctylphosphine Selenide

ZnO Zinc Oxide

SECTION I INTRODUCTION

The overall aim of the proposed research is to examine the potential of surface plasmon resonances (SPR) to boost the effectiveness of multiple exciton generation (MEG) by increasing absorption rates above the MEG energy threshold in near infrared (NIR) quantum dots (QDs). This exciton-plasmon coupling could be a general strategy for increasing absorption rates in solar cells, enabling thinner and cheaper devices. This investigation proposed is relevant for the development of cheap, low cost, and highly efficient devices at creating electricity from solar energy.

In this chapter, I am going discuss the motivations and background for my research. I will talk about the latest solar energy technologies and highlight their advantages and disadvantages. I will then focus on QD solar cells and describe some of their specific properties and potential for efficiency improvements. One is MEG, which promised to revolutionize ‘third generation’ solar technology but has suffered some setbacks with lower efficiencies than many hoped. This research project takes a slightly different approach. Instead of trying to improve the efficiency of MEG, we are working on ways to maximize the utility of MEG by increasing the amount of light absorption above the MEG threshold. I will discuss the use of surface plasmons in metal nanoparticles as a potentially attractive way to do this.

CHAPTER 1.1 WHY RESEARCH SOLAR ENERGY?

The research and development of novel solar energy technologies is imperative for a variety of reasons including environmental preservation and boosting the economy. In a mere hour, there is more harvestable solar energy hitting the earth's surface than humans consume in a year.⁵ Solar energy can be used for many applications ranging from seawater desalination to photovoltaic cells, where photons are used to generate electricity.⁶

Aside from the exquisite environmental benefits, solar has the potential to greatly improve our economy while subsequently decreasing our dependency on Middle Eastern oil. Doubled from 2010, there are approximately 209 K Americans that work in the solar industry.⁷ This number is expected to nearly double by 2021.⁷ Needless to say, efforts toward the advancement of solar technology will not be in vain. To place our proposed research toward a novel photovoltaic device into context, the current "state-of-the-art" will be discussed.

1.1.1 Current State-of-the-Art

First, the top current solar cells/modules (2019) should be noted.

Table 1 highlights the top power conversion efficiencies (PCE) of some of the top classes of solar cells reported to date.⁸ It includes the test center, date of acquisition, and a brief description of the device.

Table 1: Some of the most recent (2019) reported single-junction solar cell/module efficiencies measured under the global air mass 1.5 spectrum (1000 Wm^{-2}) at 25°C ⁸

Classification	Efficiency (%)	Test Center (date)	Description
Si (crystalline)	26.7 ± 0.5	AIST (3/17)	UNSW p-type PERC top/rear contacts
GaInP	21.4 ± 0.3	NREL (9/16)	LG Electronics, high bandgap
CIGS (thin-film)	22.6 ± 0.5	FhG-ISE (5/16)	ZSW on glass
CdTe (thin-film)	22.1 ± 0.5	Newport (11/15)	First Solar on glass
Perovskite (thin-film)	23.7 ± 0.8	Newport (9/18)	ISCAS, Beijing

Closely following Si in PCE are: GaInP solar cells and thin film solar cells made up of CIGS, CdTe, and perovskites. It should be noted that the PCE of GaInP, CdTe, and Si PV is approaching the theoretical limit with respect to their E_g . Reported in March of 2017, crystalline Si solar cells still have the top PCE to date of $26.7 \pm 0.5\%$.⁸ Next, some of these top varieties of solar cells will be briefly discussed along with their pros and cons.

1.1.1.2 Silicon Solar Cells

The photovoltaic (PV) cell that is currently dominating commercially is comprised of crystalline silicon (Si) wafers often doped with impurities like phosphorus for increased conductivity. Si PV is commercially available at a relatively low cost. Solar

plants and farms are comprised of many Si solar panels, which are made up of Si wafers interconnected to form a circuit.

Pros: The prominence of Si already in the circuit and PV market is a huge plus because there are already established ways of fabrication at a large scale. There is currently enough Si PV installed in the U.S. to decrease the amount of the ozone-damaging greenhouse gas, CO₂, emission by 1.1 million metric tons per year!⁷

Cons: Some of the current issues with Si involve its low absorption coefficient, indirect E_g, high cost. Though prices of Si PV have dropped 62 % since 2011, in order for solar energy to actually compete with fossil fuels like coal, the costs need to drop about three fold.⁷ Much of the decrease in price was achieved by reducing “soft costs” such as labor and overhead costs. The raw cost and intricate processing of the thick (\approx 180-300 μ m) crystalline Si wafers will be much harder prices to slash.⁹

Current Research: Per Web of Science, there are 105 publications with the topic “silicon solar” so far in 2017.

Much of this research (2017) involves the utilization of nanostructures to enhance Si PV light trapping and absorption such as: Si QD layers on the pyramidal texture,¹⁰ the direct etching of nanostructures^{11,12}, anodic aluminum oxide (AAO) nano-gratings for enhanced infrared response¹³, nano-texturing with SiO₂/Si₃N₄¹⁴, Si nanowire homojunction solar cells¹⁵⁻¹⁷, resonant waveguide gratings of SiO₂ and TiO₂¹⁸, and Si nano-cone arrays.¹⁹ Other research is geared toward enhancing the thermal and electrical properties of Si PV by adding features to the surface like: single walled carbon nanotubes²⁰ or ultra-thin SiO₂ layers.^{21,22} Unfortunately, we cannot hope to exceed the

Shockley-Queisser limit of PCE in Si PV. Next, a hot, third generation solar cell material, perovskites will be discussed.

1.1.1.3 Perovskite Solar Cells

Perovskite solar cells (PSCs) are made up of organic-inorganic hybrid materials most commonly $\text{CH}_3\text{NH}_3\text{PbX}_3$, ($\text{X} = \text{I}, \text{Br}, \text{Cl}$) and have a perovskite crystal structure. Much like Si PV, PSCs have the ability to generate free charges rapidly after absorbing photons, without a need for an exciton dissociation interface (Figure 2).²³

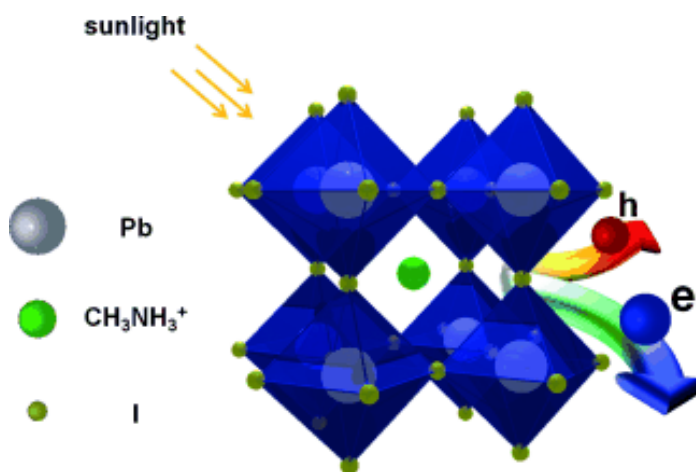


*Figure 2: Schematic of the highly efficient Perovskite solar cell. The grey, light green, and dark green spheres represent lead atoms, methylammonium ions, and iodine atoms, respectively. The arrows represent the one-step charge carrier generation.²³ From [Collavini, S.; Volker, S. F.; Delgado, J. L., *eUnderstanding the Outstanding Power Conversion Efficiency of Perovskite-Based Solar Cells. Angewandte Chemie-International Edition* 2015, 54 (34), 9757-9759.]*

Reprinted with permission from John Wiley and Sons.

Pros: Due to their high conductivity, power conversion efficiency, and low cost perovskite-based solar cells are the fastest developing solar technologies thus far.²³ They are solution processable, which means they can be cheaply prepared on a large scale. The material can be processed onto a metal-oxide surface in one step by mixing PbX_2 and $\text{CH}_3\text{NH}_3\text{X}$ in air.²⁴ The efficient charge extraction of PSCs can be attributed to the

notoriously long diffusion lengths. Triiodide and mixed halide perovskites have reported diffusion lengths of 100 nm and of over a micron (an order of magnitude greater than the absorption depth), respectively!²⁵

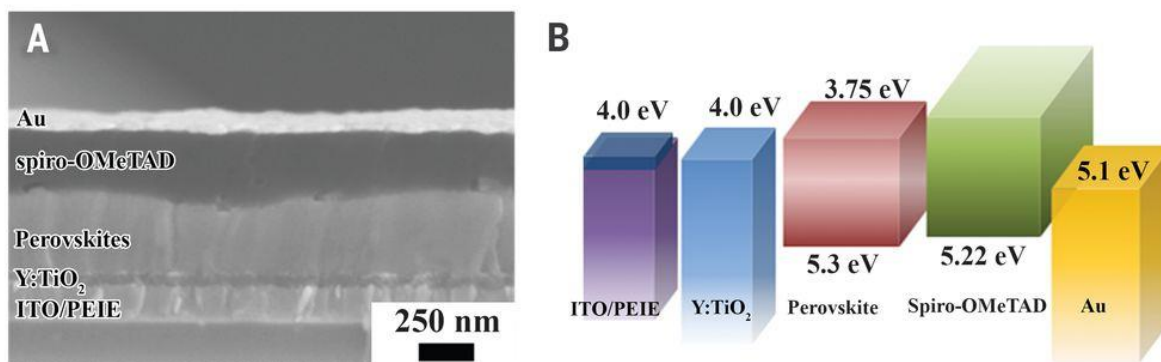


Figure 3: Perovskite device with a >19 % power conversion efficiency. A) labeled SEM cross-section of perovskite solar device B) Energy level diagram (relative to vacuum) of each layer of device²⁶ From [Zhou, H. P.; Chen, Q.; Li, G.; Luo, S.; Song, T. B.; Duan, H. S.; Hong, Z. R.; You, J. B.; Liu, Y. S.; Yang, Y., *Interface engineering of highly efficient perovskite solar cells. Science* 2014, 345 (6196), 542-546.] Reprinted with permission from AAAS.

The 19 % PCE perovskite device (Figure 3) consists of an electron transport layer such as yttrium-doped TiO₂ and cobalt and lithium co-doped Spiro-OMeTAD as the hole transport layer sandwiching the perovskite material.²⁶ The ITO layer was treated with a PEIE polymer to lower the work function and improve electron transport.²⁶

Cons: A common, important concern in the PSC realm is the device thermal and moisture stability. A current-voltage plot in the forward and reverse bias direction of the 19 % efficient PSC (imaged in Figure 3) is shown in Figure 4.

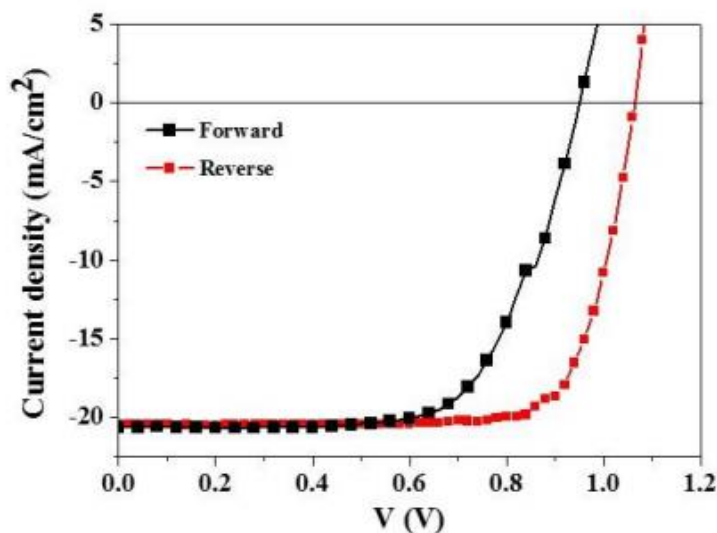


Figure 4: Hysteresis in current density versus voltage curve of planar heterojunction perovskite solar cell (shown in Figure 2) under AM 1.5, 100 mWcm^{-2} . The black and red curves represent the forward and reverse directions, respectively.²⁶ From [Zhou, H. P.; Chen, Q.; Li, G.; Luo, S.; Song, T. B.; Duan, H. S.; Hong, Z. R.; You, J. B.; Liu, Y. S.; Yang, Y., *Interface engineering of highly efficient perovskite solar cells. Science* 2014, 345 (6196), 542-546.] Reprinted with permission from AAAS.

The drastic changes in the J-V curve between the forward (black) and reverse (red) direction indicates the device's poor stability. The PSC sensitivity to the surroundings can cause conformational changes. A study of PCE performance retention over 6 days was performed for devices in ambient air, dry air, and N_2 atmosphere (Figure 5).

Due to moisture, the cells stored in ambient air severely degraded/dissolved after only 24 hours. The cells stored in dry air and N_2 only retained 5% of the original performance after 6 days.²⁶ Thermal stability is also an issue as $\text{CH}_3\text{NH}_3\text{PbI}_3$ experiences a tetragonal to cubic phase transition at 55°C , which can easily occur under direct sunlight.²⁷ Clearly, better stability needs to be achieved in PSCs to be used for practical purposes.

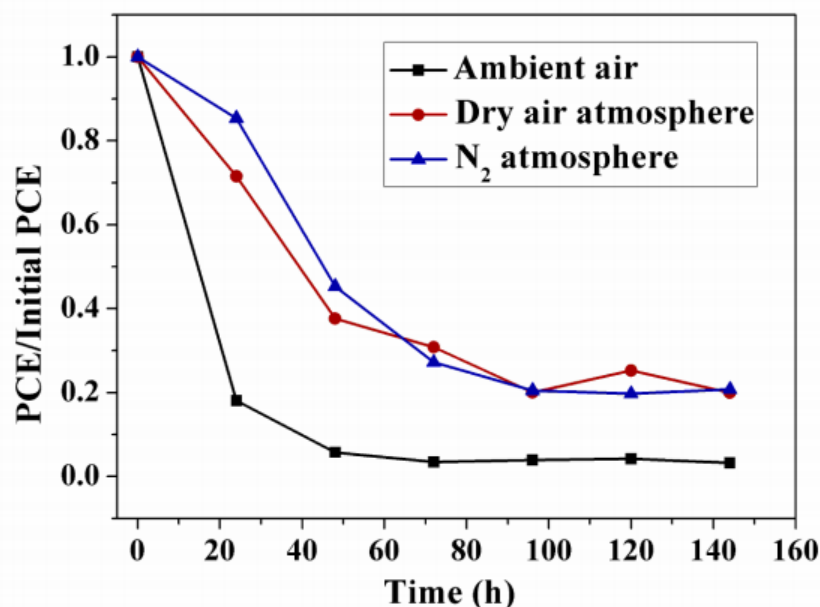


Figure 5: Perovskite stability study of non-encapsulated perovskite solar cells in ambient air, dry air, and N₂ atmosphere (10 devices were studied per condition) over 6 days. The black, red, and blue curves represent devices in ambient air, dry air, and nitrogen gas, respectively.²⁶ From [Zhou, H. P.; Chen, Q.; Li, G.; Luo, S.; Song, T. B.; Duan, H. S.; Hong, Z. R.; You, J. B.; Liu, Y. S.; Yang, Y., *Interface engineering of highly efficient perovskite solar cells*. *Science* 2014, 345 (6196), 542-546.] Reprinted with permission from AAAS.

Current Research: Per web of science, there are 81 publications with the topic “perovskites” so far in 2017. Of this work, there is research to improve PSC thermal stability such as: perovskite nanorods²⁷, novel sequential deposition processing²⁸, and passivation of with SnO₂/ZnO nanorods.²⁹ Some recent efforts to decrease PSC moisture sensitivity include: high-pressure annealing for film recrystallization³⁰, and cobalt doped tin based PSCs.³¹ Most of the recently published literature in PCSs had aims of higher power conversion efficiency. Efforts include: interfacial trap state passivation with ionic-liquid, MATS³², improving the hole extraction layers³³⁻³⁶, improving the electron transport layer³⁷⁻⁴¹, and even developing tandem PSCs.⁴²

Though the research efforts to improve the stability and efficiency of PSCs look promising to improve, the beautiful simplicity and solution processibility of PSCs will

inevitably be lost. Next, some polycrystalline thin film solar cells will be briefly introduced.

1.1.1.4 Polycrystalline Thin Film Solar Cells

Polycrystalline thin film solar cells are made up of materials with high absorption cross sections and are only 1-2 μm thick.

Pros: Thin film solar cells can be fabricated cheaply via roll-to-roll processing on inexpensive substrates like flexible plastic. Thin solar cells use much less material, and have lower recombination losses.⁴³ The absorbing layer can be made up of anything from organic porphyrins to inorganic copper indium gallium diselenide (CIGS).

Cadmium Telluride (CdTe) Solar Cells: CdTe thin films have been of interest for the past 30 years due to their nearly perfect E_g , high absorption, and theoretical maximum PCE of 27 %.⁴⁴ Technically, a CdTe film of only 2 μm is necessary to absorb 100 % of incident solar irradiation.⁴⁵ Films of 10 μm have reached over 16 % in the laboratory.⁴⁶ A research group from the Tokyo Institute of Technology have claimed to have fabricated an 11.2 % efficient CdTe thin film of only 1 micron thick!⁴⁷ To quickly and efficiently fabricate thin film cells, a common technique for CdTe deposition is by close-space sublimation (CSS).⁴³ Many groups have added an n-conducting layer of CdS to create a depletion region with CdTe.⁴⁸⁻⁵¹

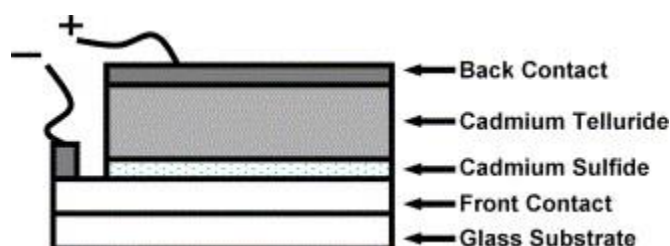


Figure 6: Schematic of a layered, CdS/CdTe thin film solar cell.⁴⁵ Reprinted from *Solar Energy* 2004, 77 (6), Ferekides, C. S.; Balasubramanian, U.; Mamazza, R.; Viswanathan, V.; Zhao, H.; Morel, D. L., *CdTe thin film solar cells: device and technology issues*. 823-830. Copyright (2004), with permissions from Elsevier.

The thin CdS layer also acts as a window to allow green light to the CdTe.⁴⁵

Typically, as shown in Figure 6, the front contact is sputtered SnO₂, and the back contact is CuTe.⁴⁵ CdS/CdTe thin film solar cells PCEs are approaching their theoretical limit of 29 %, reaching efficiencies as high as 21 % in the laboratory.⁵²

Copper indium gallium diselenide (CIGS) solar cells: CIGS are another commonly used material for thin film PV due to their optimal E_g and high absorption.⁵³ Films made by three step electrodeposition had PCEs of 10.9 % as compared to the expensive vapor deposition method.⁵⁴ Employing a tandem thin film has great potential for thin cells with high PCE.⁵⁵ Elbae et. al. found that CGS-CIG tandem cells have simulated efficiencies of 26.21 % when each layer is 0.19 μm .⁵⁵

Cons: A feat to overcome with thin film technology is trapping as much light as crystalline Si by appearing “optically thick,” while being orders of magnitude thinner. An issue that has risen in thin CdTe PV is the presence of pinholes at a minimum thickness of approximately 2 μm .⁴³ These deep defects act as trap states and strongly affect the cells performance.⁵⁶ Without an extra cleaning step, oxide formation on CdTe which decreases performance.⁴⁵ CIGS solar cells suffer from complicated fabrication and relatively low PCE.

Current Research in thin films: Per web of science, there are 231 publications with the topic “thin film solar” so far in 2017. Of this research, groups have worked on thin film stability and degradation in tropical climates⁵⁷ Some groups are working on enhancing thin cell performance CIGS.⁵⁸ Most of the recent publications in thin films focuses on new materials such as: CdS doped-phosphate glass⁵⁹, MgZnO⁶⁰, and Cu₂ZnSnS₄.^{58, 61, 62} Some of the top current solar PV devices have now been discussed. One may now ponder where solar research is heading.

1.1.1.5 Why are we interested in QDs for solar cells?

Nano-based solar devices are a promising alternative to Si-based PV due their attractive qualities for harvesting solar energy such as their size tunable optical properties, high absorption cross sections, and catalytic behavior.¹ Furthermore, QDs make excellent sensitizers due to their small size, low cost, solution processability, and high efficiency.⁶³

Pros: QDs have been often incorporated to existing solar cell technologies to enhance performance. When added to polymer solar cells (PSCs), Cd₂SSe/ZnS QDs increased the device’s power conversion efficiency increased by over 1 %.⁶⁴ Compared to the control, adding these QDs to PSCs led to better light trapping, exciton dissociation, and overall charge transport.⁶⁴ For a realistic approach, the issues that come with nanomaterials should be noted.

Cons with nanomaterials: Nanomaterials are dominating in research areas including solar, wind, biomass, hydrogen, and tidal energy.⁶ Along with the unique properties of nanomaterials, come unique challenges. The high surface area to volume

ratio of nanoparticles (NPs) has a drawback: the localization of charges in surface defects (trap states). Energetically, these states reside within the NP band gap and lead to non-radiative decay of the exciton due to a decrease in the wave function overlap.⁶⁵ Efficient passivation of trap states with ligands or inorganic shells can help relieve this issue. To gain an idea of the trajectory of certain solar research topics, a literature search of the past 10 years was conducted and plotted.

1.1.2 Research in the Past 10 Years

To highlight the current trends in solar research, the number of articles published in various topics in solar over the past 10 years are plotted in Figure 7. From 2006 to approximately 2014, research in silicon, polymer, and quantum dot solar cells steadily increased, and then dropped or remained the same from 2014 to 2016. The recent drop in these fields may be due to groups shifting to research trending perovskite solar cells- as most chemistry labs already have the materials to make perovskites lying around and the means to do so.

The more complicated solar systems like CIGS and plasmonic solar cells have very slowly increased in popularity in the literature from 2009 until now. This may be attributed to the complexity of the device fabrication.

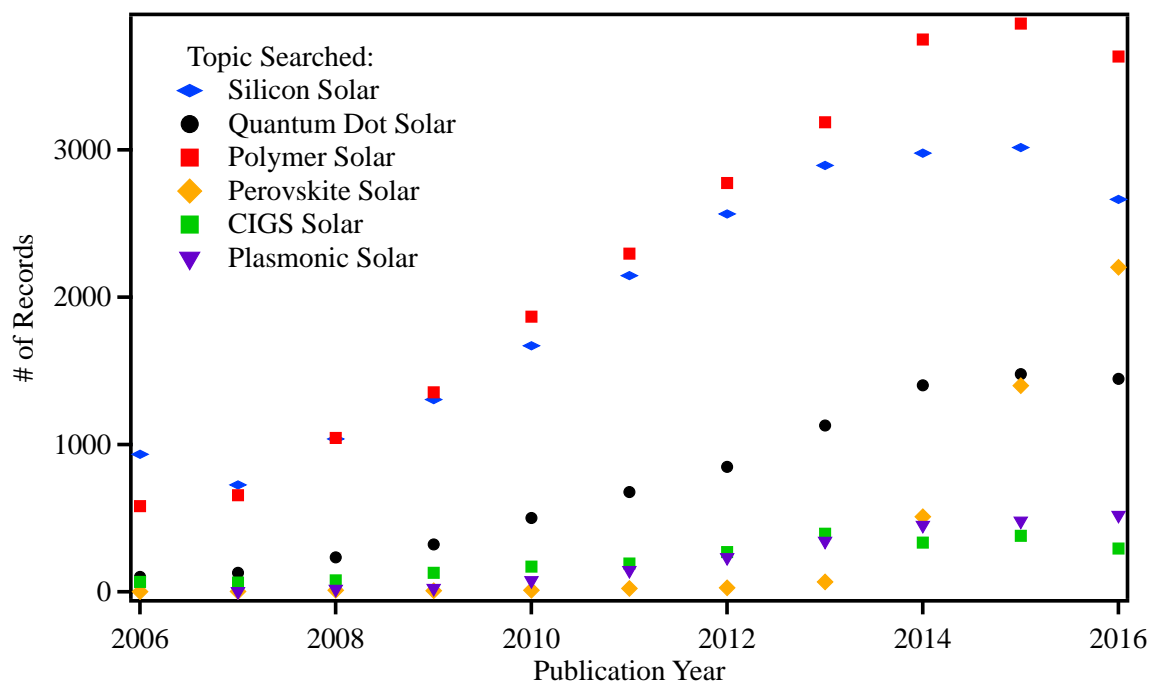


Figure 7: Trends in solar: number of records versus publication year of various topics in solar (per Web of Science). The blue, black, red, yellow, green, and purple curves represent the number of publication records in silicon, quantum dot, polymer, perovskite, CIGS, and plasmonic solar versus year, respectively.

Hopefully now, the context for our research area has been framed. Topics involving the proposed research will now be discussed, beginning with how to absorb more solar energy. Since many nanomaterials have size-tunable optical properties, how can we utilize them best to absorb more of the solar spectrum?

CHAPTER 1.2 HOW CAN WE UTILIZE MORE OF THE SOLAR SPECTRUM?

As aforementioned, current Si PV technology cannot utilize near IR photons. Research in slimming down Si PV geared toward fabricating cheaper devices has its consequences. There have been efforts to slim down Si PV while maintaining the absorption. Current Si PV can only absorb sunlight with wavelengths up to 1100 nm. Figure 8 illustrates that simply slimming down crystalline Si solar cells (to 2 μm) is not the most efficient solution to the raw cost problem of current solar cell technology. The Si wafer is thinner both physically and optically as most of the sunlight from about 600 – 1200 nm (blue curve) is not able to be absorbed (red curve).

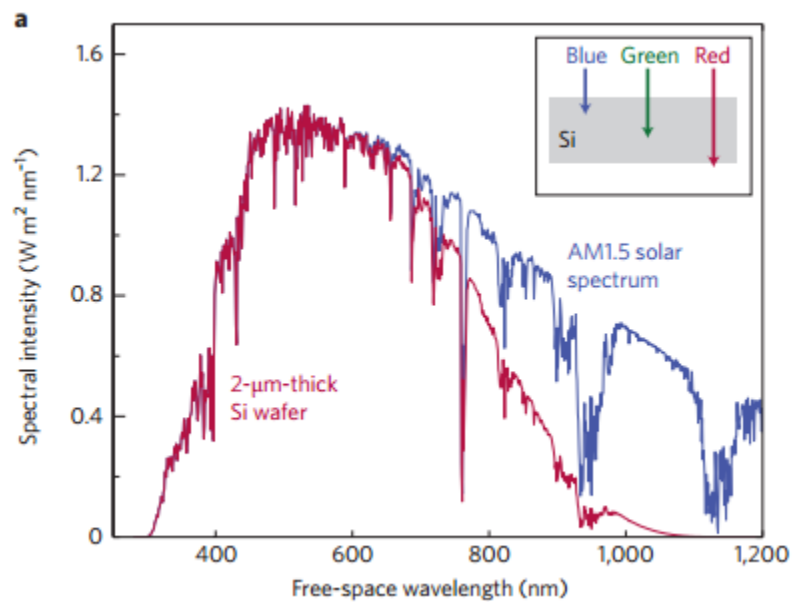


Figure 8: Solar energy absorbed (red) by a 2 μm thick Si wafer (assuming no reflection) versus solar spectrum at air mass 1.5 (blue). The inset reveals the relative depth that certain colors of light make it through a Si device.⁹ Reprinted by permission from [Atwater, H. A.; Polman, A., *Plasmonics for improved photovoltaic devices*. *Nature Materials* 2010, 9 (3), 205-213.] [COPYRIGHT] (2010).

Near infrared QDs can utilize long wavelength light to generate Coulombic-attracted electron-hole pairs, or excitons.

1.2.1 Near-Infrared Quantum Dots (Near IR QDs)

Near IR absorbing/emitting QDs are especially hot in the QD realm due to their great potential in a wide range of applications. Infrared QD photodetector devices, which use InAs QDs, are replacing traditional quantum well photodetectors because they have; intraband absorption due to their normal incident response, lower dark currents, and longer excited state lifetimes which increases the devices responsivity.⁶⁶ These QDs are of interest in biological research because they absorb and emit wavelengths of light that allows light to travel deeply into tissue and their large surface provides a template for targeting molecules. Novel nanoprobe, which are near IR QDs loaded into micelles, have shown the ability to target, treat, and brightly image cancer cells, even in the early stage.⁶⁷ A very commonly implemented near IR QD for light-related research is PbSe.

1.2.2 Lead Selenide Quantum Dots (PbSe QDs)

PbSe QDs are of great interest in the improvement of solar cell efficiency because they have size tunable optical properties in the near IR and are able to generate multiple excited states per one absorbed high-energy photon at relatively high yields.⁶⁸ PbSe is a IV-VI semiconductor with a rock-salt crystal structure and a direct, bulk E_g of 0.27 eV (4592 nm) at RT at four equivalent L-points in the first Brillouin zone.⁶⁹ PbSe exhibits quantum confinement effects at a very large size as it has a large exciton bohr radius of 46 nm which is nearly 8X the size of CdSe (6 nm)!⁷⁰ The electron and hole radii are both

23 nm.⁷¹ A normalized absorbance (solid black line), emission (dashed line), and lifetime measurement (inset) of a PbSe QD sample is shown in Figure 9.

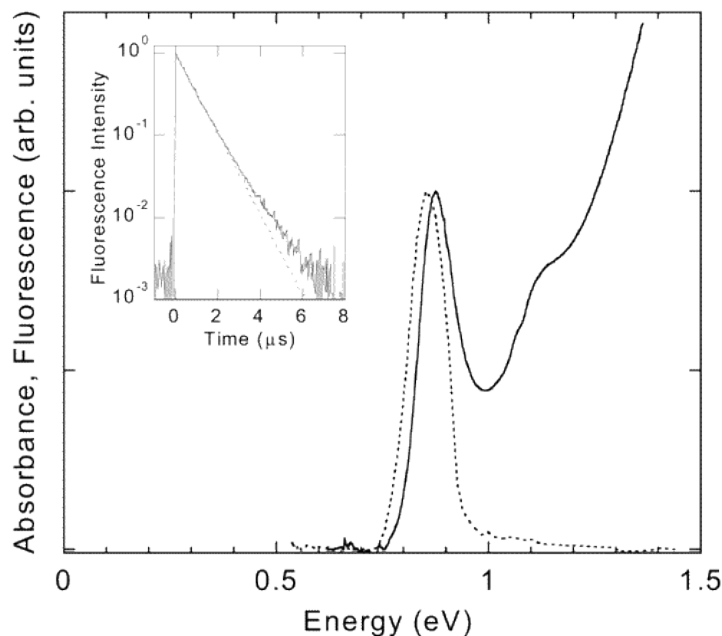


Figure 9: Absorbance (solid), steady state emission (dashed), and time resolved lifetime decay (inset) of PbSe QDs ($E_g = 0.88 \mu s$)⁷² Reprinted (adapted) with permission from (Wehrenberg, B. L.; Wang, C. J.; Guyot-Sionnest, P., *Interband and intraband optical studies of PbSe colloidal quantum dots. Journal of Physical Chemistry B* 2002, 106 (41), 10634-10640.). Copyright (2002) American Chemical Society.

There is a small Stokes shift of these narrow bandgaps, E_g (0.85 eV). PbSe lifetimes have a characteristic single exponential decay. We also propose to work with PbS QDs in a similar way to PbSe.

1.2.3 Lead Sulfide Quantum Dots (PbS QDs)

Lead sulfide is a IV-VI semiconductor with a rock-salt crystal structure and a direct, bulk E_g of 0.41 eV at four equivalent L-points in the first Brillouin zone.⁶⁹ PbS has a large exciton Bohr radius of 18 nm.³ The absorbance spectra of a series of PbS aliquots taken at various synthesis times is shown in Figure 10. This image illustrates PbS a tunable absorption band edge peak followed by a broad strong absorption at slower

energies. The absorbance spectra included of this PbS series demonstrates the strong absorbance across the solar spectrum along with their size-tunability.

Tight binding calculations and experimental data were used to develop the bandgap versus PbS QD size plot shown in Figure 11. The Moreels group used the fit (blue line) in Figure 11 to generate an equation to easily determine the PbS particle diameter from the E_g .³

$$E_0 = 0.41 + \frac{1}{0.0252d^2 + 0.283d}$$

In this equation, E_0 is the bandgap and d represents the particle diameter.

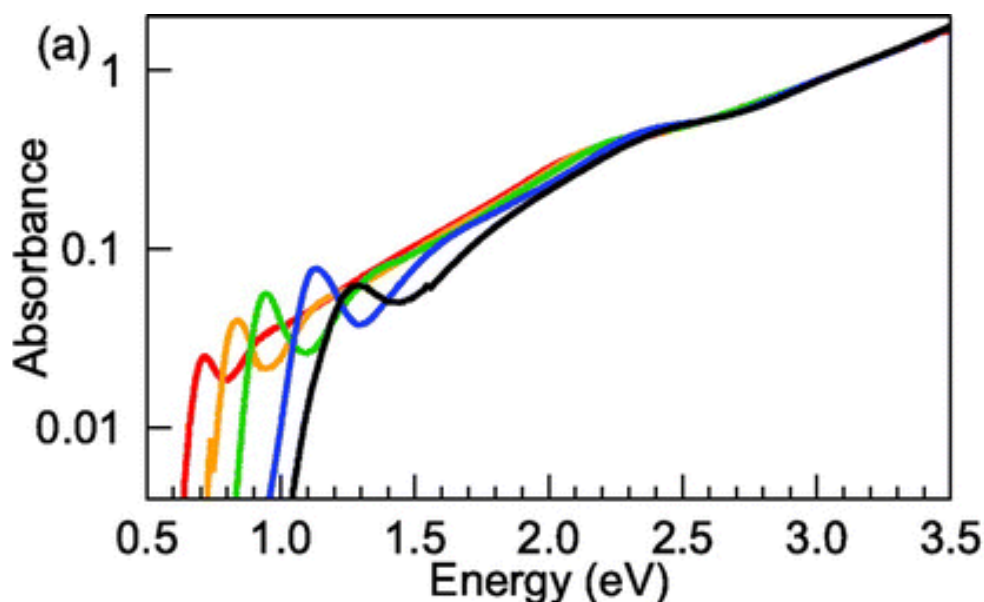


Figure 10: Normalized absorbance spectra of a PbS QD series with E_g ranging from 970-1740 nm (red-black curves). There is an absorbance peak red shift with increasing QD size due to the quantum confinement effects.³ Reprinted (adapted) with permission from (Moreels, I.; Lambert, K.; Smeets, D.; De Muynck, D.; Nollet, T.; Martins, J. C.; Vanhaecke, F.; Vantomme, A.; Delerue, C.; Allan, G.; Hens, Z., *Size-Dependent Optical Properties of Colloidal PbS Quantum Dots*. *Acs Nano* 2009, 3 (10), 3023-3030.) Copyright (2009) American Chemical Society.

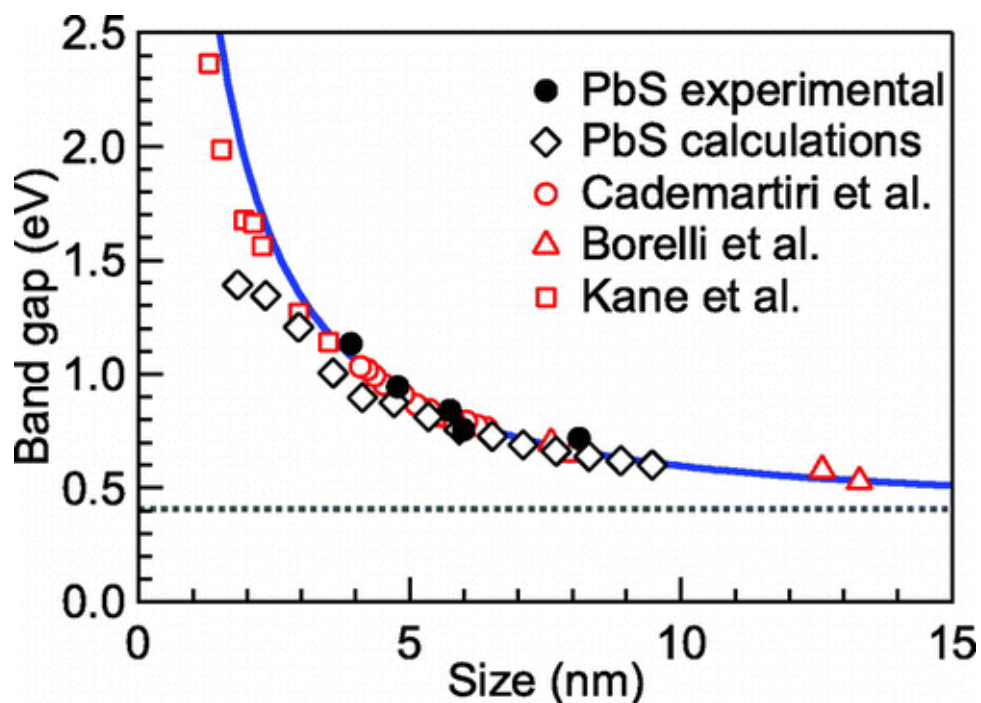


Figure 11: Published (red and solid black), and tight binding calculations (open black diamond) of PbS E_g versus particle size relationship. The dotted line is the bulk E_g (0.41 eV)³ Reprinted (adapted) with permission from (Moreels, I.; Lambert, K.; Smeets, D.; De Muynck, D.; Nollet, T.; Martins, J. C.; Vanhaecke, F.; Vantomme, A.; Delerue, C.; Allan, G.; Hens, Z., *Size-Dependent Optical Properties of Colloidal PbS Quantum Dots*. *ACS Nano* 2009, 3 (10), 3023-3030.) Copyright (2009) American Chemical Society.

We can utilize this relationship to predict the PbS QD diameter from the first absorption peak energy without the necessity of expensive, time consuming TEM for every sample. Since we plan on using both PbSe and PbS QDs, it is important to point out the differences between the two materials.

1.2.4 PbSe QDs versus PbS QDs

PbSe and PbS QDs have similar physical (rock salt crystal structure) and optical qualities. Both types of QDs have the abilities to perform MEG, absorb NIR light, and are optically size tunable. There are slight differences in oscillator strength due to the elemental differences (Figure 12).

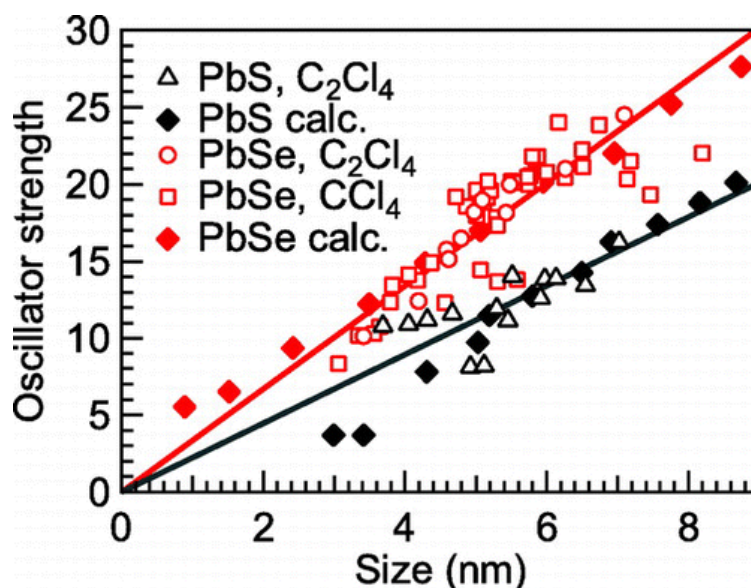


Figure 12: Calculated (solid markers) and experimental (open markers) relationship between oscillator strength and particle size of PbS (black) versus PbSe (red). Overall, lead selenide QDs have a greater oscillator strength than lead sulfide.³ Reprinted (adapted) with permission from (Moreels, I.; Lambert, K.; Smeets, D.; De Muynck, D.; Nollet, T.; Martins, J. C.; Vanhaecke, F.; Vantomme, A.; Delerue, C.; Allan, G.; Hens, Z., *Size-Dependent Optical Properties of Colloidal PbS Quantum Dots*. *ACS Nano* 2009, 3 (10), 3023-3030.) Copyright (2009) American Chemical Society.

In both cases, there is a linear relationship between oscillator strength versus size, which agree well with the tight binding calculations.³ On average, PbSe exhibits stronger oscillator strength than PbS QDs.

The long-term stability and quantum yield of these lead-based QDs can be greatly enhanced if the outer layer is well passivated. Surface passivation with ligand exchange is a less fruitful method due to the high mobility of ligands. A great way of passivating the many charge trapping states on QD surfaces is with an inorganic shell

CHAPTER 1.3 CORE/SHELL QDS

It is highly common to passivate QD surface trap states, and improve stability with an inorganic shell, yielding a core/shell structure.⁷³⁻⁷⁷ Non-epitaxial shelling via cation exchange yields core/shell QDs with even lower interfacial defects, higher quantum yields, and better synthetic control of the core bandgap than epitaxial growth.⁷⁸⁻
⁸⁰ An illustration paired with corresponding e^-h^+ wavefunction distributions of a core only, core/shell, and core/alloy-shell system are included in Figure 13.

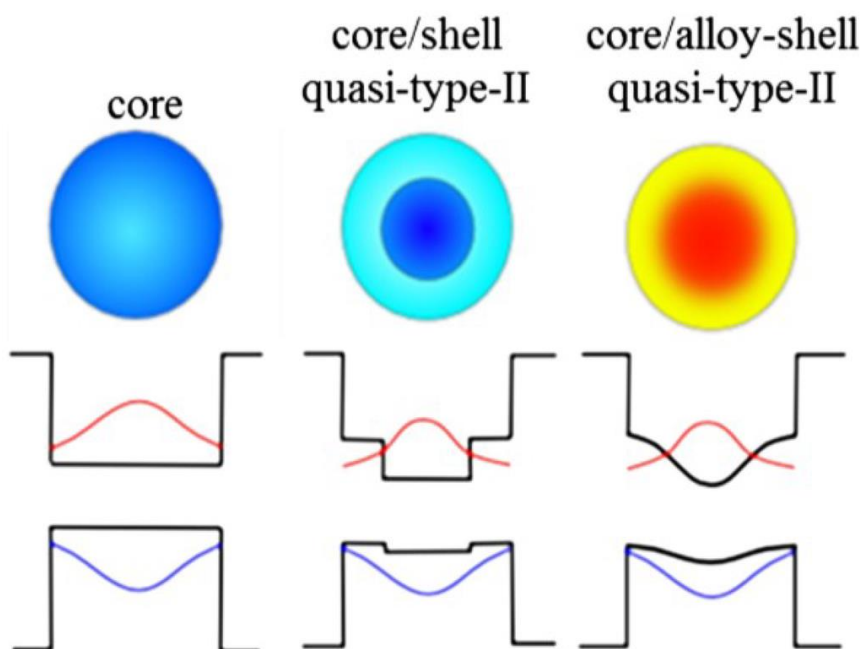


*Figure 13: Types of core/shell heterostructures with the corresponding electron and hole wavefunction distributions below. The quasi-type-II core/shell structures have wavefunctions more promising for charge separation.⁸⁰ Reprinted (adapted) with permission from (Zaiats, G.; Yanover, D.; Vaxenburg, R.; Tilchin, J.; Sashchiuk, A.; Lifshitz, E., *PbSe-Based Colloidal Core/Shell Heterostructures for Optoelectronic Applications. Materials* 2014, 7 (11), 7243-7275.) Copyright (2014) MDPI.*

In the core-only situation, the electron and hole wavefunction are delocalized across the entire structure with a highest probability of residing at the center. The

similarities in wavefunctions of the electron and holes may be indicative of higher instances of recombination rather than charge extraction.

In quasi-type-II core/shell and core-alloy shell structures (depending on band-edge offset) one carrier is confined to the core with the other delocalized across the entire NP. This causes partial charge separation, which can be ideal for optoelectronic purposes. The alloy-shell allows for slightly better confinement of the carrier in the core, higher spectral stability, and lower interfacial defects.

In contrast to the core/shell case in Figure 13, the hole is confined to the core and the electron is delocalized across PbSe/CdSe QDs, possibly allowing better charge extraction in a device.⁸⁰ This is the type of confinement that we are interested in for PV device purposes.

1.3.1 PbSe/CdSe Core/Shell QDs

PbSe/CdSe core/shell QDs are not new, as they have been studied thoroughly for the past 10 years.⁸¹ The hole confinement, and electron delocalization in PbSe/CdSe QDs with respect to radial coordinate is shown in Figure 14.⁸⁰

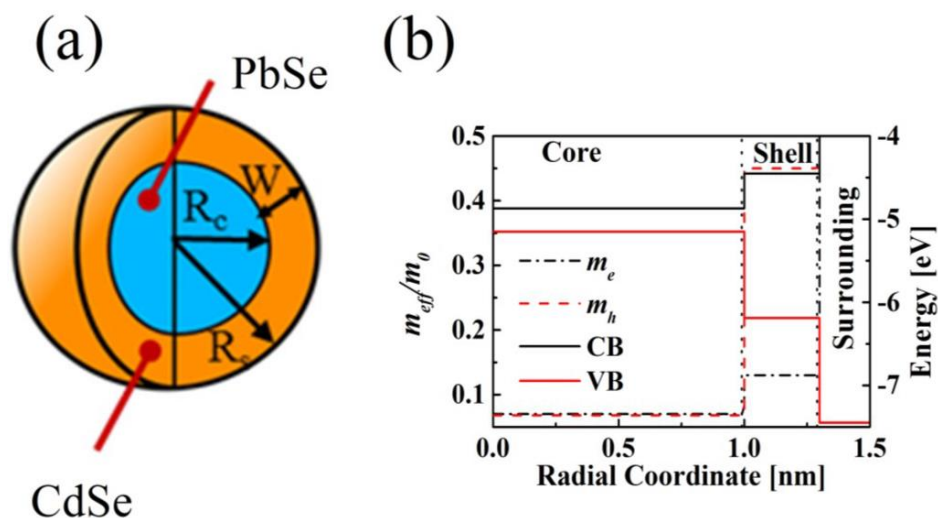


Figure 14: Effective electron (black) and hole (red) masses and energy bands versus radial coordinate in PbSe/Cdse core/shell QDs generated by using the FEA software (COMSOL). The valence and conduction band energies change from the core to the shell.⁸⁰ Reprinted (adapted) with permission from (Zaiats, G.; Yanover, D.; Vaxenburg, R.; Tilchin, J.; Sashchiuk, A.; Lifshitz, E., *PbSe-Based Colloidal Core/Shell Heterostructures for Optoelectronic Applications. Materials* 2014, 7 (11), 7243-7275.) Copyright (2014) MDPI.

In this figure, the hole's effective mass changes much more drastically than the electron's as the coordinate gets into the CdSe shell. The probability of a hole residing in the CdSe shell being zero would indicate an optimal shell thickness for charge extraction. The reduced carrier overlapping in thick-shelled, quasi-type-II QDs like PbSe/CdSe allows for improved multiple exciton generation (MEG).⁸² Pandey and Guyot-Sionnest showed control of electron cooling rates from 6 ps to 1 ns with changing the shell thickness of CdSe/ZnSe QDs.⁸³ This control can be utilized to suppress Auger recombination and further improve MEG-which can greatly enhance PCE in these QDs. We should keep in mind the fact that charge extraction in thicker-shelled QDs is much harder compared to their thin counterparts. If we cannot efficiently extract charges from our device, then the power conversion efficiency will suffer.

1.3.1.1 Fabricating PbSe/CdSe QDs

Step 1: Synthesize PbSe QDs

The PbSe nanoparticles shown in the data below were synthesized via hot injection of TOPSe into a lead oleate solution according to Murray et.al.⁸⁴ The size of the QDs increased as the colloidal suspension was allowed to ripen and grow after the hot injection. TEM of PbSe QDs taken 954 seconds after injection are shown in Figure 15.

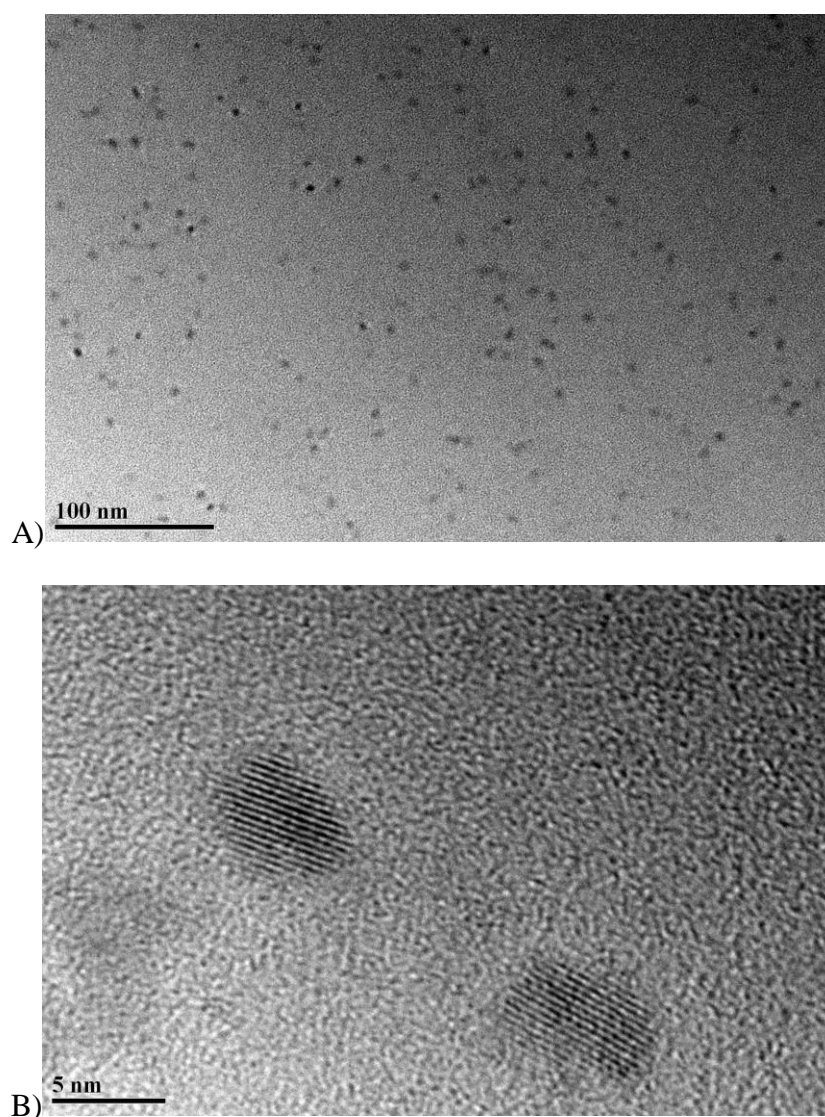


Figure 15: Zoomed out (A) and in (B) TEM image of PbSe QDs taken 954 seconds after hot injection. The scale bar in A) and B) are 100 and 5 nm, respectively. Here, the average QD

diameter is approximately 5 nm. A) reveals the monodisperse size distribution. In image B), the lattice fringes and crystallinity of the two quantum dots are clear.

Figure 15-B reveals that the PbSe QDs were formed and ≈ 5 nm in diameter. Part A is a more zoomed out image that shows the particles were highly monodispersed. The absorbance of these PbSe QDs and a standard near IR dye is shown in Figure 16. These QDs are able to absorb most of the solar spectrum.

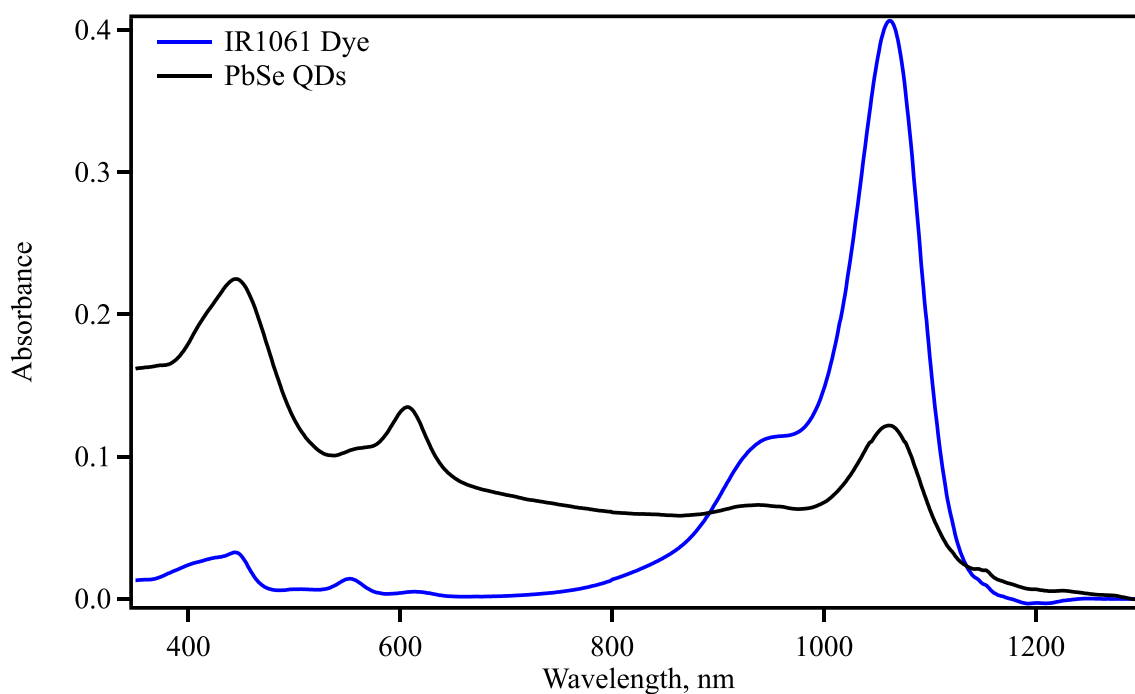


Figure 16: Absorbance versus wavelength, nm of PbSe QDs (black) and near IR dye (IR1061) standard (blue). The absorbance peaks of the two samples are very similar in wavelength. The IR1061 dye was used to determine the relative quantum yield of the QDs.

The relative (to IR1061 dye) QY were calculated of the samples at different reaction times. Figure 17 shows the calculated relative QY versus PbSe reaction time.

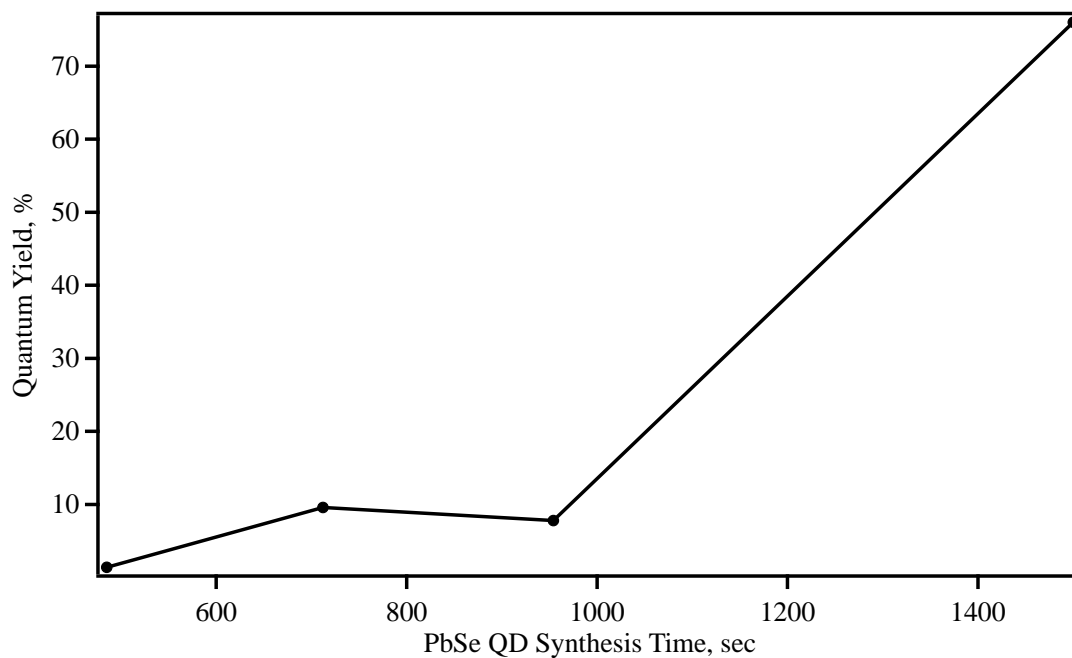


Figure 17: Calculated quantum yield of PbSe QDs taken out at various times after the hot injection. The x-axis represents the PbSe QD synthesis time in seconds. In every case, the reaction was quenched by a rapid injection of a cold solvent mixture.

The longer the QDs were synthesized, the higher the relative QY was. The next step was to improve the PbSe QD stability and QY by adding a CdSe shell.

Step 2: Cation exchange reaction on QDs to yield PbSe/CdSe QDs

A cation exchange reaction was initiated by exposing the PbSe QDs to a cadmium oleate solution at 100 °C. The normalized absorbance spectra as the reaction proceeded are shown in Figure 18.

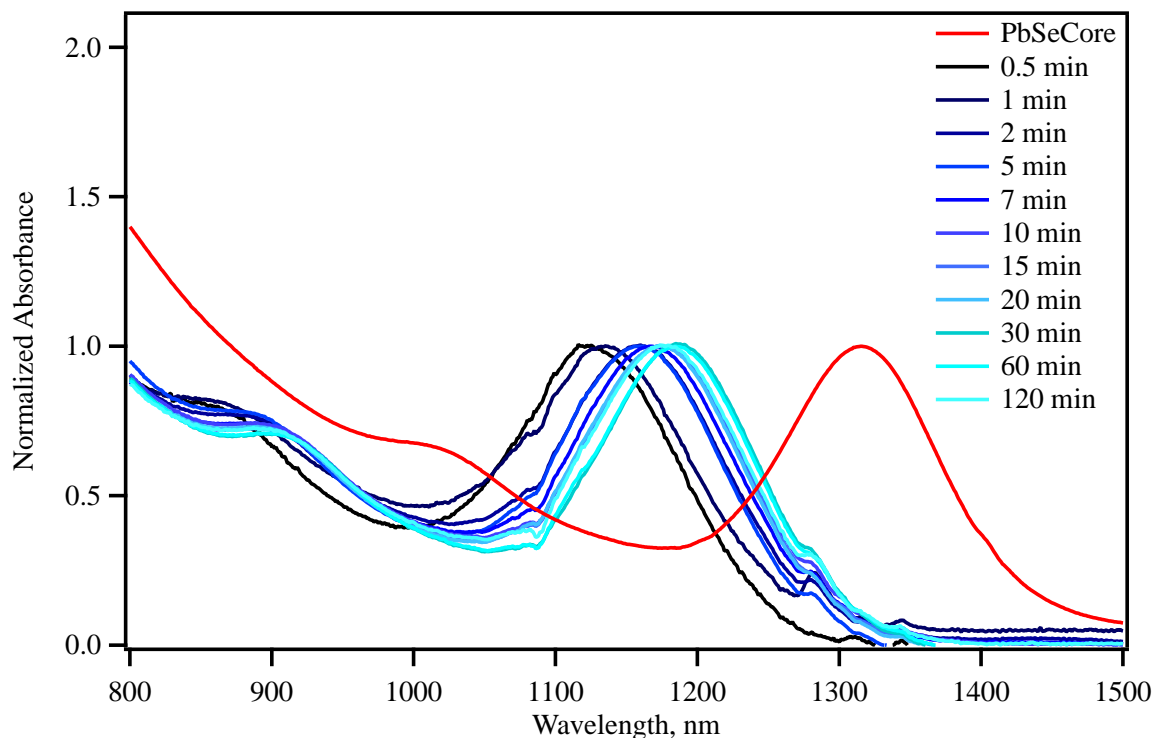


Figure 18: Normalized absorbance of PbSe/CdSe QDs taken during the cation exchange reaction between lead and cadmium. The PbSe core only sample is shown in red. The times correspond to exposure time to the cadmium oleate solution. The increase in the reaction time (black to light blue) means an increase in the lead and cadmium cation exchange and thus the increase in the CdSe shell growth.

After merely 30 seconds (black) of the cation exchange there is a large, ≈ 250 nm blue shift from the core only peak (red), which is attributed to the stronger confinement. The cation exchange starts at the surface of the PbSe QD and works its way inward. So, over time, the effective PbSe core radius shrinks as the reaction proceeds.

Furthermore, (black to light blue) there is a gradual red-shifting due to the increase in symmetry of the shell. Initially, the cation exchange process does not affect the QD evenly. It occurs in sections and takes time to even out. The increase in symmetry causes the observed slight red shift and narrowing in the spectrum (from black to light blue).

1.3.1.1.1 Determining the Optimal CdSe Shell Thickness

To determine the optimum shell thickness of our QDs for our films, aging studies of the core shell nanoparticles were performed. First, the relative QY versus shell growth time was observed over the course of two weeks (Figure 19).

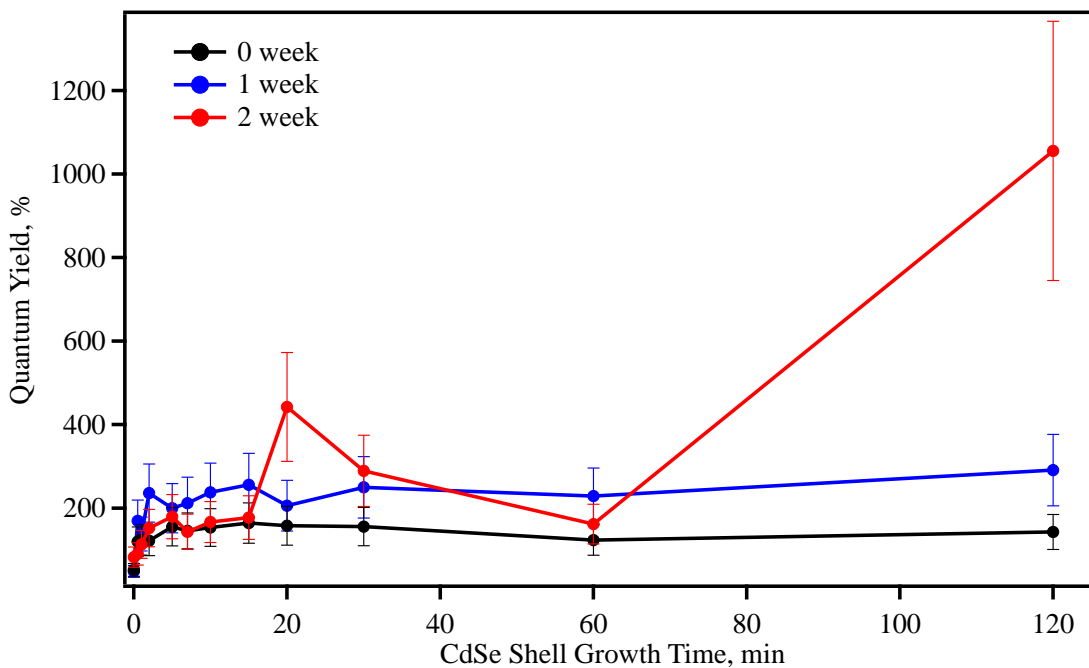
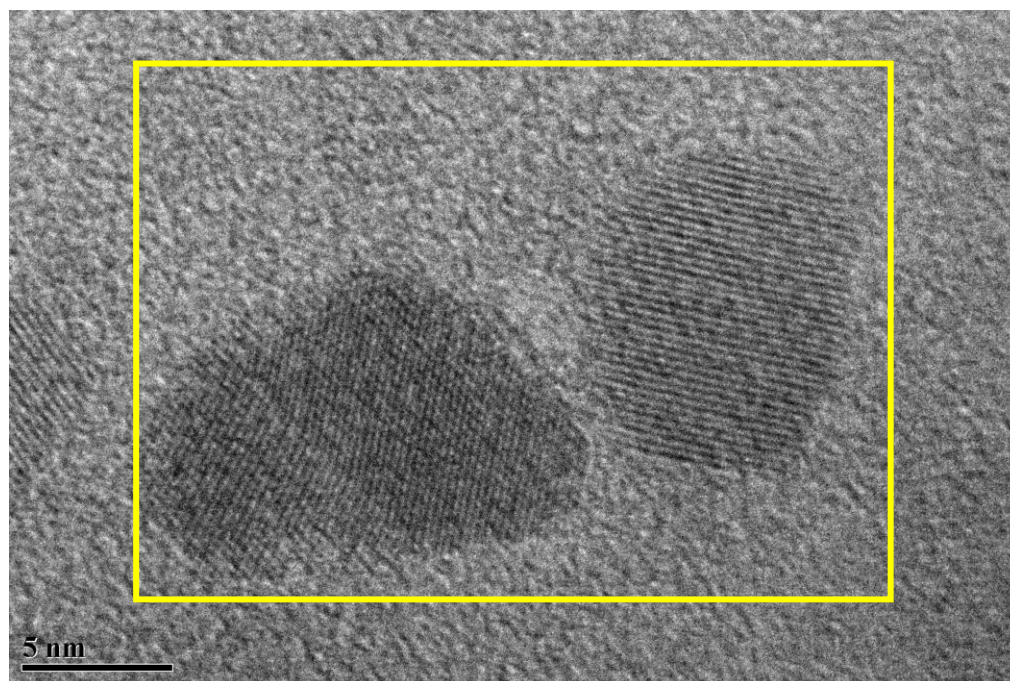


Figure 19: Calculated relative QY versus CdSe shell growth time at 625 nm excitation ($1.5E_g$) as the PbSe/CdSe QDs age in air for 0 weeks (black), 1 week (blue) and 2 weeks (red). Larger CdSe shells (longer growth times) have greater quantum yields.

There was an unexpected overall increase in the QY over time. This can be attributed to an alloying between the core/shell barrier, which would reduce trap states. TEM and EDX were taken of PbSe/CdSe samples with a 60-minute shell growth time (Figure 20). The TEM reveals the monocrystalline nature of the PbSe/CdSe QDs, which supports our hypothesis that there is core/shell alloying as they age. The elemental analysis confirmed cadmium present in the sample.



Element	Peak	Area	k	Abs	Weight%	Weight%	Atomic%
	Area	Sigma	factor	Cornn.		Sigma	
C K	32179	369	2.208	1.000	70.26	0.38	83.13
O K	6270	156	1.810	1.000	11.23	0.27	9.97
Si K	10671	182	1.000	1.000	10.55	0.19	5.34
Cl K	516	61	0.964	1.000	0.49	0.06	0.20
Cr K	148	36	1.100	1.000	0.16	0.04	0.04
Cu K	3757	105	1.366	1.000	5.07	0.14	1.13
Cd L	278	65	1.769	1.000	0.49	0.11	0.06
Pb L	636	62	2.775	1.000	1.75	0.17	0.12
Totals					100.00		

Figure 20: TEM and EDX elemental analysis of PbSe/CdSe core/shell QDs (60 min shell growth). In the TEM image, the scale bar is 5 nm and the yellow rectangle represents the area which the energy dispersive x-ray (EDX) elemental analysis was taken on. The copper, silicon, chromium, carbon, oxygen and chlorine signals arise from the sample grid and detector.

CHAPTER 1.4 HOW CAN WE EXCEED THE SHOCKLEY-QUEISSER LIMIT USING NEAR IR QDS?

Back in 1961, Shockley and Queisser determined the theoretical maximum PCE of PV devices with bandgaps of 1.1-1.4 eV to be 31-33 %.⁸⁵ These calculations operated with three assumptions: excess energy is thermalized to the band edge, the illumination is by 1 sun (unconcentrated), and each photon can produce only one e^-h^+ pair.⁸⁵ In 2006, Hanna and Nozik modeled the theoretical efficiency of single E_g devices, under 1.5 AM, that can perform MEG to be 44.4 %, which is 10.7 % greater than the Shockley-Queisser (SQ) theoretical limit of cells which cannot.^{85, 86} We can take advantage of MEG to exceed the SQ limit and spawn a highly efficient PV device.

1.4.1 Multiple Exciton Generation (MEG)

Conventionally, a solar cell can only excite one electron across the bandgap per photon absorbed; where any excess photon energy is lost as heat. One way of developing next generation solar cells is with cheap quantum dot materials that enable multiple exciton generation (MEG) to enhance photoconversion efficiencies. In this process a material can produce multiple excited states following the absorption of one high-energy photon, potentially increasing the photocurrent of a device.

When a photon of greater energy than the E_g is absorbed, the extra energy is dispersed between the charge carriers as kinetic energy.⁸⁷ The equations below describe this dispersion of energy with ΔE_e as the energetic difference between the electron and conduction band and ΔE_h as the difference between the hole and valence band energy.⁸⁷

$$\Delta E_e = (h\nu - E_g) \left[1 + \frac{m_e}{m_h} \right]^{-1}$$

The effective electron and hole masses are denoted as m_e , and m_h , respectively. Note that the energy of the incident light must be greater than the E_g for this dispersion of energy to occur.

$$\Delta E_h = (h\nu - E_g) - \Delta E_e$$

This equation describes the system at thermal equilibrium, which occurs very quickly (<100 fs).⁸⁷

$$\Delta E_e = \Delta E_h = 0$$

At this equilibrium, the electrons reside at the bottom of the conduction band and the hole resides at the top of the valence band with a Boltzmann distribution. Finally, the electrons and holes combine either radiatively or non-radiatively to form a completely relaxed system.

The rates of these processes after photoexcitation decide if certain phenomenon like multiple exciton generation is possible. The rates of carrier cooling, which are usually different between electrons and holes, must be slow compared to the rate of carrier multiplication.

1.4.1.1 Possible Quantum Mechanisms of MEG

MEG is a phenomenon where multiple excited states result from a single, high-energy photon. The quantum mechanics of MEG have been under some debate. The italicized mechanisms mentioned below are the least commonly mentioned propositions in the literature. The *coherent superposition of excited states* is attributed to strong coulomb interactions between e^-h^+ pairs in confined systems. For this to occur, the rate of

two-exciton thermalization and rate of Coulombic coupling must be greater than the relaxation rate of a single exciton.⁸⁸ *MEG through a virtual single exciton state* can be explained with second-order perturbation theory.⁸⁹ *MEG via optical intraband transitions* yielding virtual biexciton states.⁹⁰

The most common mechanism of MEG in QDs is described as impact ionization (II). The idea that II may enhance carrier multiplication in quantum-confined systems was first proposed by Arthur Nozik in the early 2000s.^{87, 91} A schematic of biexciton formation via II (A) and subsequent, opposite process, AR (B) is provided in Figure 21.⁹² The symbols η_x and η_{xx} represent the fraction of the population that generate single excitons, and undergo II to generate biexciton, respectively. Part C shows a model of dynamic carrier populations of PbSe excited at $>3E_g$. Immediately after excitation, at τ_0 , hot excitons are formed. Of those formed (at τ_1), half undergo II to form biexcitons, and half of the hot carriers relax to the band edge, thermally. By the time, τ_2 , all the biexcitons have decayed to the band edge via AR and cooling.

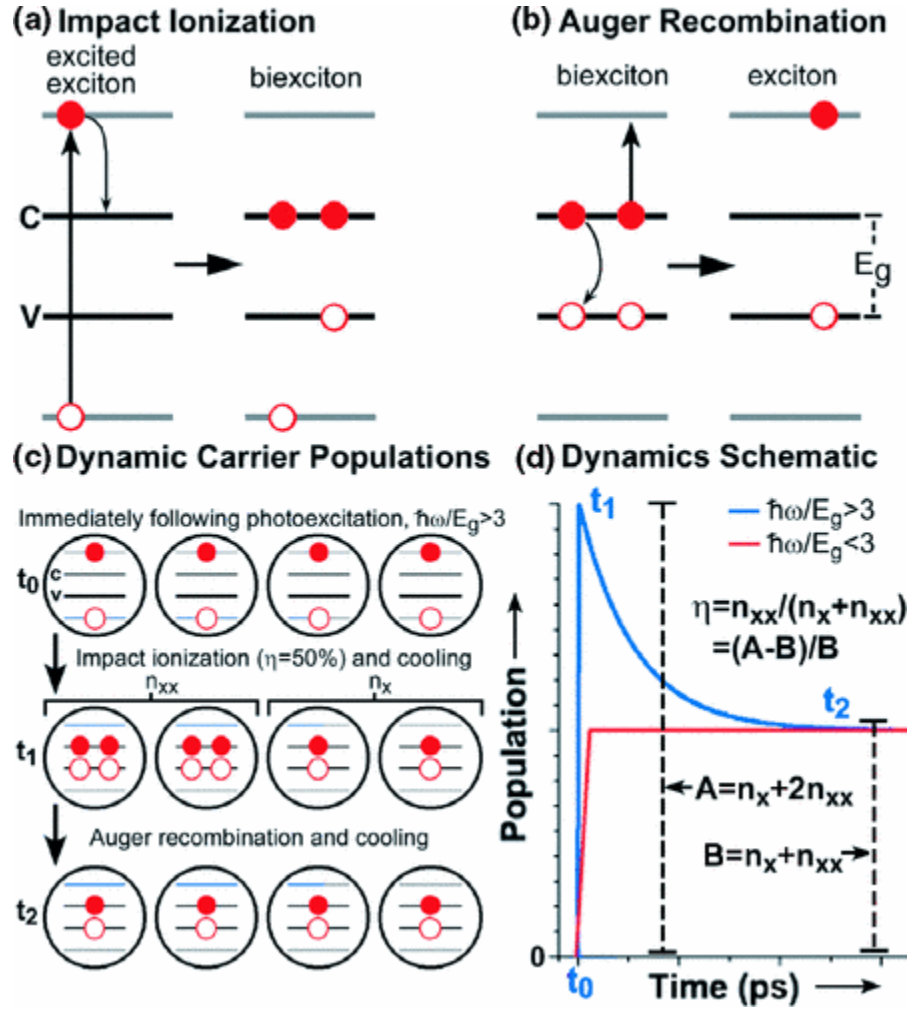


Figure 21: A) Impact ionization, B) Auger recombination, C) dynamic carrier populations following the excitation of PbSe QDs with photon of energy $> 3 E_g$. Filled and open red circles represent electrons and holes, respectively. C and V represent the conduction and valence bands. η_x and η_{xx} represent the fraction of the population that generate single excitons, and undergo II to generate biexciton, respectively D) dynamics schematic of time resolved data blue trace (excitation above MEG threshold) red trace (excitation below MEG threshold).⁹² "Reprinted (figure) with permission from (Schaller, R. D.; Klimov, V. I., High efficiency carrier multiplication in PbSe nanocrystals: Implications for solar energy conversion. *Physical Review Letters* 2004, 92 (18), 4.) Copyright (2004) by the American Physical Society.

Figure 21-D shows a dynamics schematic of time resolved data of samples excited above the MEG threshold (blue trace) and below the MEG threshold (red trace). The labeled times, τ_0 , τ_1 , and τ_2 correspond to populations in part C. The fast decay component in the blue curve from τ_0 to τ_1 , can be attributed to AR. MEG in PbS has also

been widely observed. It has been described as bulk-like and less sensitive to surface properties which affect AR.⁹³ The very first publication demonstrating MEG was with PbSe QDs (excited at $\geq 3E_g$) in 2004.⁹²

1.4.1.2 MEG in PbSe QDs

MEG has been reported in various QD materials such as CdS, CdSe, InAs, PbS, and even Si^{94,95}. Since then, PbSe QDs have been found to be highly efficient at MEG; Schaller et. al reported the generation of 7 excitons when excited at $7.8E_g$!⁹⁶ However, they generate, on average three excited states per photon absorbed with the energy at least $4 E_g$.² A mechanism of incoherent MEG in PbSe QDs when excited at $3 E_g$ was proposed by Ellingson et. al. and is shown in Figure 22.²

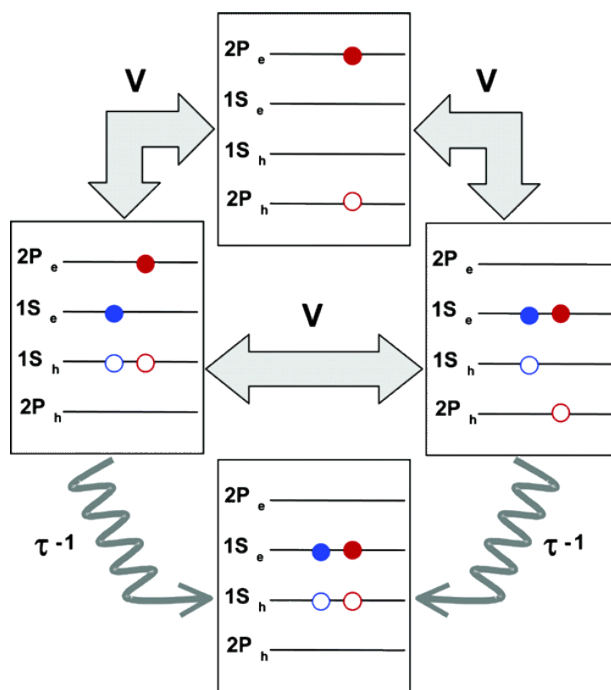


Figure 22: Incoherent multiple exciton generation model in PbSe QDs at $3E_g$ excitation energy.² Reprinted (adapted) with permission from (Ellingson, R. J.; Beard, M. C.; Johnson, J. C.; Yu, P. R.; Micic, O. I.; Nozik, A. J.; Shabaev, A.; Efros, A. L., Highly efficient multiple exciton generation in colloidal PbSe and PbS quantum dots. *Nano Letters* 2005, 5 (5), 865-871). Copyright (2005) American Chemical Society.

Within 250 fs, the $2P_e-2P_h$ exciton formed mixes with multiple excited states matrix element (V), and generates coherent multiexciton states.² These asymmetric states then quickly dephase via phonon coupling at a rate of τ^{-1} . In this model, MEG efficiency is determined by the ratio of dephasing rates of the coherently coupled single and multiexcitons.² A question of this phenomenon regarding our research is: how can we maximize the efficiency of solar cells with MEG?

CHAPTER 1.5 HOW CAN WE IMPROVE SOLAR CELL EFFICIENCY WITH MEG?

The whole point of a solar cell is to utilize photons to generate the flow of electrons, or current to later be used as electricity. Solar cells that can perform MEG essentially have the ability to generate at least twice the current than cells that cannot. In addition to generating more current, solar cells that can perform MEG should have a greater long-term stability. This is because excess energy from photons that hit cells that cannot perform MEG is lost by thermalization. The loss of heat to the lattice in non-MEG solar cells can cause the cell to degrade more quickly.

We can boost a materials ability to perform MEG by changing the material's shape. This is because the shape of a nanomaterial determines its confinement i.e. the common particle in a box p-chem problem.

1.5.1 Boosting MEG with Nanoparticle (NP) Confinement

MEG in bulk semiconductor systems is relatively inefficient because angular momentum of the wavefunction needs to be conserved, and the process must compete with the very fast process of electron-phonon scattering.² The conditions are more relaxed for confined systems (e.g. 3-D confined QDs) because the angular momentum is not a good quantum number and the increased Coulombic interactions lead to more Auger processes, including MEG.²

Nanoscale materials can exhibit quantization in three dimensions (QDs), two dimensions (nanowires/nanorods), or one dimension (quantum films/platelets).⁹⁷ Unlike QDs, the anisotropy of electric field and charge distribution in 2-D and 1-D systems

causes enhanced Coulombic interactions and MEG.⁹⁸ A comparison of MEG efficiency in and threshold in quasi-1-D confined and 3-D confined PbSe is shown in Figure 23.⁹⁹

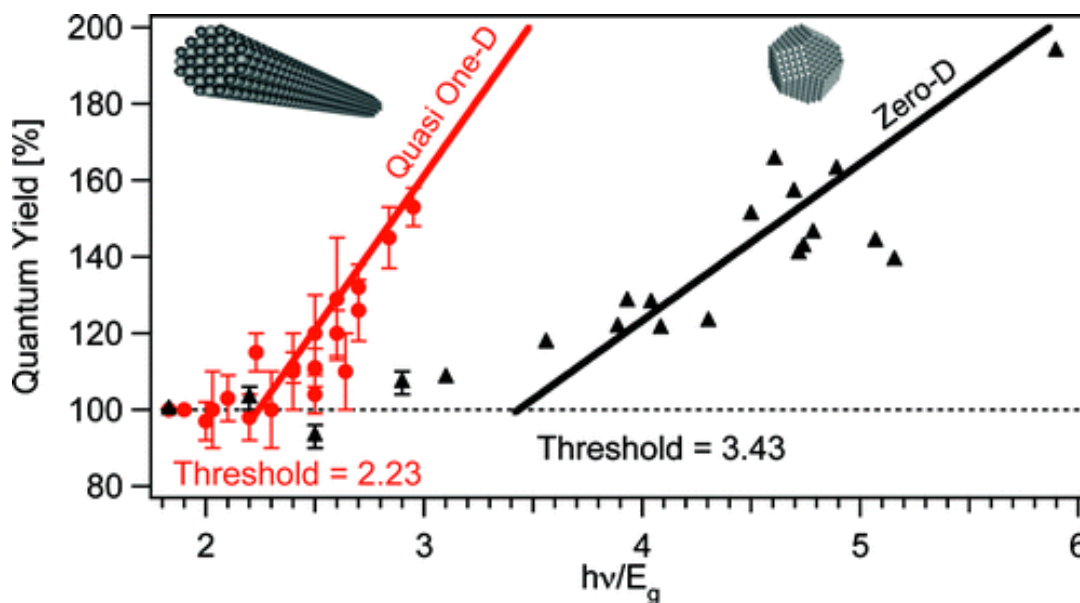


Figure 23: MEG in PbSe nanorods (red curve) and QDs (black curve); QY versus excitation energy. The horizontal dashed line represents where the NPs exhibit a 100 % QY. Anything above that line represents MEG. The point at which the energy (x-axis) and the dotted line intersect represents the minimum threshold energy for MEG to occur.⁹⁹ Reprinted (adapted) with permission from (Cunningham, P. D.; Boercker, J. E.; Foos, E. E.; Lumb, M. P.; Smith, A. R.; Tischler, J. G.; Melinger, J. S., *Enhanced Multiple Exciton Generation in Quasi-One-Dimensional Semiconductors*. *Nano Letters* 2011, 11 (8), 3476-3481 Copyright (2011) American Chemical Society.

The MEG threshold energy is lower and the efficiency is 2-fold greater of the PbSe nanorods than QDs. MEG in one dimension has been highly efficient in PbS nanosheets¹⁰⁰, CdSe nanoplatelets¹⁰¹ which can attribute to strong optical transitions and much slower (relatively) AR times. How can we make sure as much energy above the MEG threshold makes it into our semiconductors?

CHAPTER 1.6 CAN WE INCREASE LIGHT ABSORPTION ABOVE THE MEG THRESHOLD?

So, we now know that MEG can increase solar cell efficiencies and we can increase MEG efficiency and lower the threshold with increasing confinement. Naturally, the next thing we want to know is how to push more light into our material that is energetically above the MEG threshold in hopes to create even more excited states in our system.

A direct way of increasing a materials absorption is by making it thicker. Unfortunately, making our absorbing material thicker defeats one of our main overall goals; which is developing cheaper devices that can compete with current PV. Surface plasmon resonances may allow us to make lead-based QDs absorb more above the MEG threshold without the need to make our absorbing material thicker

1.6.1 Metal Nanoparticles Surface Plasmon Resonance

Beginning in the 1800s following experiments conducted by Michael Faraday using gold nanoparticles, noble metal nanoparticles have been of scientific interest due to their unique optical properties.¹⁰² The unique optical properties of “coinage” (e. g. gold, silver, and copper) metal nanoparticles (NPs) arise from the interactions between the confined, conductive electrons with electric fields.¹⁰³ Specifically, the excitation of a metal NP at a respective wavelength generates a confined and coherent oscillation of conductive electrons also known as a surface plasmon resonance (SPR). In 1908, Gustav Mie used the Maxwell equations to describe the absorption and scattering of light

incident to a < 200 nm sphere in an attempt to compare theoretical results to what one of his Ph. D. students was observing with Au NPs, experimentally.¹⁰⁴

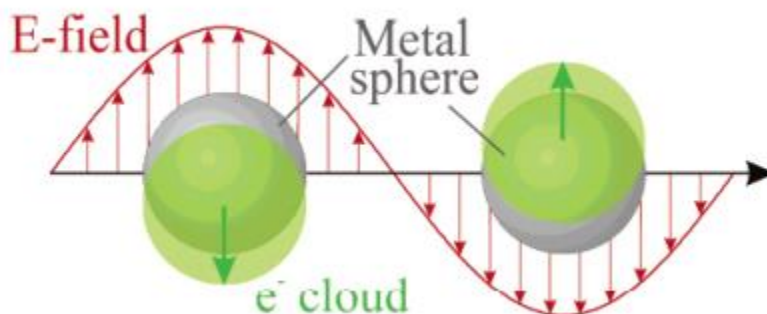


*Figure 24: Illustration of a surface plasmon resonance for a spherical nanoparticle where electron charge is displaced. The red curve represents the strong localized electric field caused by the coherent oscillation of electrons. The grey and green spheres represent the metal NP and electron cloud, respectively.⁴ Reprinted (adapted) with permission from (Kelly, K. L.; Coronado, E.; Zhao, L. L.; Schatz, G. C., *The optical properties of metal nanoparticles: The influence of size, shape, and dielectric environment. Journal of Physical Chemistry B* 2003, 107 (3), 668-677). Copyright (2003) American Chemical Society.*

In the case of light contacting small, spherical, metallic NPs (Figure 24), the oscillating electric field causes the free electrons to oscillate coherently. When the electron cloud is pushed away from the nucleus, a coulombic attraction pushes the cloud back toward it which gives rise to the dipolar plasmon resonance.⁴

Larger particles have a quadrupolar plasmon resonance, which can be visualized in the electric field contour calculations in Figure 25-B. In Figure 25 of the Ag NP cross-sections, A and B contain the propagation and polarization axes and C and D contain the plane perpendicular to the propagation axes.⁴ The p-orbital shape of the field around smaller sphere is due to the wavelength chosen (369 nm, the dipolar plasmon peak) causing the dipole field to dominate. The quadrupole plasmon resonance (part B) looks like a d_{xz} orbital, while the plane perpendicular to the propagation axis (part D) contains the node and a very weak dipole component.⁴ The small amount of asymmetry in the

electric field contours is due to a small quadrupole component in the 30 nm sphere, and a small dipole component in the 60 nm sphere.⁴

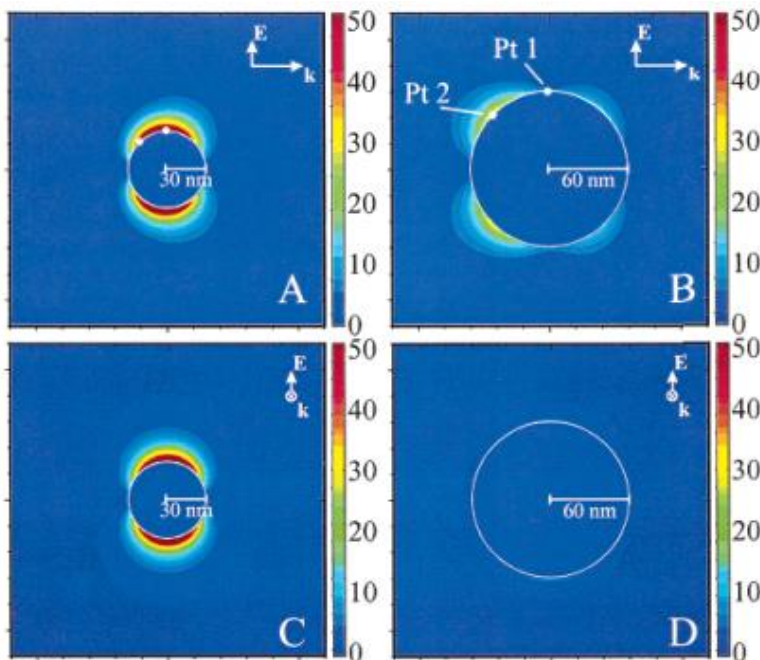


Figure 25: Mie theory calculated electric field contours of 30 nm (A and C) and 60 nm (B and D) Ag spheres with 369 nm and 358 nm light, respectively. The different colors (blue to red) represent an increase in electric field strength.⁴ Reprinted (adapted) with permission from (Kelly, K. L.; Coronado, E.; Zhao, L. L.; Schatz, G. C., *The optical properties of metal nanoparticles: The influence of size, shape, and dielectric environment. Journal of Physical Chemistry B* 2003, 107 (3), 668-677). Copyright (2003) American Chemical Society.

Mie's equation for the extinction cross-section, C_{ext} of a metallic NP which has a radius, R much smaller than the wavelength of light, λ is given in the equation below.¹⁰⁴

$$C_{ext} = \frac{24\pi^2 R^3 \epsilon_m^{1.5}}{\lambda} \frac{\epsilon_i}{(\epsilon_r + 2\epsilon_m)^2 + \epsilon_i^2}$$

In this equation, ϵ_m is the refractive index of the surrounding media; ϵ_r and ϵ_i represent the real and imaginary part of complex dielectric function of the particles ($\epsilon = \epsilon_r + i\epsilon_i$), respectively.¹⁰⁵ Due to the presence of dipolar coupling in thin films of metal NPs, Maxwell-Garnet came up with an expression for the transmittance of a thin film¹⁰⁶:

$$T_{film} = \frac{(1 - R)^2 + 4R\sin^2\Psi}{R^2 \exp(-\alpha h) + \exp(\alpha h) - 2R\cos(\zeta + 2\Psi)}$$

In equation 6, R is the reflectance at normal incidence, Ψ is the metal volume fraction, α is the absorption coefficient, and h is the film thickness. As Ψ and h increases, the film transmittance decreases This suggests that films of greater metal NP density will scatter and absorb more light than those with less density.

Interactions like SPRs induce high-angle scattering and concentrated electromagnetic fields within the metal NPs; thus, causing an increase in the fluorescence and absorption efficiency of a nearby fluorophore. Many applications, including enhanced fluorescence activation¹⁰⁷, SERS,¹⁰⁸⁻¹¹⁰ biosensing,¹¹¹⁻¹¹⁵ bioimaging,¹¹⁶⁻¹¹⁹ and LEDs^{120, 121} have utilized these unique properties.

For example, the amplified absorption and fluorescence caused by metal NPs, which would otherwise be lost in the background signal or rapidly bleached, can allow for highly sensitive biosensors and bioimagers for heterogeneous assays.¹²² For SERS, the Raman scattering cross-section of a molecule can increase by 10 orders of magnitude when metal NPs are present (compared to without).¹²³ For bio-detecting agents, thin silver film and gold nanohole arrays caused an increased fluorescence enhancement factor by 170-fold¹¹² and 100-fold,¹²⁴ respectively.

Additionally, recent research has shown the ability of metal NPs to increase the intensity, efficiency, and charge transport properties of light emitting diodes (LEDs). Deep ultraviolet, AlGaIn-based LEDs had a 2.6-fold emission enhancement when decorated with Aluminum NPs.¹²⁵ The addition of gold NPs to perovskite LEDs caused a 226 % enhancement in the maximum luminescence and an 86 % enhancement in current

efficiency.¹²⁶ The photoresponse of a reduced graphene oxide/silicon photodetector was enhanced by 30 times at 382 nm when gold NPs were incorporated.¹²⁷ The presence of silver nanoclusters in blue, organic LEDs led to an enhancement of current efficiency by 15 % compared to the control.¹²⁸

Various shapes of nanoscale metals have also enhanced the reverse process in LEDs: converting light into electricity. At the single particle level, metal NPs have increased nearby fluorophores fluorescence intensity by a factor of 1,340 by Au nanobowties¹²⁹ and 1,100 by Au nanorods (NRs)¹³⁰ Metal NPs can also increase fluorophores photo-stability by increasing their radiative decay rates by a factor of 10-100;¹³¹ making them ideal candidates to aid in the creation of thinner, cheaper, and more efficient solar devices.¹⁰³ Organic solar cells equipped with gold NPs and silver nanogratings yielded a power conversion efficiency of 8.79 ± 0.15 % compared to the control (without metal NPs) of 7.59 ± 0.08 %.¹³² The addition of Ag NPs to donor-acceptor polymer bulk heterojunction (P3HT/PC₇₀BM) solar cells caused an increase in charge transport and thus PCE from 3.54 to 4.36 %.¹³³ The addition of silver NPs into Graetzel solar cells caused the PCE to more than double from 0.0082 % to 0.01734 %.¹³⁴ All in all, metal NPs have shown to enhance the absorption, fluorescence, charge transport, and decay rates of various devices across disciplines.

Since surface plasmon resonance (SPRs) are generated from the nanoscale features of the surface, they are very sensitive to changes on the surface. Jiawei He et. al. utilized this sensitivity by using SPRs to measure binding affinities and interactions between human serum albumin (immobilized on gold surface) and carthamin.¹³⁵ This

work focuses specifically on enhanced solar devices. Surface plasmons can also cause the production of radiation of nearby charged particles, termed the Purcell effect.

1.6.2 Purcell Effect

In 1953, S. J. Smith and E. M. Purcell published a paper describing a produced radiation (visible light) when a charged particle moved very close and parallel to a metal diffraction grating.¹³⁶ A figure describing the experiment is shown in Figure 26.

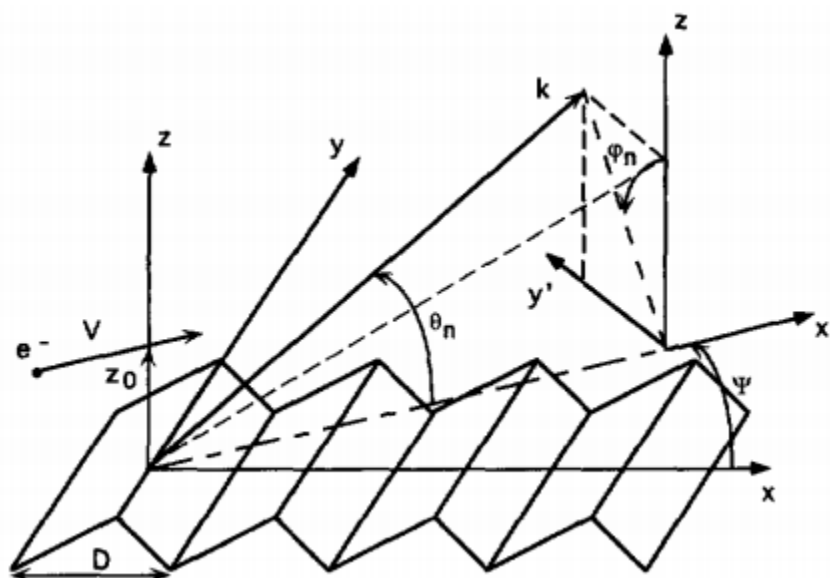


Figure 26: Configuration of Smith-Purcell experiment. The lower area represents a grating with a periodicity of D . The arrows represent the path of an electron (e^-) traveling at velocity, V and at an angle, ψ across the grating.¹³⁷ Reprinted from Haeberle, O., Reciprocity theorem for Smith-Purcell radiation. *Optics Communications* 1997, 141 (5-6), 237-242. Copyright (1997), with permission from Elsevier.

In this figure, the electron moves at a constant velocity, V at an angle, ψ relative to the grating. Since this discovery, scientists have aimed to control and enhance the spontaneous emission of fluorophores with the surroundings.¹³⁸ SPRs can be used as an antenna to push more light into fluorophores. With the addition of metallic nanoparticles, a silicon tandem thin film solar cell experienced a 56 % absorption enhancement with a

decrease in the active layer thickness from 1750 to 750 nm.¹³⁹ Au NPs specifically placed Co_3O_4 films have shown an enhancement in photocatalytic activity compared to films without the Au NPs.¹⁴⁰ This enhancement was attributed to SPR coupling.

We can use this type of enhancement caused by SPRs to increase the spontaneous emission in our particles. Other than concentrating light into nearby fluorophores, particles with SPRs are also excellent light scatterers. Au NPs have been added to CuInS_2 films and increased absorption due to the scattering effect of the metallic nanoparticles.¹⁴¹ Though our main intention is to use the SPRs to concentrate light, we can use this to our advantage because in increasing the optical path length of incident light we are increasing the chances for our thin layer to absorb the light.

1.6.3 Increasing the Optical Path Length with SPR Light Scattering

Metallic nanoparticles can also enhance the absorption of absorbing layers by simply acting as scattering centers. The incident light goes into the film, is scattered by the metallic NPs at high angles, which allows the absorbing material more chances to absorb the light (Figure 27).

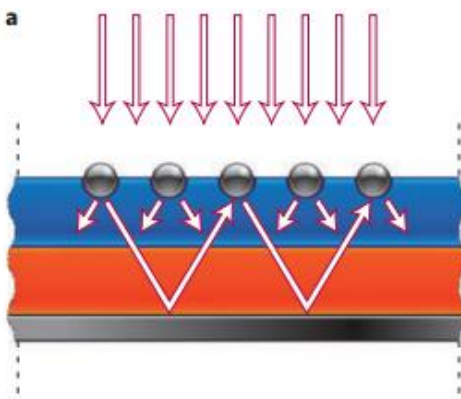


Figure 27: Light trapping geometry of plasmonic nanoparticles (grey sphere) in a layered (glue and orange) thin film solar cell. The arrows represent the path of the incident light. The presence

of metal nanoparticles cause an increase in optical pathlength through the device.⁹ Reprinted by permission from [Atwater, H. A.; Polman, A., *Plasmonics for improved photovoltaic devices. Nature Materials* 2010, 9 (3), 205-213.] [COPYRIGHT] (2010).

In Figure 27, light hits the metal NPs at the surface of the device and is trapped by high angle scattering. This scattering can be controlled by the size/shape of the metal NPs and/or the dielectric constants of the surrounding material.

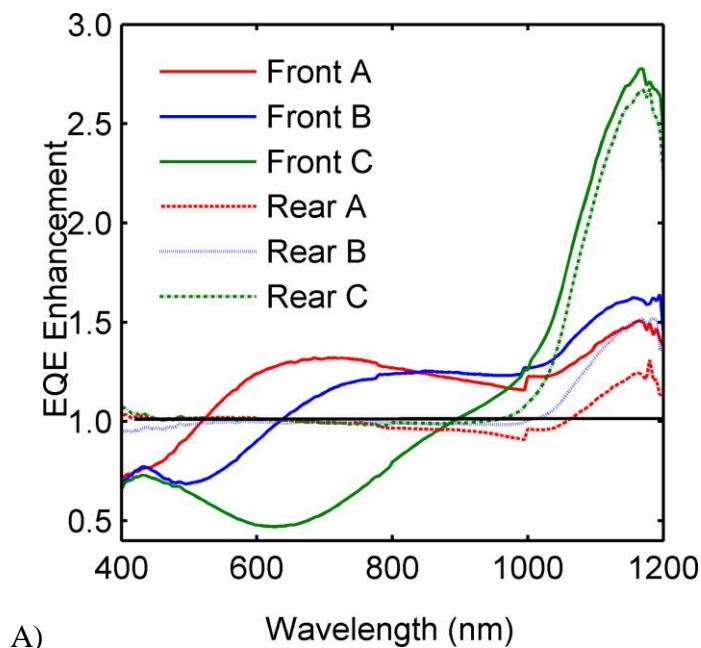


Figure 28: A) External quantum efficiency enhancements of Si wafers due to the presence of 50 nm Ag nanoparticles for samples with different top layers: SiO_2 on sample A, Si_3N_4 on sample B, and TiO_2 on sample C. The solid curves represent when the samples were irradiated from the front and the dashed were irradiated from the rear.¹⁴² Reprinted from [Beck, F. J.; Polman, A.; Catchpole, K. R., *Tunable light trapping for solar cells using localized surface plasmons. Journal of Applied Physics* 2009, 105 (11)], with the permission of AIP Publishing.

In Figure 28, the refractive indices of samples A, B, and C are 1.5, 2, and 2.5, respectively. Sample C (TiO_2), with the highest refractive index showed the greatest enhancement at > 900 nm due to the redshift in the SPR.¹⁴² All samples showed EQE enhancements above the Ag SPR due to light trapping and a decrease in EQE below due

to interferences. Furthermore, the enhanced absorption in these devices due to SPR light scattering agreed with the modeled FDTD (finite-difference time-domain) calculations.¹⁴²

Overall, the EQE enhancements were greatest when the samples were excited from the front. We kept this in mind when designing our layered system. This work tells us that not only can we push more light above the MEG threshold, but we can use the scattering abilities of metallic NPs to increase absorption of our proposed fluorophores in general.

1.6.4 Coupling of Metal Nanoparticles to Quantum Dots

The enhancement of solar devices involves three mechanisms: (i) increasing absorbance by light trapping via high angle scattering of NPs⁹, (ii) increasing radiative decay rates by metal enhanced fluorescence (far field), or (iii) increasing excitation due to SPR enhancement (near field). Each mechanism is dependent on the plasmon wavelength of metal NPs, which can be tuned by changing the size and shape of the NP, altering the dielectric environment and modifying distance between particles. Changes to the surface of a metal NP can elicit shifts in the extinction spectrum. Jiawei He et. al. utilized this property by measure binding affinities and interactions between human serum albumin immobilized on gold surface and carthamin by observing SPR shifts.¹³⁵ Blake et. al. demonstrated theoretically and experimentally that the plasmon of a gold NP array can be controlled by changing the interparticle distances (< 20 nm).¹⁴³ This causes the individual plasmons to couple together, drastically changing the wavelength and sensitivity.

Multiple nanoparticles in close proximity exhibit a highly sensitive and coherent plasmon coupled resonance.¹⁴⁴ The concentrated electric field between the NPs causes

strong red-shift in the plasmon peak.¹⁴⁵ Coupled plasmon resonances can be best described by the coupled dipole approximation, while larger particle separations can be estimated by the discrete dipole approximation.¹⁴⁵ This makes it possible to control the plasmon absorption and scattering of metal NPs by altering the interparticle distances, and not the size.

1.6.4.1 Role of NP Scattering Efficiency in QD Absorption Enhancement

Mie theory predicts the extinction (σ_{ext}), the sum of the absorbance and scattering ($\sigma_{absorbance} + \sigma_{scattering}$), of metal nanoparticles to be dependent on the particle radius cubed (R^3).¹⁰⁴ Once irradiated with light, the likelihood of metal NPs (like Au NPs, $\epsilon = 6 \times 10^9 \text{ cm}^{-1}\text{M}^{-1}$)¹⁴⁶ absorbing or scattering that light is about four orders of magnitude greater than quantum dots (like CdSe QDs, $\epsilon = 5 \times 10^5 \text{ cm}^{-1}\text{M}^{-1}$)¹⁴⁷ due to their large extinction coefficients. Smaller NPs are predicted to predominately absorb extincted light, while larger particles are expected to scatter much more efficiently than smaller ones due to the R^6 (radius) dependence.¹⁰⁴ Larger silver NPs, like silver nanorods, are especially attractive due to the appearance of higher order modes which cause the scattering ability to overshadow absorption to an even greater degree.¹⁴⁸ This is an unfortunate case for layered metal NP film applications because a smooth, homogenous film (which requires small NPs) is necessary to keep the NP-fluorophore distances consistent.

In project II, we want to fabricate tunable, homogeneous, and colloidal-monolayer films for enhanced solar applications. Since individually, small metal NPs do not scatter light very well, we took advantage of the sensitivity of the coherent plasmon resonance of

the film. The plasmon absorption and scattering properties were controlled via altering the interparticle distances. We are most interested in the scattering efficiency (Q_{sca}). This value represents the proportion of extincted light which is scattered.¹⁴⁹

$$Q_{sca} = \frac{\sigma_{sca}}{\sigma_{abs} + \sigma_{sca}}$$

We aimed to maximize Q_{sca} of the metal NP films at various relevant wavelengths to optimize the enhancements of fluorophore performance.

The scattering ability of metal NPs can (i) increase the optical path length of incident light¹⁴² and (ii) can lead to metal enhanced fluorescence (MEF).¹⁵⁰ Metal NPs can scatter incident light in all directions, which increases the likelihood of absorption by nearby fluorophores. In the second case, MEF, energy can be rapidly transferred from a fluorophore to a nearby plasmon, which then radiated back into the far field.

Conversely, absorption by the metal is parasitic due to the direct absorption of the energy. With our approach we aim to control the losses due to absorption. For MEF to occur, the scattering of the metal NPs must trump the absorption cross-section at the wavelengths of interest.¹⁵¹ Groups that use calculated scattering coefficients using Mie theory have found that the parasitic absorption is underestimated. Another problem with calculating the scattering efficiency is the assumption of homogeneous dielectric surroundings-which is not the case in colloidal suspensions due to ligands and the solvent.

1.6.4.2 Silver: The Best Nanoparticle for the Job

Compared to other noble metal NPs such as gold, silver NPs are the most attractive contenders for MEF due to their promising scattering efficiencies paired with

relatively low parasitic absorption.¹⁴⁸ Many groups have reported the fabrication for silver NP films. Dewetting, the most common method to fabricate silver NP films, is a spontaneous and spinodal process.¹⁵² In this method, silver, which has been evaporated onto a substrate, is annealed to form silver nano-islands. However, the major disadvantage with this method is the silver NP loading is dependent on the silver NP size and spacing, which are difficult to control.¹⁵² In another common method, nanosphere lithography (NSL), self-ordered polymeric NPs are used as a mask for NP deposition.¹⁵³ Though NSL is great for controlling the size, shape, and interparticle distances of metal NPs, the mask limits all of these properties.

The colloidal approach can alter the shape, size, and coverage of our silver nanoparticle films independently and without limitations.¹⁵⁴ Although, colloidal monolayer films can be difficult to fabricate due to a tendency to aggregate, in this work, we have developed a facile, colloidal approach toward monolayer silver NP films. With this degree of control, we can correlate the films structure to the optical properties. The absorbance and scattering of metal NPs can be tuned by changing their size, shape, and dielectric surroundings. In addition, monolayer films of metal NPs have enhanced optical responses due to plasmonic resonance coupling phenomena.¹⁵⁵ This field can couple to fluorophores and enhance the absorption, non-radiative, and radiative rates.

1.6.4.3 SPR Effects on Fluorophores Lifetime

It is well known that a signature of fluorophore-SPR coupling is a rapid decrease in lifetime.^{151, 156} The lifetime is shortened due to the increase in radiative and non-

radiative decay rates. The impacts of SPRs on the QD lifetime (τ_1/τ_0) can be described in the equation below.¹⁵⁷

$$\frac{\tau_1}{\tau_0} = \frac{1}{f_t \times \eta_1 + 1 - \eta_1}$$

In this equation, τ_1 and τ_0 represent the QD lifetime with and without the presence of a SPR, respectively. In addition, f_t and η_1 represent the enhancement factor and the quantum yield, respectively. This relationship shows that if the SPR causes an increase in f_t and η_1 , the shorter the lifetime (τ_1). This phenomenon can be seen in the work of Fu et. al. (Figure 29) where a) represents a single molecule lifetime in the presence of Ag nano-shells and b) alone on glass.¹⁵⁸

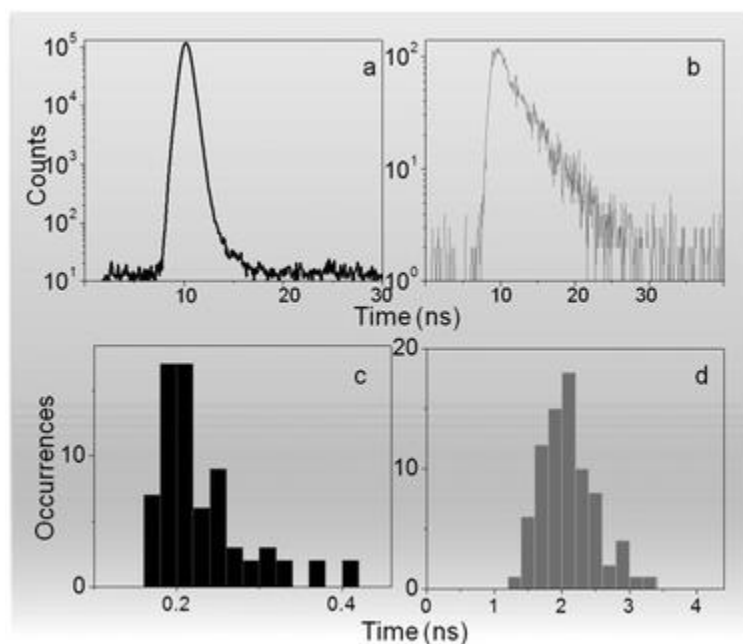


Figure 29: TCSPC curve of a single molecule fluorophore a) near Ag metal nano-shell versus b) on glass alone and corresponding histograms of decay times (c-d)¹⁵⁸ Reproduced from Fu, Y.; Zhang, J.; Lakowicz, J. R., Large enhancement of single molecule fluorescence by coupling to hollow silver nanoshells. *Chemical Communications* 2012, 48 (78), 9726-9728. with permission from the Royal Society of Chemistry.

The shortening of fluorophore lifetime can mean more photons can be harvested in a solar device and the fluorophore will be less prone to photooxidation because it spends less time in the excited state. We will include TCSPC studies at various metal SPR-fluorophore distances to prove that we have the distance-dependent coupling that we expect.

1.6.5 Plasmonic Enhanced Multiple Exciton Generation

Various other research groups have aimed to use the strong electric field of metal NP SPRs to enhance photoabsorption of QDs and thus MEG.¹⁵⁹⁻¹⁶⁴ In 2018, Shaik et. al. showed that Au nanoprisms could boost absorption and MEG in CdSe/CdS core/shell QDs. Their work showed that when in the presence of the SPR, the two-electron photoreduction reaction catalyzed by the QDs had faster kinetics and better yields than without SPRs.¹⁶⁰ Swayandipta et. al. and LeBlanc et. al. studied the plasmonic effect on MEG in single (visible) QDs. Both groups found an increase in MEG (through antibunching experiments) and a suppression of blinking in the QDs when in the presence of Au NPs.^{157, 159, 165}

CHAPTER 1.7 SUMMATION/RESEARCH AIMS

We are interested in the development of novel, more efficient, cheaper, and thinner solar devices than the current state-of-the-art. We want to utilize lead-based QDs as absorbers because we can tune them to absorb well into the near infrared and they can efficiently generate multiple excited states with light $\geq 2.5 E_g$. To increase the quantum yield and long-term stability, we will synthesize PbSe core-only QDs from a CdSe template. We propose to increase the light absorption at energies and below the MEG threshold in the lead-based semiconductors using the light concentration and scattering abilities of surface plasmon resonances in colloidal metal nanoparticles.

The aim of this research is to examine the potential of surface plasmon resonances to enhance photo-absorption rates in NIR QDs at a wide range of frequencies to enable thinner, more efficient solar cells.

In our work, there is no overlap between the emission of the PbSe QDs and the SPRs of the Ag NPs. However, there is overlap between the SPR and the QD absorption. We aim to enhance the photoabsorption of the QDs in general, and then specifically above the MEG threshold.

SECTION 2 RESEARCH

CHAPTER 2.1 OVERALL GOALS

Specifically, I studied how we can use SPRs to enhance photoabsorption in near IR, PbSe QDs by first enhancing the absorption at a range of frequencies and then tuning the system to above the MEG threshold. The motivation is illustrated in Figure 30, where Ag NPs, crystalline Si, and PbSe QDs absorption are compared to the spectral irradiation of the sun at 1.5 global air mass.

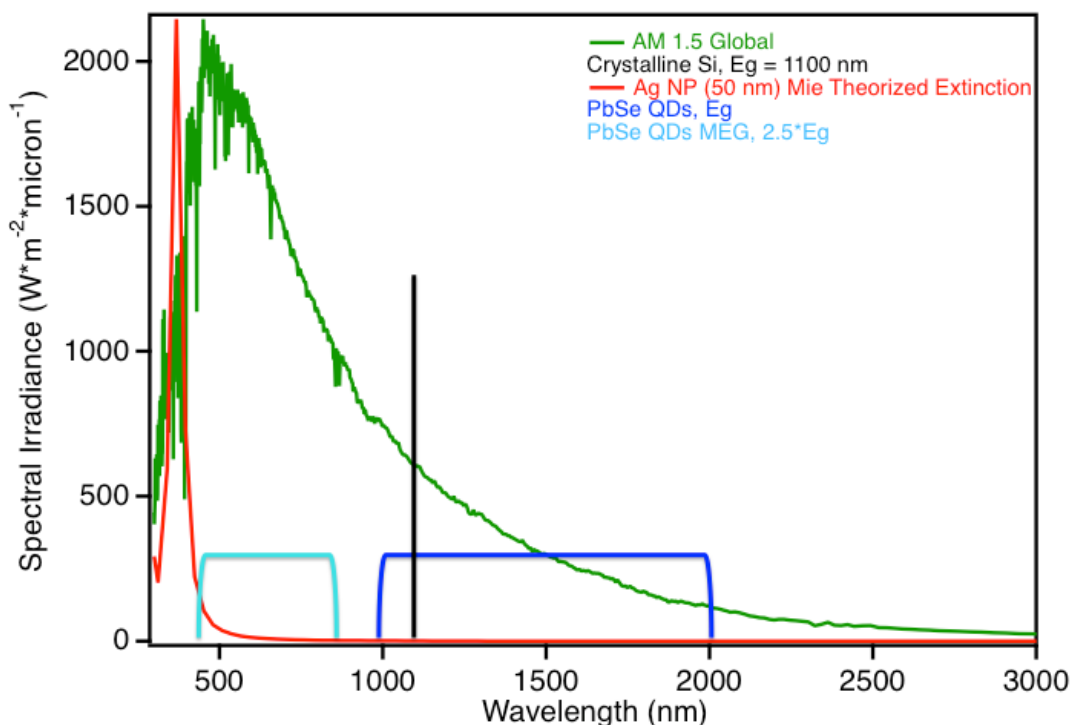


Figure 30: Comparison of silicon absorption (black line) to our system (PbSe QDs and Au) and the spectral irradiance at air mass 1.5 global (green curve) versus wavelength (nm). The dark blue range represents the range that PbSe QDs bandgap can be tuned to absorb. PbSe QDs have the potential to absorb more of the solar spectrum than conventional silicon can. The light blue range represents the energies that are suitable for MEG in PbSe QDs. There are plenty of photons from the sun (green curve) with energies suitable to generation multiple excitons in PbSe QDs. The red curve represents the Mie theorized absorbance of 50 nm diameter silver nanoparticles. The red curve is to show that the surface plasmon resonance of silver NPs can boost absorption rates in the QDs; even above the MEG threshold.

Near IR emitting QDs such as PbSe can be tuned to absorb many of the near IR photons (Figure 30-dark blue range) from the sun that bulk Si (black line) cannot. We aimed to generate a system capable of harvesting more of the sun's energy and at greater rates than conventional Si solar cells can. Moreover, there are many available photons at and above the MEG threshold (2.5 Eg, Figure 30-light blue range), which overlaps beautifully with the Ag SPR absorption profile. We used the SPR of Ag to increase the photoabsorption of QDs at many frequencies. Furthermore, the SPR of Ag can be tuned above the MEG threshold of the QDs to possibly enhance the importance of MEG. There is arguably a great benefit for a solar cell device that can utilize many of the sun's photons, even with the cost of a lesser open circuit voltage.

2.1.1 Mechanisms of Plasmonic MEG Enhancement

Theoretical studies of Swayandipta et. al. suggested that there are two mechanisms of plasmonic MEG enhancement: 1) the enhanced excitation rates of biexcitons relative to single excitons and 2) biexciton QY increased while the single exciton QY decreased.¹⁵⁷ The equations below show the theorized relationship between the single and biexciton QD emission intensity with (I_1) and without (I_0) a nearby SPR, respectively. It is important to note the excitation rate enhancement $|E|$ of the QDs due to the nearby strong electric field of the SPR.

$$\frac{I_1}{I_0} = |E|^2 \frac{f_r}{f_t \times \eta_1 + 1 - \eta_1}$$

Equation 9 shows that the change in emission intensity due to a SPR is proportional to the excitation rate enhancement squared, $|E|^2$.

$$\frac{I_1}{I_0} = |E|^4 \frac{f_r}{f_t \times \eta_1 + 1 - \eta_1}$$

The relationship between the emission intensity ratio due to nearby SPRs is proportional to excitation enhancement factor, $|E|^4$. The symbols f_r and f_t in the previous equations are given by the equations below.

$$f_r = \frac{k_r'}{k_r}$$

F_r represents the ratio of radiative rate with (k_r') and without (k_r) the presence of a nearby SPR. F_r can be seen as the radiative rate enhancement factor. F_t is equal to sum of F_r and the ratio of the nonradiative energy transfer rate from the QD to the metal NPs (k_{SPR}) and the radiative rate with an SPR present (k_r')

$$f_t = f_r + \frac{k_{SPR}}{k_r'}$$

Our work capitalizes on the first mechanism of MEG enhancement by SPRs: the fact that they cause exponential excitation rate enhancements in nearby QDs.

Furthermore, the excitation rate enhancement, or absorption enhancement, is exponentially greater for biexcitons than that of single excitons. We will aim to use the predicted excitation enhancement rates caused by nearby SPRs to improve overall absorption of near IR QDs.

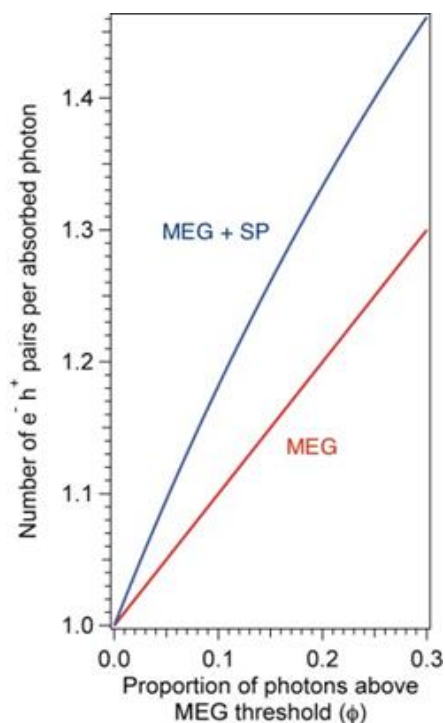


Figure 31: Potential Effect of SPRs on e^- and h^+ generation after MEG.

Number of charge carriers per absorbed photon versus proportion of photons above MEG threshold. The red and blue curves represent MEG in QDs alone and MEG in QDs when a surface plasmon resonance is present, respectively.

Figure 31 illustrates the potential effect of SPRs on the generation of electron hole (e^-h^+) pairs after MEG. It is based on two assumptions: (i) every photon absorbed above the MEG wavelength threshold can yield a maximum of two e^-h^+ pairs, and (ii) coupling to the SPR doubles the photo-absorption rate for those photons. In this model, if just 20% of the photons are above the MEG threshold, surface plasmon induced absorption in the QD could theoretically increase the efficiency by 11%.

In summary, my aim is to learn the factors that control the coupling between QD excitons and SPRs in Ag NPs. What, for example, is the dependence on distance between QD and NP? How

does the excited state (exciton, biexciton, trion, etc) on the QD affect the coupling strength? What is the effect of nearby SPRs on the absorption rates? Ultimately, I hope to demonstrate spectroscopically that I can enhance the excitation rates in metal-coupled QD systems relative to QDs alone. We took two, vastly different approaches toward systems to answer these questions with similar spectroscopic experiments.

2.1.2 Two Approaches

We can study the (many possible) effects of the SPR near lead-based QDs and the distance dependence of these effects using our two approaches: **1)** all-in-one hybrid NPs Au/CdX/PbX where X = Se and S and **2)** Films of Ag NPs with PSS and PAA polymer spacer layers and core/shell QDs on top. Each approach is illustrated in Figure 32.

With both approaches (Figure 32), we propose using noble metal NPs as the SPR source (red sphere) and PbX (X=S or Se) as our near IR, multiple exciton-generating semiconductors (teal sphere). In our colloidal approach, within the core/shell/shell hybrid nanoparticles, the CdX spacer (purple sphere) between the Au and the PbX shell will act as a barrier for electron transfer back into the metal. This spacer can be changed synthetically and will allow us to control the distance between the SPR and the PbX layer.

In a similar way, the PAA and PSS charged polymer layers (blue and black squiggly lines) in our second, layered approach will act as a barrier for electron transfer back into the metal. Just by changing the amount of charged polymer layers spin coated onto our samples we can control the distance between the Ag NP and the core/shell QDs.

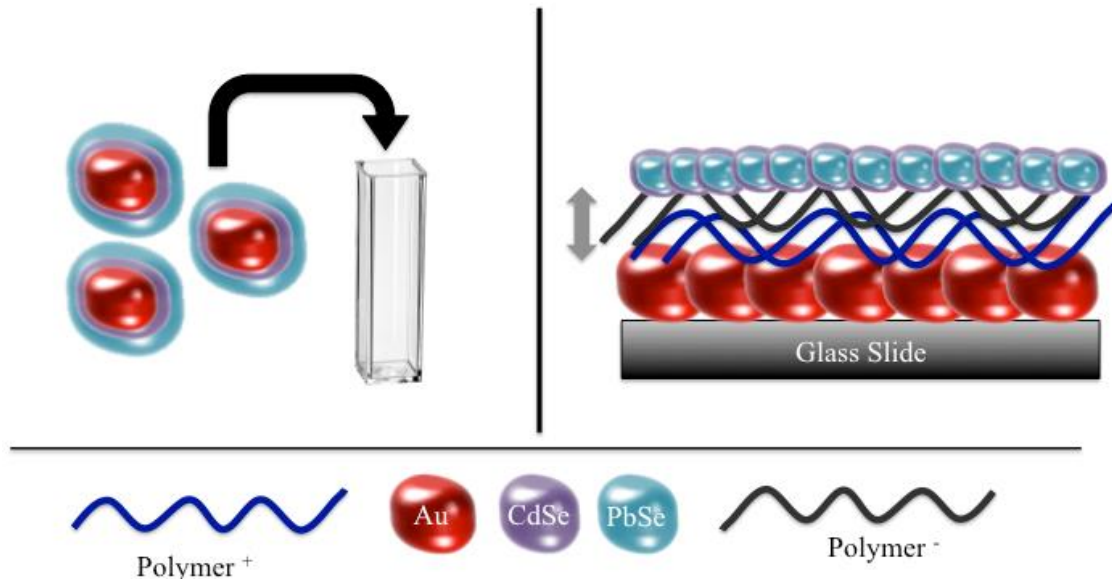


Figure 32: The two approaches to employ surface plasmon resonances to boost effectiveness of MEG in lead-based quantum dots: one colloidal and one layered. The left portion of the figure represents the colloidal, hybrid core/shell/shell approach. There is a metal core (red) with a wide bandgap shell (purple) and a near IR outer shell (blue). The right portion represents the layered approach where a monolayer of silver nanoparticles is separated from PbSe QDs by charged polymer spacer layers of varying thicknesses.

In the subsequent sections, each project will be described. The first project that will be discussed is the all-in-one hybrid NPs.

CHAPTER 2.2 PROJECT I: HYBRID CORE/SHELL/SHELL NPS

Our first approach was partially inspired by the Au/CdS core/shell nanoparticles that a former member of our group Andrew Tobias, Ph. D. studied and the general cation exchange process to create PbSe/CdSe core/shell QDs. An illustration with our rationale and NP design is displayed below in Figure 33.

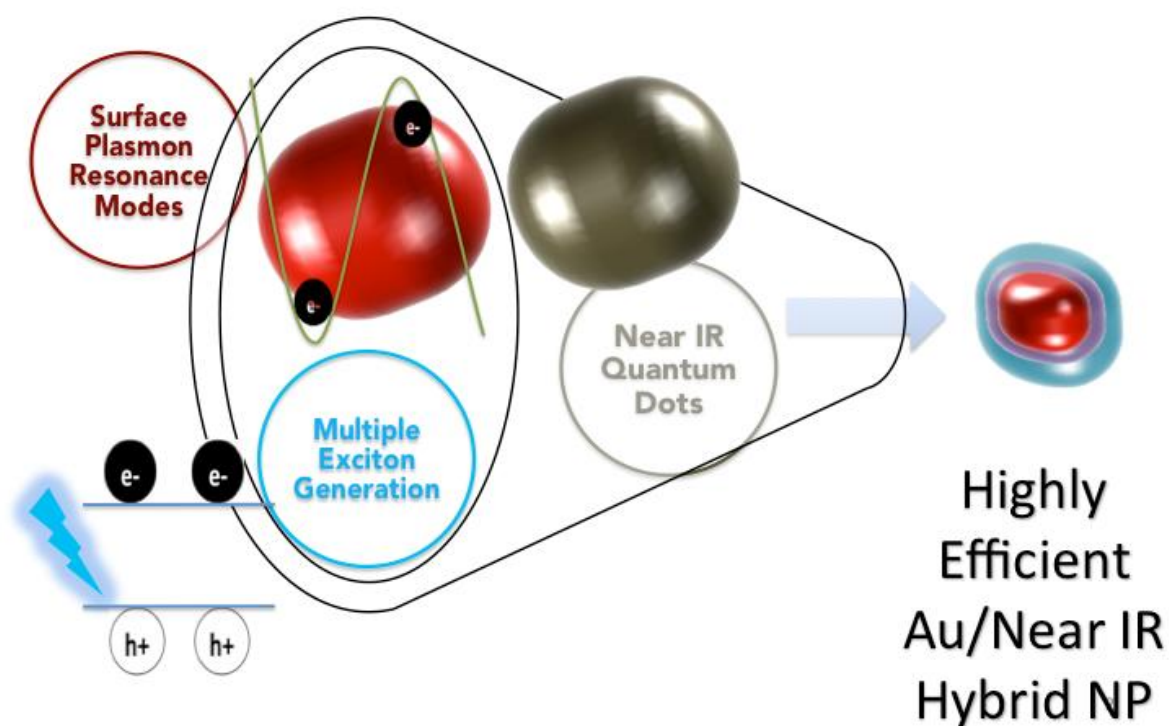


Figure 33: Schematic of rationale of our hybrid Au/CdX/PbX ($X = S$ or Se) NPs. The hybrid NP includes Au (red circle), a CdX layer (purple), and a PbX layer (teal). The idea is to use the MEG and near IR absorption capabilities of the PbX layer along with the surface plasmon resonance modes of the metal nanoparticle. The idea is to boost the absorption and possibly MEG of the PbX layer with the SPR of the metal. The wide bandgap spacer (purple = CdX) was placed to minimize energy loss into the metal.

We aimed to use the SPR of Au to act as an antenna to push more light above the MEG threshold in the near IR absorbing PbX layer. This will create a highly efficient,

well absorbing hybrid nanoparticle for PV purposes. Important aspects to keep in mind with this approach is shown in Figure 34 with the Au NP SPR shown as the red sphere and the near IR, PbX layer as the grey sphere.

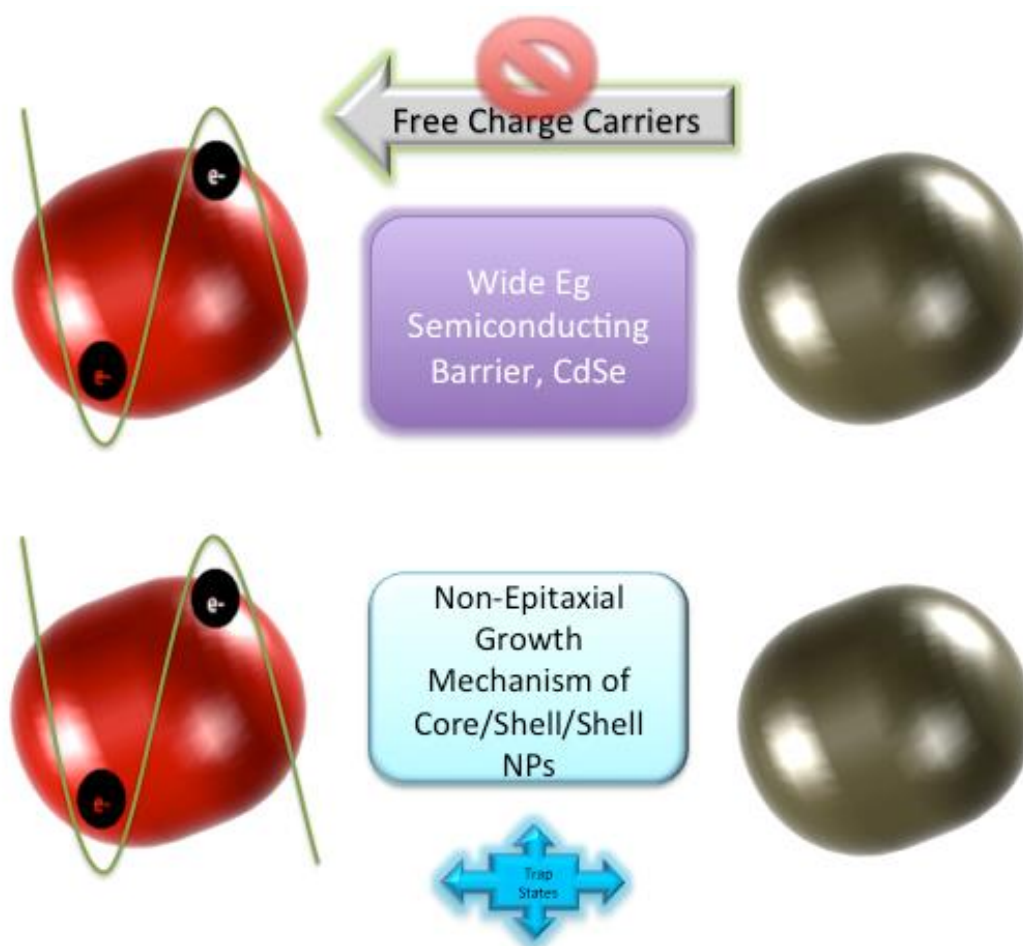


Figure 34: Vital aspects to ensure that this approach worked. The wide bandgap spacer (purple = CdX) was placed to minimize energy loss into the metal. We chose a non-epitaxial growth mechanism of the core/shell/shell NPs to minimize the defects that act as trap states.

To avoid free charge carriers flowing back into the metal through the Schottky barrier, we propose the inclusion of a wide E_g semiconductor layer such as CdSe separating the SPR and NIR QD.

We chose an epitaxial, and cation-exchange growth mechanism of the two shells surrounding the Au to help minimize interfacial defects that act as trap states and lower the efficiency of the NP. The outer shell was formed via cation exchange between the lead and cadmium. We synthetically controlled the distance between the Au and the PbX layer by tailoring the cation exchange process. The work that has already been accomplished in this approach will be mentioned next.

2.2.1 Synthesis and Characterization of Core/Shell/Shell Hybrid NPs

Each step of the synthetic process is broken down with italicized headings with a corresponding figure. A cation-exchange synthesis method was chosen to minimize defects that act as trap states for generated charges.¹⁶⁶ This particular method was altered and optimized by Andrew Tobias in a peer-reviewed scientific video journal, JOVE.¹⁶⁷ The first step was to make the Au cores.



Step 1: Au NP synthesis (≈ 15 nm diameter)

The Au cores were synthesized by first heating equal amounts of 1 mM HAuCl₄ and 0.2 M CTAC to 70 °C in an oil bath. Once temperature was reached borane tertbutylamine was added to reduce the Au to begin forming nanoparticles. Upon adding the reducing agent, the solution turns into a wine-red color which is indicative of NP formation. The reaction was heated for 30 minutes to create 15 nm Au NPs. A transmission electron micrograph of the aforementioned, CTAC-coated, Au NPs is shown in Figure 35.

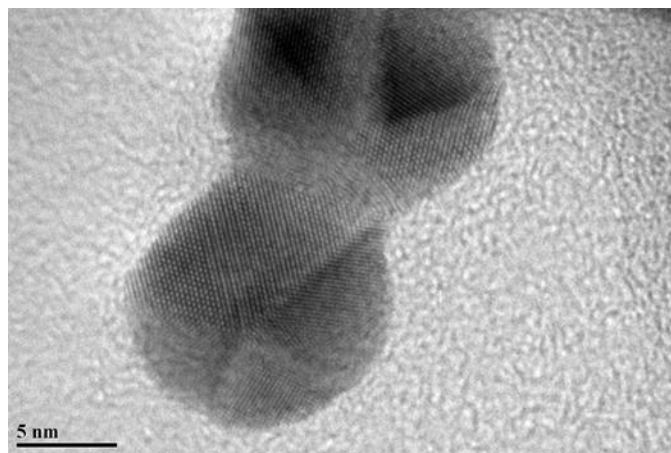


Figure 35: TEM image of cetyltrimethylammonium chloride coated gold nanoparticles. The scale bar is 5 nm and the image is of two NPs stuck together. The atomic lattice and the facets of the Au NPs are clearly visible.

In Figure 35, the facets of the two Au NPs (approximately 15 nm in diameter) are clearly visible. As seen in the TEM, the lattice fringes of the crystalline Au NPs are visible. The particles are not exactly spherical, with clear rectangular (100) and triangular (111) facets. In the next step, a silver shell was grown on these facets of the Au NPs.



Step 2: Ag shell growth (5-25 nm thick)

The Ag shell can be grown on the Au NPs anywhere from 5 nm to 25 nm in thickness, which determines the thickness of the overall shell. To make a 15 nm Ag shell, 130 mg of ascorbic acid, 10 mL of Au NPs, and 1.76 mL of 8 mM silver nitrate were heated to 70 °C in an oil bath for 2 hours. Changes to the ascorbic acid and silver nitrate amounts were made depending on the desired Ag shell thickness. Figure 36 includes the absorbance spectra as this reaction proceeded for a 20 nm Ag shell.

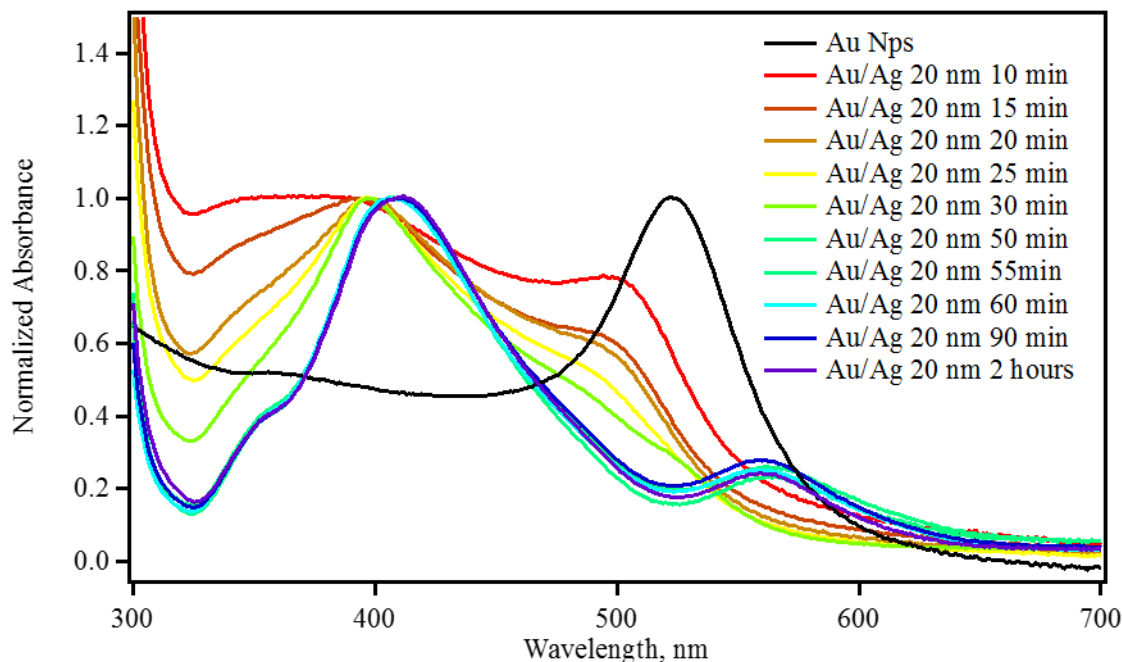
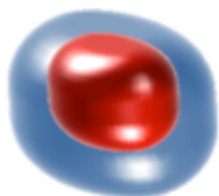


Figure 36: Absorption versus wavelength of gold nanoparticles as growth of a 20 nm thick silver shell proceeds (red to purple). The black curve represents the absorbance of gold nanoparticles before the reaction occurs. As the Ag shell growth proceeds (red to purple) in time, the spectrum shifts and begins to look like the characteristic silver NP plasmon alone.

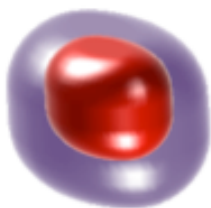
As the Ag shell grew, the Au plasmon peak around 520 nm remains but shifts slightly due to the change in the dielectric constant of the surrounding media. The peak that arises around 570 nm may be due to a higher order mode of the large silver shell. The Ag plasmon peak at about 400 nm appears and narrows as the monodispersity of the shells increase. At first, the solution visually appears as a wine-red solution. As the reaction proceeded, it progressively turned a bright orange color.

The final Au/Ag NPs were washed with ethanol and redispersed in >3 mL of DI water (the high concentration causes solution to appear burnt orange). They were dispersed in a small amount of water for the phase transfer, which occurs in the next step.



Step 3: Dope the Ag shell with either selenium or sulfur

In this step, the Ag shell outside of the Au was doped with sulfur or selenium. To dope a 15 nm Ag shell with sulfur, 52 mg of elemental sulfur was first dissolved in 7 mL oleylamine, 3 mL oleic acid, and 10 mL toluene. Once the sulfur was completely dissolved, forming a bright yellow solution, the Au/Ag NPs dispersed in a small amount of DI water were injected and allowed to stir for 1 hour at room temperature. At this point in the procedure, the suspension of nanoparticles appeared bright green. The suspended Au/Ag₂S NPs were washed with ethanol and redispersed in toluene. The resulting washed NPs were a deep teal-blue color. In the next step, there was a complete cation exchange between the Ag⁺ and Cd²⁺.



Step 4: Cation exchange of Ag⁺ with Cd²⁺ with tributylphosphine (TBP) as a transport agent

To initiate this cation exchange for a 15 nm shelled Au/AgX (X = S or Se) sample, the particles were added to 0.35 mL of 8 mM cadmium nitrate and heated to 50 °C under nitrogen. After 10 minutes, the transporting agent, tributylphosphine was added and the reaction was allowed to stir for 2 hours under the same conditions. The newly

formed Au/CdX NPs were washed with ethanol, redispersed in toluene, and had a royal blue appearance. Figure 37 A) and B) shows a TEM and EDX elemental analysis of Au/CdSe NPs, respectively.

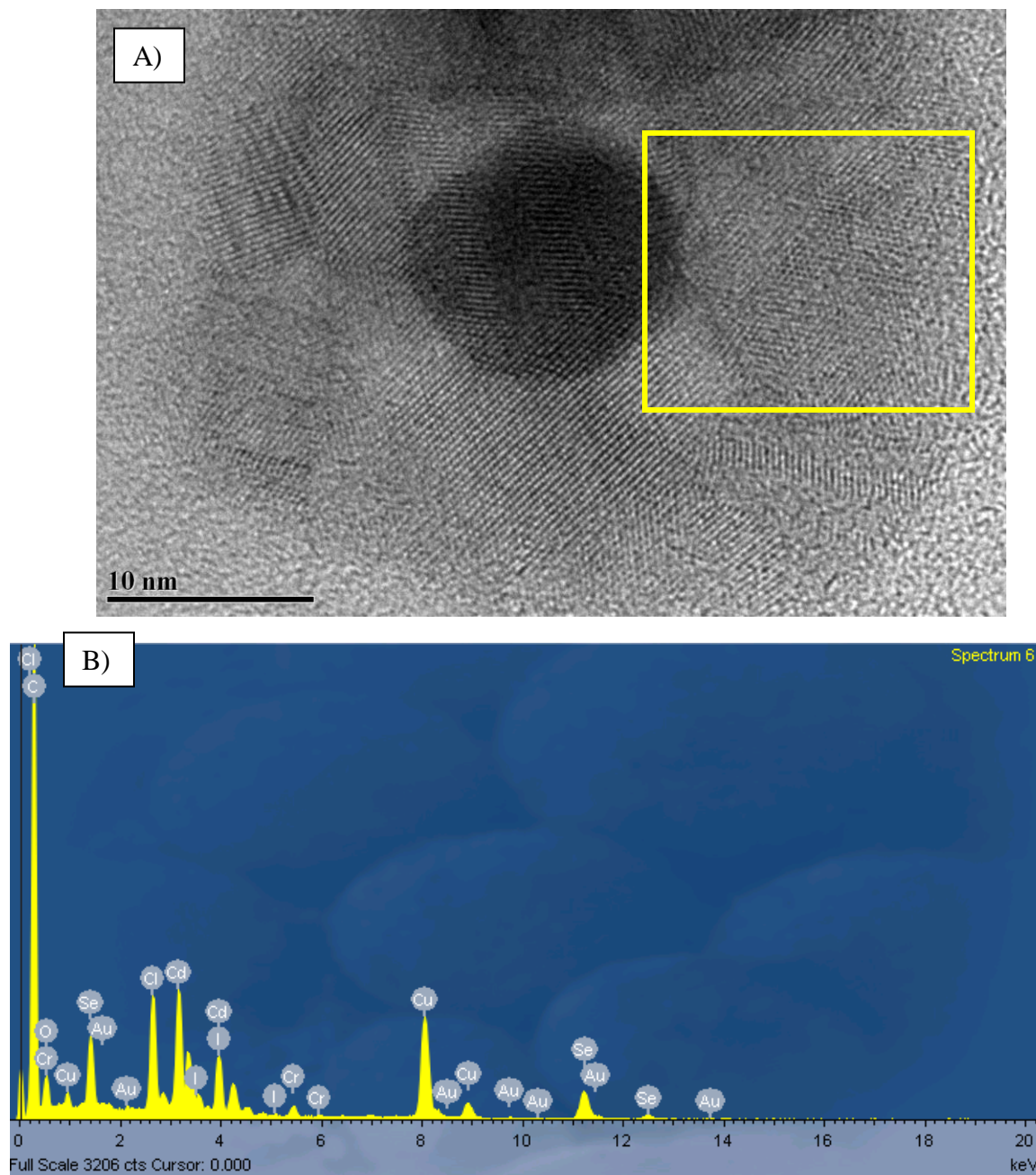


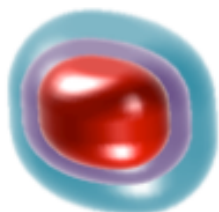
Figure 37: A) TEM and B) EDX elemental analysis of a single Au/CdSe hybrid nanoparticle. In the TEM image, the scale bar is 10 nm and the yellow rectangle represents the area which the

energy dispersive x-ray (EDX) elemental analysis was taken on. The copper, silicon, chromium, carbon, oxygen and chlorine signals arise from the sample grid and detector.

Figure 37 A) shows that the hybrid particle has a clear core and shell. The CdSe shell appears to be crystalline and approximately 15 nm in radius. The Au core appears to be approximately 10 nm in diameter. The high electron density in the Au NP causes the core of the nanoparticle to appear darker in the TEM because less electrons can transmit through. The clear grain boundaries revealed in the lattice fringes of the shell may be indicative of strain caused by the synthetic process. The yellow rectangle in Figure 37 A) represents the portion of the nanoparticle used for the analysis in Figure 37 B).

Figure 37 B) shows the energy-dispersive x ray spectroscopy (EDX) elemental analysis. To take this measurement, a high energy beam of electrons is bombarded on a selected portion of the sample (Figure 37 A), yellow rectangle). For this measurement, I selected a large portion of the NP shell. After the sample is bombarded, X-rays are emitted from the sample which are elementally unique, allowing us to determine the types of elements within the sample. This measurement was taken to ensure that the cation exchange between the Ag and Cd was completed. There is no Ag peak in 37 B, which proved to me that no Ag is left in the shell from *Step 4* and that the cation exchange was successful. It should be noted that copper and carbon peaks arise from the TEM sample grid and the carbon lacy mesh, respectively. The chromium peak is from the detector.

The very last step is a novel, partial cation exchange between Pb^{2+} and Cd^{2+} to yield a PbX outer shell. This step completes the core/shell/shell hybrid NP.



Step 5: Partial cation exchange between Pb^{2+} and Cd^{2+} for PbX shell

The Au/CdX NPs was be exposed to a lead solution to initiate a Cd^{2+} cation exchange reaction with Pb^{2+} , forming a PbX shell on the outermost surface. The shell's purpose is to stop electron transfer between the PbSe and Au layer and enable distance control between the plasmonic and semiconductor layer.

The cation exchange between lead and cadmium on CdSe surfaces has been published with the use of lead oleate and lead chloride.¹⁶⁸ The first attempt was inspired by PbSe/CdSe synthesis where PbSe QDs are exposed to a cadmium oleate solution at 100 °C to initiate the cation exchange (but reversed).¹⁶⁹

Lead Oleate Method for PbX Layer

Figure 38 shows the normalized absorbance spectra of Au/CdS samples as the cation exchange reaction using lead oleate occurred at 100 °C. Three different samples were analyzed: before the Au/CdS were exposed to lead (Figure 38, black curve), after the samples were exposed to lead oleate for 4 hours (Figure 38, red curve), and after the sample was exposed for 15 hours (Figure 38, blue curve.)

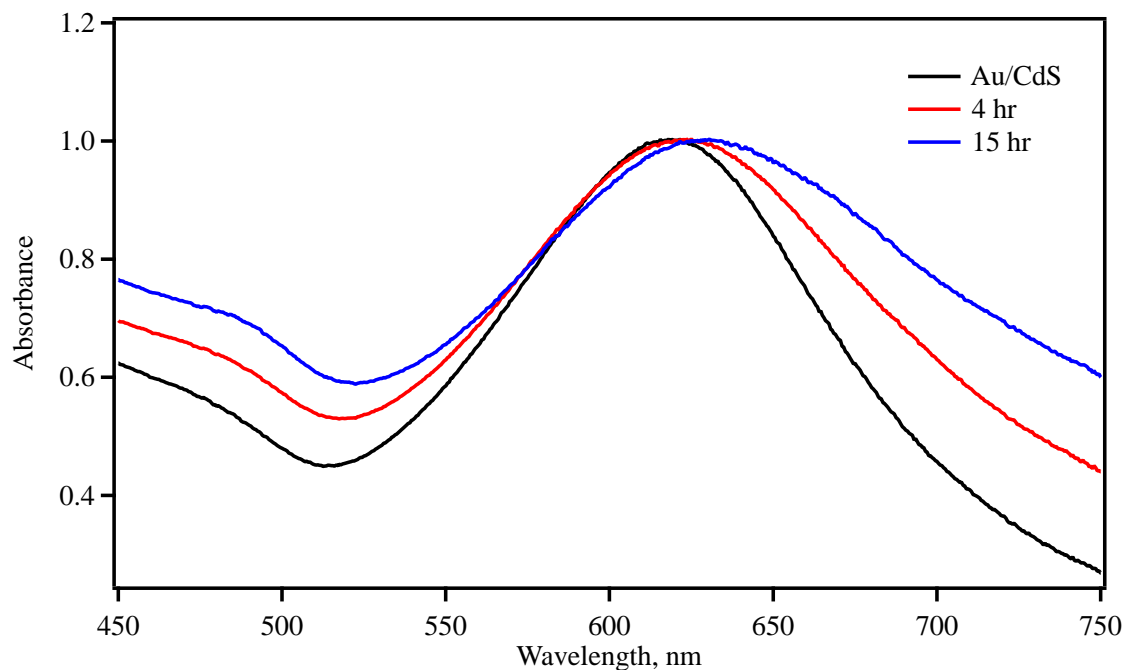
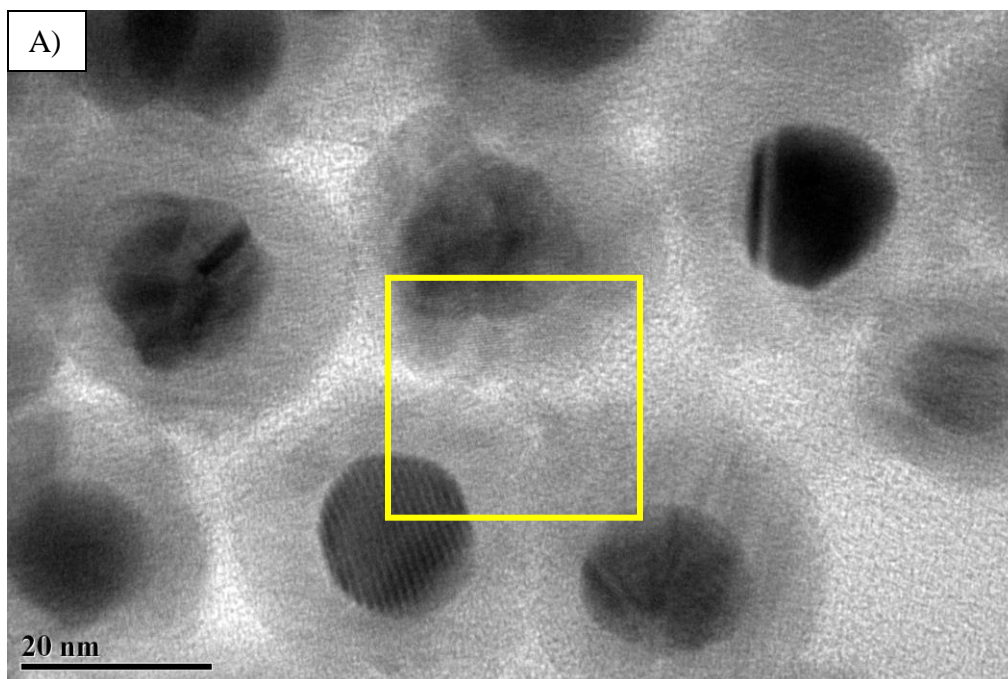


Figure 38: Absorbance changes versus wavelength of Au/CdS hybrid nanoparticles during “cation exchange” using exposure to lead oleate. The absorbance of the initial Au/CdS nanoparticles is shown in black. The blue and red curves show the absorbance as the cation exchange reaction proceeds for 4 and 15 hours, respectively.

After four hours of the reaction (red curve), there is a broadening and slight red shift of the Au plasmon peak compared to the Au/CdS (black curve). I allowed the reaction to proceed for 15 hours (blue curve), and a slight red shift and broadening occurred-but overall not much had changed. There were no peaks present in the near infrared (up to 1700 nm).

Unconvinced that Pb had incorporated into the CdS shell, TEM and EDX analyses were performed on the washed “15 hour” sample (Figure 39 A) and B)). I did not expect to visually see the outer, PbS shell in the TEM image (Figure 39 A)) because the d-spacing of CdS is not significantly different than that of PbS. However, since there should not be any starting material in the NP suspension because they were washed, the presence of lead and cadmium in the EDX analysis would prove that the partial cation

exchange was successful. In fact, the ratio between the Pb and Cd signals could give me a clue to how far the cation exchange had gone. With a 15 hour reaction time with lead, I intended on this reaction causing a complete cation exchange between lead and cadmium. I presented the EDX data in a table (Figure 39 B)) to quantify and compare the relative atomic amounts of lead and cadmium.



B)

Element	Peak	Area	k	Abs	Weight%	Weight%	Atomic%
	Area	Sigma	factor	Corn.		Sigma	
C K	987	74	2.208	1.000	4.90	0.36	23.11
O K	159	34	1.810	1.000	0.65	0.14	2.29
S K	502	78	0.940	1.000	1.06	0.16	1.87
Cl K	309	52	0.964	1.000	0.67	0.11	1.07
Cr K	663	61	1.100	1.000	1.64	0.15	1.79
Cu K	22463	250	1.366	1.000	69.04	0.75	61.51
Cd L	2471	132	1.769	1.000	9.84	0.49	4.96
Au L	927	90	2.622	1.000	5.47	0.51	1.57
Pb L	1076	85	2.775	1.000	6.72	0.50	1.84
Totals					100.00		

Figure 39: A) TEM and B) EDX elemental analysis of Au/CdS/PbS after 15 hr exposure to Pb oleate. In the TEM image, the scale bar is 20 nm and the yellow rectangle represents the area which the energy dispersive x-ray (EDX) elemental analysis was taken on. The copper, silicon, chromium, carbon, oxygen and chlorine signals arise from the sample grid and detector. The atomic % of lead and cadmium present in the yellow area were 1.84 and 4.96 %, respectively.

The TEM image showed that the shell was intact; neither confirming nor denying the presence of an PbS outer shell. Surprisingly, the elemental analysis (Figure 39 B)) showed Pb present in the sample with atomic % of 1.84 and Cd present 4.96 %. Due to the very low presence of PbS in the 15 hours of exposure, it was clear that a different approach to incorporate lead had to be taken. An overall smaller, possibly more favorable form of lead for the cation exchange is lead nitrate.

Lead Nitrate Method for PbX Layer

I decided to expose the Au/CdS NPs to lead nitrate (in methanol) at 150 °C with tributylphosphine, TBP added to aid in cation transport. Absorbance measurements were taken every 10 minutes for 3 hours. For clarity purposes, only the normalized absorbance spectra of the initial Au/CdS suspension (black), the reaction after 3 hours (red), and with a control (grey) are shown in Figure 40. For the control reaction, I added the same amount of methanol and TBP but without any lead. I allowed the control reaction to heat to 150 °C for three hours. I used the control to be sure that the spectral changes were not occurring because of heating induced degradation etc..

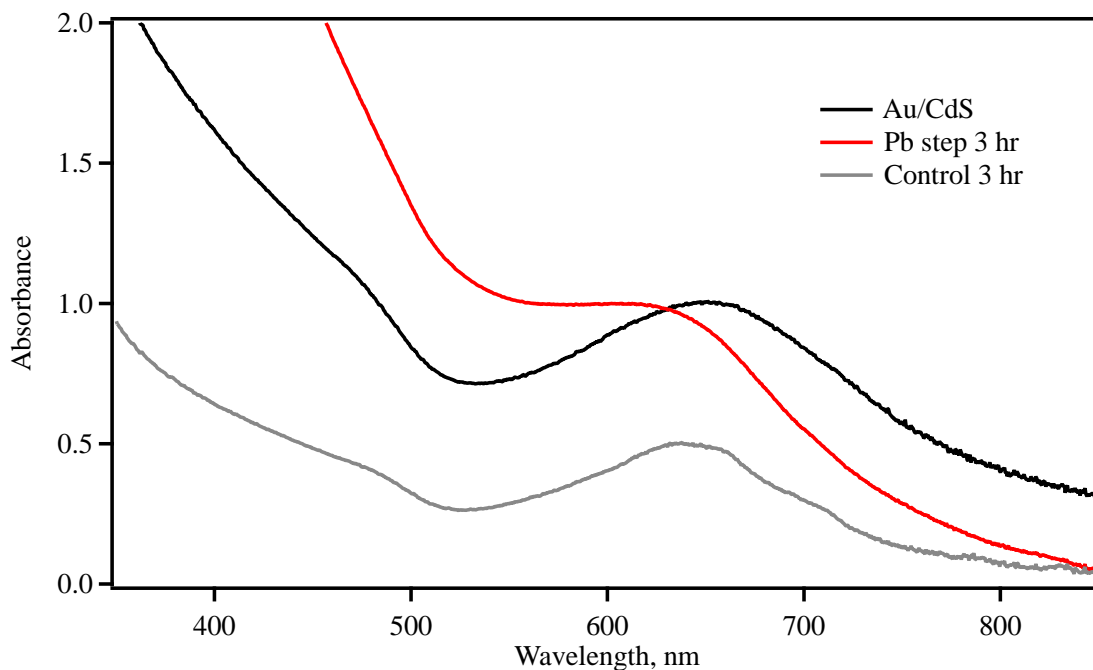


Figure 40: Absorbance changes versus wavelength of Au/CdS hybrid nanoparticles during “cation exchange” using exposure to lead nitrate with tributylphosphine as a transport agent. The absorbance of the initial Au/CdS nanoparticles is shown in black. The red curve shows the absorbance as the cation exchange reaction proceeded for 3 hours. The grey curve shows the absorbance of the control sample (at $\frac{3}{4}$ the intensity for clarity). The control sample was exposed to everything that the (red curve) was (including heat and solvents) except lead nitrate.

In Figure 40, comparing the black and red curves, the Au plasmon peak changes shape (to more of a shoulder) and blue-shifts after three hours of exposure to lead nitrate. Comparing the original reaction (black curve) to the control (grey curve), the plasmon peak did not change in location. The intensity of the control curve (grey) was intentionally lowered for clarity purposes. Per Mie theory, we would expect the Au plasmon peak to (if anything) move in the opposite direction with the change in dielectric constant of the media from CdS to PbS.

Though TEM and EDX were needed to confirm the presence of lead in the shell, the lead nitrate method seems much more promising for the generation of a PbX shell than the lead oleate method. Although I was successful at fabricating the core/shell/shell

hybrid nanoparticles, the PbX layer did not emit as expected, no matter how hard I tried. I did some research in the literature on this issue and found the others were experiencing this problem with complex layered nanosystems, too. The main culprit is lattice strain.

2.2.2 Effects of Lattice Strain on Photoluminescence of PbX (X= S, Se) Layer

Lattice strain can cause the quenching/suppression of fluorescent nanoparticles.¹⁷⁰ The lattice strain of the PbX outer layer combined with the close proximity to the ligands provides a favorable situation for surface trapping. Furthermore, the cation exchange diffusion between the CdSe and PbSe layers cause even more lattice strain through changing the radial composition.¹⁷¹ The strain is caused by the polycrystalline nature of the semiconductor shell layer and can be seen visually in the TEM image (Figure 41). I altered the brightness and contrast of the image to aid the viewer in visualizing the changes in lattice domains. The polycrystalline nature is caused by a phenomenon called Stranski-Krastanov (S-K) growth.

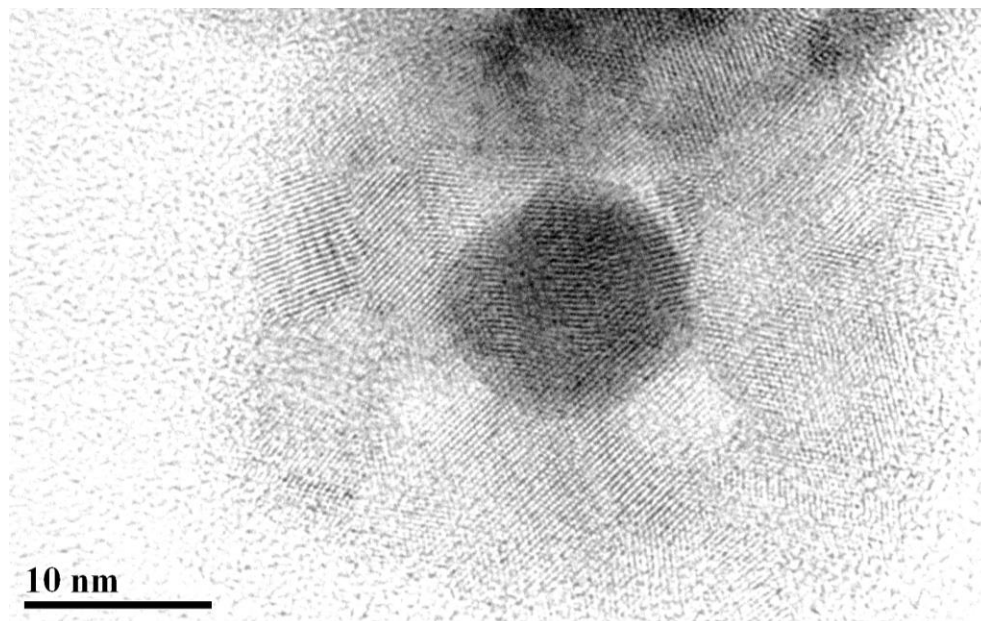


Figure 41: High contrast, close-up TEM images revealing polycrystalline shell of a single Au/CdSe core/shell NP. The scale bar is 10 nm. The light gray area represents the shell and the dark circle represents the Au core.

S-K growth is a common phenomenon in thin film preparation and has been observed in core/shell nanoparticles with high lattice mismatch.¹⁷² In nanoparticle S-K growth, once the shell reaches a critical thickness (which depends on the initial core thickness), nucleation of randomly oriented crystalline domains yields a polycrystalline shell.¹⁷¹ Unfortunately, the strain-suppressed emission of these hybrid nanoparticles led me to drop the project and focus on my second approach: Layered Thin Films.

CHAPTER 2.3 PROJECT II: LAYERED THIN FILMS

In our second approach, we aim to use a layered film system. As illustrated in Figure 42, the layers will include glass, Ag NPs, charged polymer layer spacers, and PbSe QDs. We chose silver due to its excellent scattering properties.

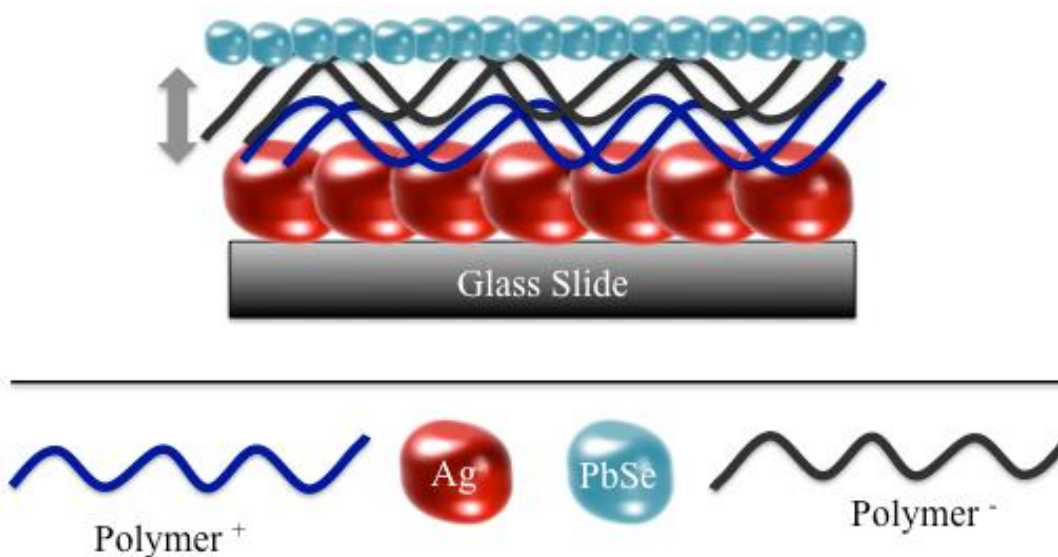


Figure 42: Configuration of layered system in the second approach. In this approach, a monolayer of silver nanoparticles (red spheres on glass slide) is separated from a PbSe QD monolayer (blue spheres) by charged polymer spacer layers (blue and black lines) of varying thicknesses.

The amount of charged polymer layers could be easily varied and will dictate the distance between the SPR and QD. We could also control the plasmon and QD optical properties. This provides a robust and versatile platform to study the optical effects of SPRs on QD absorption enhancement. The first step of this approach was to fabricate and optimize the Ag NP monolayer. Now, I will introduce silver nanoparticle films in terms of our application.

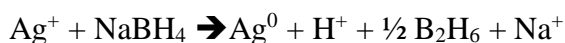
2.3.1 Introduction to Project II

In order to truly exploit metal enhanced absorption, we separated the extinction coefficient of metal nanoparticles into absorption and scattering, experimentally, with an integrating sphere. In this work, the scattering and absorption properties of highly loaded silver NP films were determined using an integrating sphere and compared to determine their MEF ability. We aimed to create a library of metal films that can be used for metal enhanced absorption or fluorescence at any wavelength.

2.3.2 Tuning Silver NP Synthesis

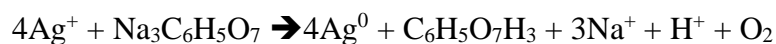
Various sizes of Ag NPs were synthesized by a “seeded” growth mechanism. The seeds are formed by the rapid reduction of silver ions (Ag^+) by sodium borohydride (NaBH_4). Then, the seeds grow larger following a slow reduction and passivation by sodium citrate ($\text{Na}_3\text{C}_6\text{H}_5\text{O}_7$). This is a one pot method. The sizes of resulting Ag NPs were controlled by tuning the ratio of $[\text{Ag}^+]/[\text{NaBH}_4]$. The respective reaction mechanisms are described below.

1) Reduction by Sodium Borohydride (FAST)



The reduction by sodium borohydride is very fast. There is a 1:1 ratio needed between Ag^+ and NaBH_4 for reduction to occur. Due to the speed of this reaction, it determines the number of NPs created and the amount of silver left over for the slower reduction by sodium citrate. Simultaneously with the NaBH_4 , the reduction by sodium citrate occurs at a much slower rate. It would be easiest to imagine that the reduction NaBH_4 happens first, and whatever silver is left over is reduced by the sodium citrate.

2) Reduction by Citrate (SLOW)



It takes only one molecule of sodium citrate to reduce 4 silver ions. The NP growth reaction proceeded until all the Ag^+ monomer was consumed. As previously mentioned, the size of the Ag NPs were controlled by the initial $\text{Ag}^+:\text{NaBH}_4$ ratio. The larger the ratio, the larger the resulting particles. This means that there is more leftover Ag^+ present to slowly be reduced to the surface of the seeds by the sodium citrate, yielding larger particles. It is also expected that the larger the ratio, the larger the degree of polydispersity. The very slow reduction by sodium citrate (even at high temperatures) would favor larger particle surfaces than smaller ones.¹⁷³ The more silver ions that the citrate is responsible to reduce then the larger the resulting particles and polydispersity.

Since the sodium citrate is also used to passivate the NP surface, I made sure that there was an excess amount present in all reactions. The passivated particle surface charges allow for repulsive van der Waals forces which improve nanoparticle stability. The precursor solutions were prepared as follows:

Precursor Solutions: First, a 0.5 M AgNO_3 solution was prepared by sonicating 0.849 g AgNO_3 in 10 mL deionized water for 10 minutes. Complete dissolution of the silver nitrate was crucial to the success and reproducibility of this reaction. Next, 0.5 M NaBH_4 was prepared by dissolving 0.190 g NaBH_4 in 10 mL DI water. Since lots of hydrogen gas is produced in the dissolution of NaBH_4 , it is important to vent the vial and be sure to knock out all the bubbles before measuring out and aliquot for the reaction.

Reaction Flask: Next, 0.400 g sodium citrate and 140 mL DI water was added to a 250 mL Erlenmeyer flask and heated until the temperature reached 85 °C. It was allowed to stir

vigorously for at least 5 minutes to ensure complete dissolution. For ≈ 20 nm diameter Ag NPs, (a 2:1 ratio was used) 3.5 mL of the Ag precursor was added to the flask until the solution became clear. For the first few seconds, the reaction flask becomes cloudy. After a few seconds, 1.75 mL NaBH_4 was added and the reaction immediately turned black. This is indicative of the rapid seed growth (on the millisecond range) caused by the reduction and coalescence of Ag^+ atoms.¹⁷³ After 20 minutes, the reaction was quenched by an ice water bath for a few minutes and then allowed to continue to cool to room temperature for the next ten minutes while vigorously stirring.

The citrate capped Ag NPs were used as-is for the film preparation or washed once with ethanol for TEM measurements. Figure 43 shows a TEM image of Ag NPs fabricated with a 3:1 Ag: NaBH_4 ratio.

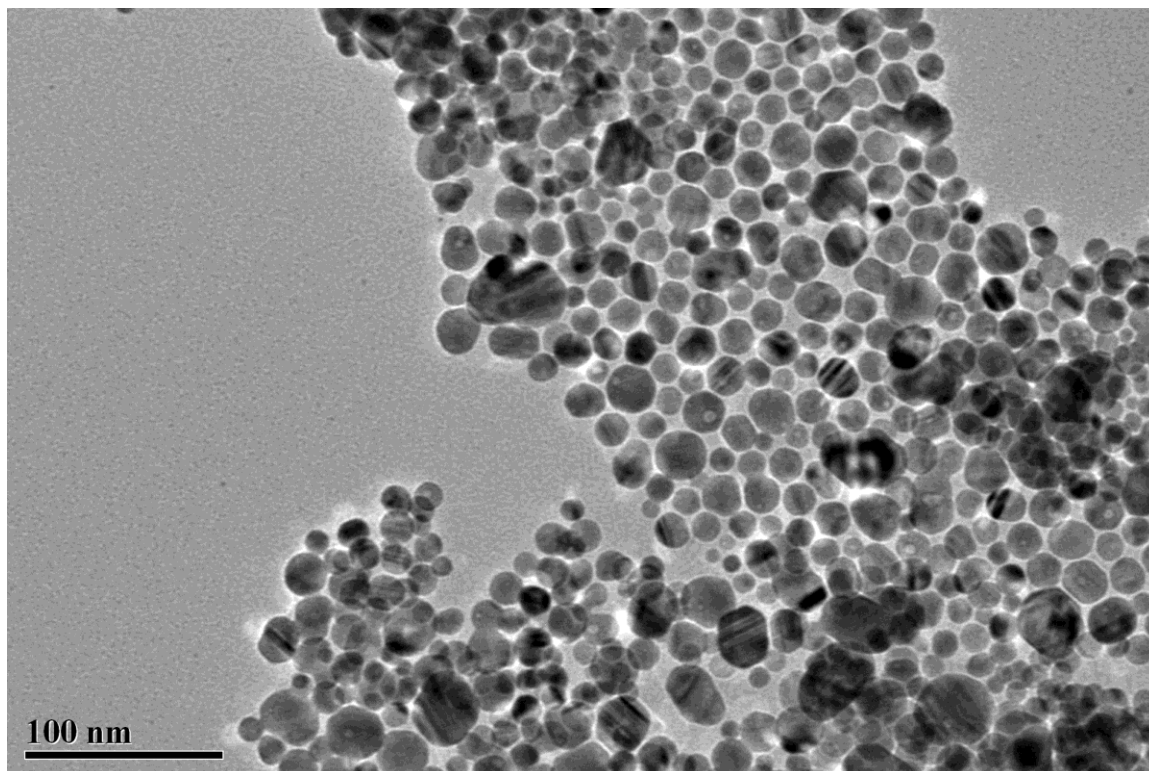


Figure 43: TEM image of silver nanoparticles fabricated with a 3:1 Ag:NaBH₄ ratio. The scale bar is 100 nm.

The Ag NPs appear spherical and polydispersed. I was able to correlate the synthetic ratio and the average size determined by the TEM measurements. The relationship between the Ag:NaBH₄ ratio and the diameter determined by TEM was investigated (Figure 44). As expected, the as the ratio increased, the average NP size did too. With larger ratios, there was more Ag⁺ around after the initial, fast NaBH₄ reduction to be reduced onto the surfaces of the NPs by the surrounding citrate, yielding larger particles.

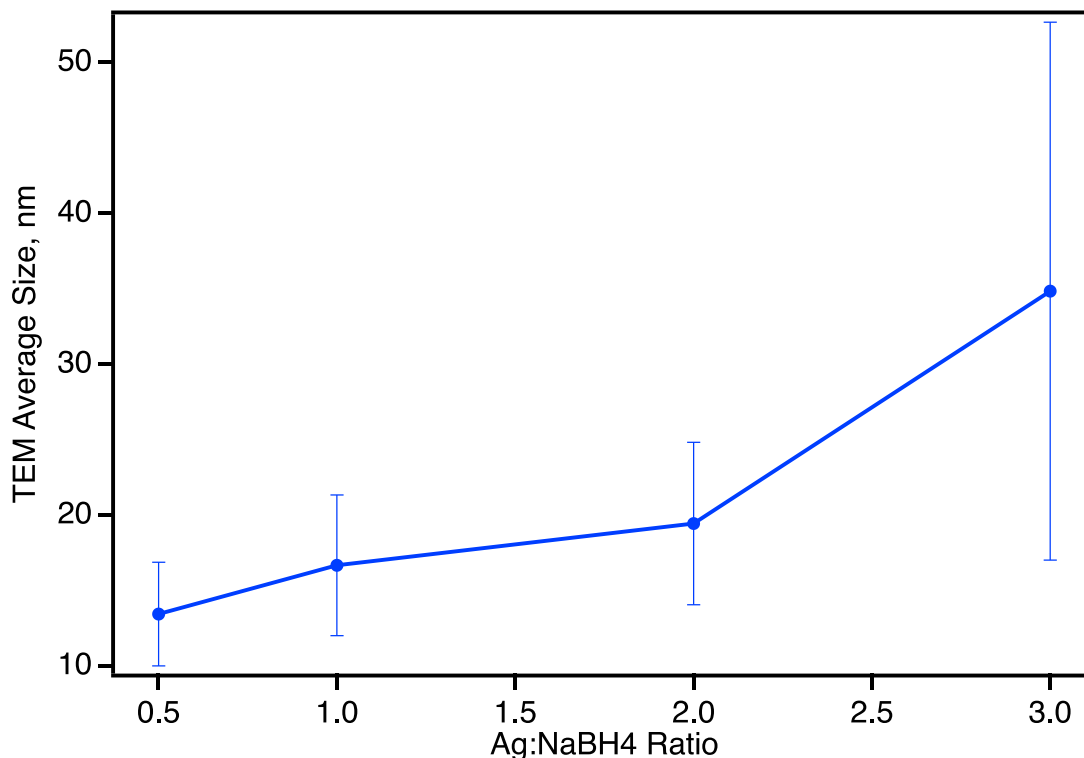


Figure 44: Average silver nanoparticle size determined by TEM versus the Ag:NaBH₄ ratio used in the synthesis. As the ratio increases, the average TEM size increased too. For each ratio, there were at least 60 nanoparticles diameters measured (error bars).

Figure 44 shows the relationship between average TEM size, nm and Ag:NaBH₄ ratio. The figure shows that not only does the size increase with the ratio, but the standard deviation of the sizes does too. This trend can be explained by the slow citrate reduction favoring larger particles and Ostwald ripening. We also looked at the absorbance changes of the colloidal suspension of Ag NPs with increasing NaBH₄ (Figure 45).

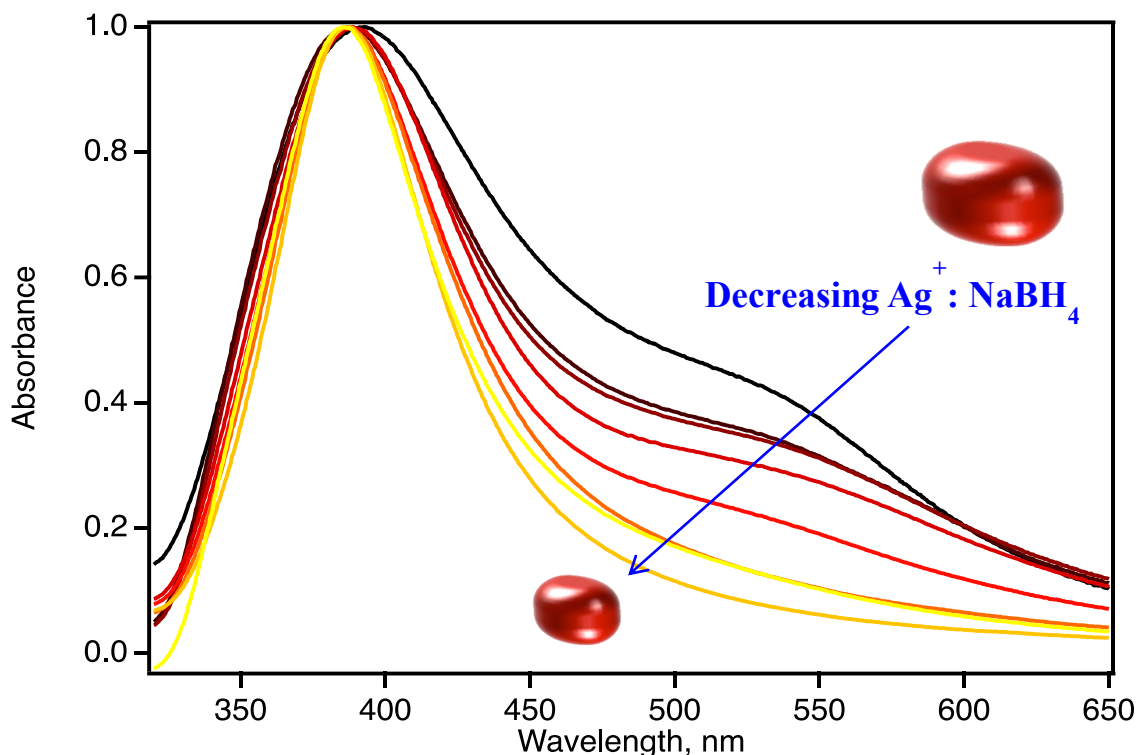


Figure 45: Colloidal Ag NPs normalized absorbance changes versus wavelength, nm with changing Ag:NaBH₄ ratio. The blue arrow represents the absorbance trend as this ratio increases. The red spheres show the relative nanoparticle size as this ratio changes. The decrease in absorbance shoulder as the particles get smaller corresponds to the decrease in higher order plasmon modes.

The figure above shows the Ag NP absorbance (in a cuvette) at different wavelengths. The scans from black to yellow show the changes in absorbance as the relative amount of NaBH₄ increases. The spectroscopic trend supports what was observed in the TEM study; more NaBH₄ yields smaller, more monodispersed particles. The red shoulder appearing as lesser amounts of NaBH₄ (greater Ag:NaBH₄) ratios suggests that higher order modes are appearing due to an increase in size.

These TEM and in-suspension, spectroscopic experiments proved that we can control and tune the Ag NP properties by changing the Ag⁺:NaBH₄ ratio during synthesis.

The next step was to apply these Ag NPs in a monolayer onto glass slides as the first layer of our system.

2.3.3 Applying and Characterizing Ag NP Monolayer Films

It is vital that the glass substrate is clean from any organic materials or dust before they are treated with silane and later Ag NPs. First, glass slides were cut and cleaned using a piranha bath (3:1 volumetric ratio of sulfuric acid to peroxide) at 85 °C for one hour. The films were rinsed with milli-q water and then soaked in a basic solution (10 mL 30 % ammonium hydroxide, 50 mL milli-q water, and 10 mL 30 % peroxide) for an hour. The clean films were rinsed 5-6 times with milli-q water and stored in methanol until the next step.

Next the surfaces of the films were exposed to a 2 % silane solution in methanol for 24 hours. This step functionalized the surface of the film so that the metal NPs would form a monolayer. Once the silane-covered films were sonicated in water, they were soaked in the citrate-stabilized Ag NP solution for 24 hours.

Once the Ag NPs were applied, the films were sonicated in water to remove unbound NPs. To prepare the slides for polymer application and spectroscopic experiments, one side of the film was wiped cleaned using a methanol-soaked q-tip. Before I started focusing on Ag NPs due to their excellent light scattering abilities, I made many gold NP monolayer films. Figure 46 shows a desktop scanning electron microscope (SEM) image of a gold NP film with 2 polymer layers added.

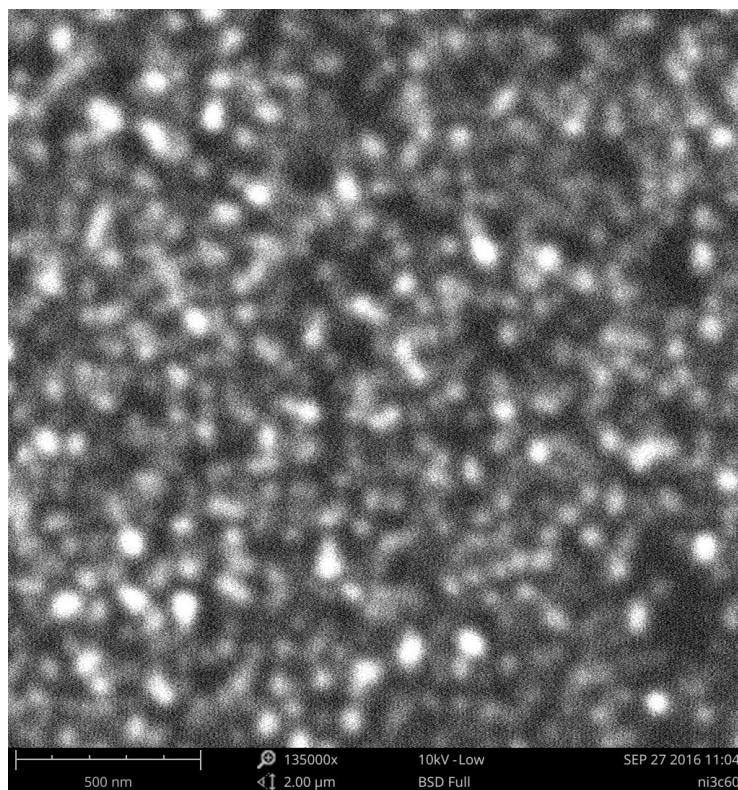


Figure 46: Scanning electron microscope image of a Au NP covered glass slides with PAA and PSS polymer layers. The scale bar is 500 nm.

For this measurement, a focused beam of electrons was scanned in a raster pattern across the surface of the film. The angle and energy that the electrons bounce back from the surface will give detailed, topographical information of the film. Here, the scale bar is 500 nm. Though it appears that the gold NPs range from 50 to 100 nm in diameter, the 2 polymer layers on top add to the perceived size. A more accurate depiction of the monolayer film morphology and size would be SEM or atomic force microscope measurements on a NP film without polymer added.

2.3.3.1 Photoaging of Silver Nanoparticles

Once the films were successfully fabricated, spectroscopic studies were swiftly taken. Silver nanoparticles are highly prone to surface oxidation in air. As Ag NPs are exposed to air and light, a silver oxide layer is formed on the surface. Studies on the photoaging of Ag NPs showed that the main culprit is oxygen as the electron acceptor.¹⁷⁴ Figure 47 a-b shows a study by Manchon et. al. on the role oxygen plays in the oxidation of single Ag NPs.¹⁷⁴

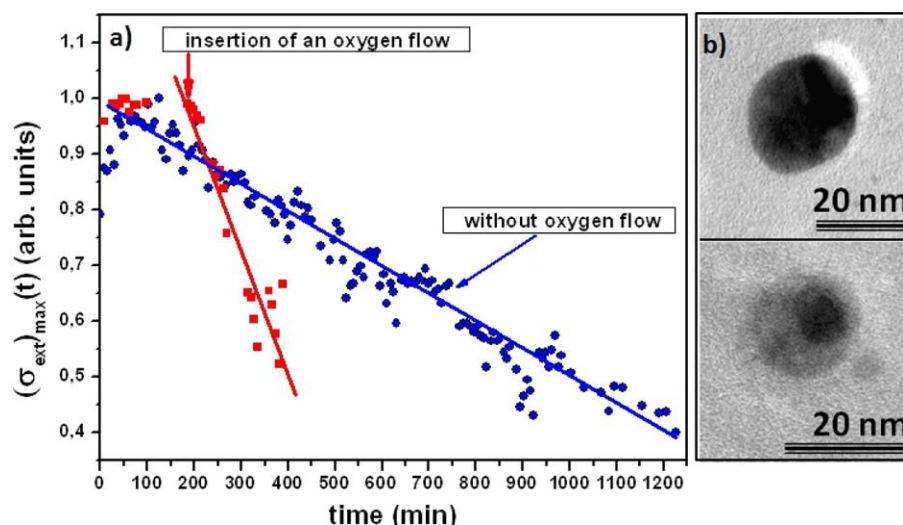


Figure 47: Evolution of a photoaging Ag NP. a) Represents the decrease in the SPR extinction maximum as the NPs photooxidize in the presence (red) and absence (blue) of oxygen over time. b) Represents the TEM image of the (top) non-oxidized and (bottom) oxidized surface.¹⁷⁴ Reprinted (adapted) with permission from (Grillet, N.; Manchon, D.; Cottancin, E.; Bertorelle, F.; Bonnet, C.; Broyer, M.; Lerme, J.; Pellarin, M., Photo-Oxidation of Individual Silver Nanoparticles: A Real-Time Tracking of Optical and Morphological Changes. *Journal of Physical Chemistry C* 2013, 117 (5), 2274-2282.). Copyright (2013) American Chemical Society.

The photoaging of QDs manifests itself in the depletion of the SPR extinction maximum and the lightening of the surface in the TEM image. In this process, the water in the air adsorb onto the NP surface, then silver ions are dissolved and transferred to the adsorbed water leaving an oxide layer behind. The loss of Ag on the surface causes the

SPR to become weaker. Figure 47 a) shows that the photooxidation of Ag NPs in the presence of oxygen (red) is much more rapid than without (blue). For approximately half of the extinction intensity to be lost, it took approximately 400 and 900 seconds in the presence and absence of oxygen, respectively. In addition, Figure 47 b) shows that silver NPs in the presence of oxygen (bottom) have a distinctly different appearance under an electron microscope than Ag NPs. The oxidized layer has less electron density, and thus transmits more electrons through the material. This gives rise to the lighter appearance of the oxidized regions in the TEM.

For our research, the strength of the SPR extinction was vital to the absorption enhancement in the QDs. Since there was plenty of oxygen and water in the ambient air, the film samples were always kept in a pumped-down desiccator and wrapped in aluminum foil; except during the spectroscopic experiments.

2.3.3.2 Scattering and Absorbance of Silver NP Films

The scattering and absorption of the Ag NP films play an important role in the absorption enhancement rates of the QDs. Conventional spectrophotometers measure the sample extinction, not merely the absorbance. Energies where the NP films scatter the most relative to absorbance are expected to cause the most absorption enhancement in the QDs. I wanted to tune these ranges so that the scattering proportion was large at energies above the MEG threshold of the QDs. First, I took absorption and scattering measurements of the films using an integrating sphere set-up. To separate the Ag film extinction into absorbance and scattering, I used the integrating sphere set up shown in

Figure 48.

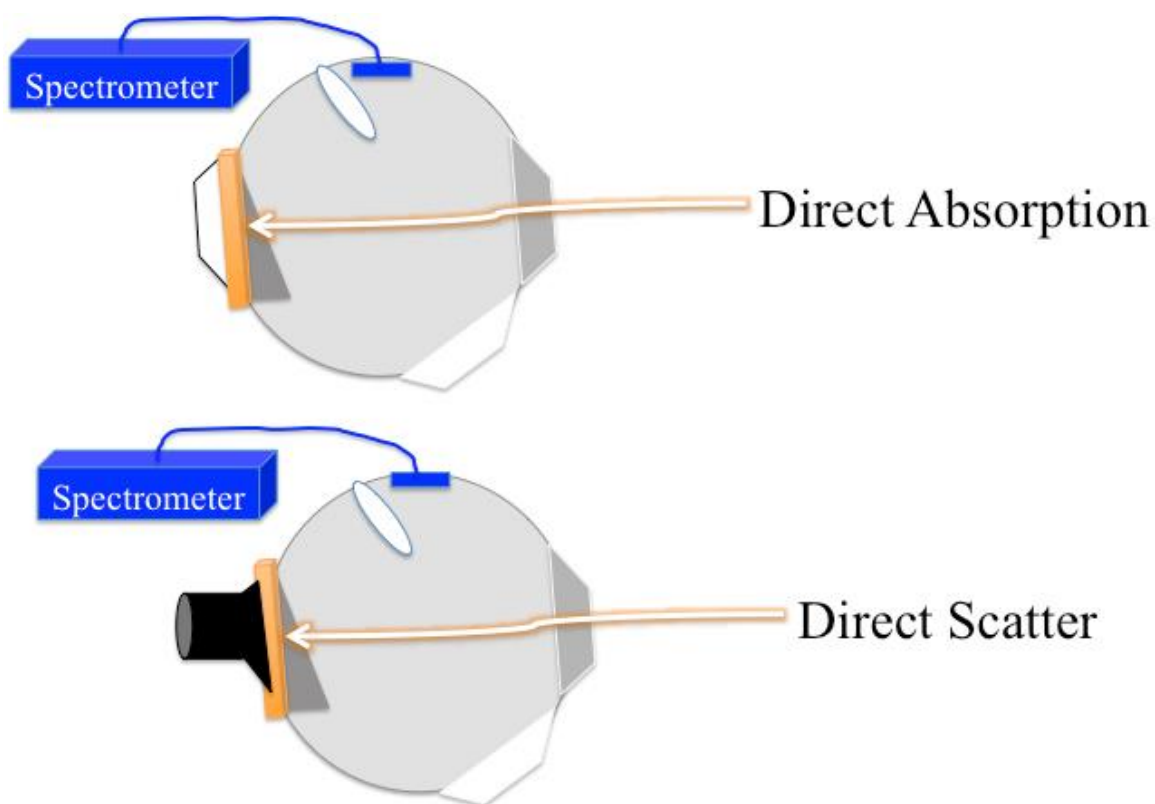


Figure 48: Integrating sphere set-up for direct absorption and scattering measurements, For the absorbance measurements, a white plug was placed behind the sample (orange rectangle). For the scattering, a black light trap was placed behind the sample so that only the scattering off the NPs were measured by the spectrometer fiber (blue port). The grey rhombus on each set up represents the open, entrance port for the incoming light. The white oval represents the baffle which prevents light coming directly off the sample into the detection fiber.

For the scattering and absorption experiments, a black plug and white plug were used, respectively. The orange rectangle represents the film sample and the white oval represents the baffle. In each case, the incoming light came through the entrance port and directly onto the sample. The direct absorption data was measured with the sample in the back of the integrating sphere with a white plug behind it. The forward scattering of the samples was measured by placing the sample in the rear of the sphere with a black light

trap behind it. Presumably, the only light that made it to the detector was scattered by the sample.

In both types of measurements, the data was corrected for with a plain glass slide as a control for “zero” absorbance and scattering. Figure 49 shows the scattering (black) and absorbance (blue) curves on an energy (eV) scale.

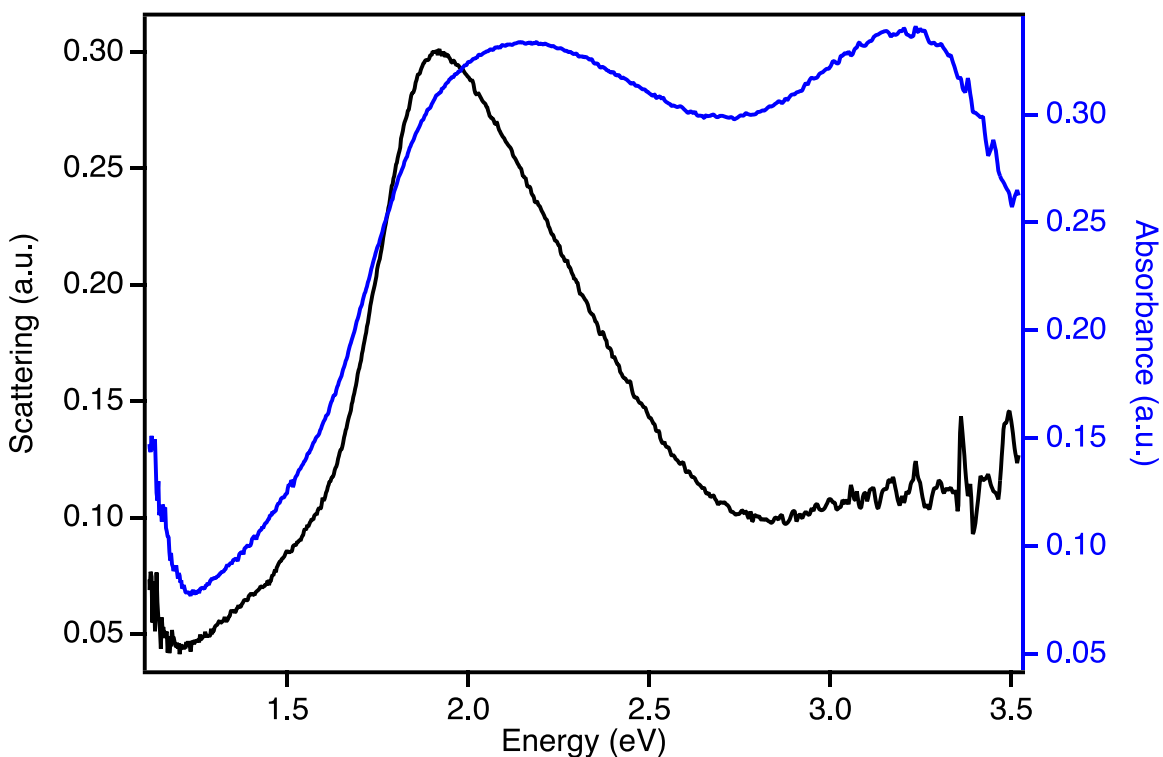


Figure 49: Scattering (left axis, black curve) and absorbance (right axis, blue curve) versus energy (eV) of Ag monolayer films made of washed NPs. The single scattering peak corresponds to the lower energy mode of the NPs absorbance. This may be due to the coherent plasmon resonance.

The scattering spectrum has two peaks and is slightly red shifted from the absorbance spectra. The absorbance spectrum (blue curve) shows two peaks: a bluer, transverse mode (≈ 3.1 eV), and a redder longitudinal mode (≈ 2.1 eV). The Ag NPs scattering (black curve) mainly comes from the longitudinal mode and is, as predicted by

Mie theory, slightly red-shifted (≈ 1.9 eV). Again, we were very interested in areas where the scattering was larger than the absorption for our application.

Next, I studied the scattering and absorption properties of films made from various sizes of Ag NPs. I wanted to prove that I could control the scattering and absorption properties of the monolayer films by altering the sizes of the NPs, themselves. We expected the smaller NPs to scatter higher energy light than the larger NPs. Furthermore, we expected smaller NPs to generate more uniform, closely (hexagonally) packed films than that of larger NPs due to the more narrow size distribution. The relationship between the absorbance (red) and scattering (blue) lowest energy peak (longitudinal mode) and the Ag:NaBH₄ ratio used to synthesize the particles is shown in Figure 50.

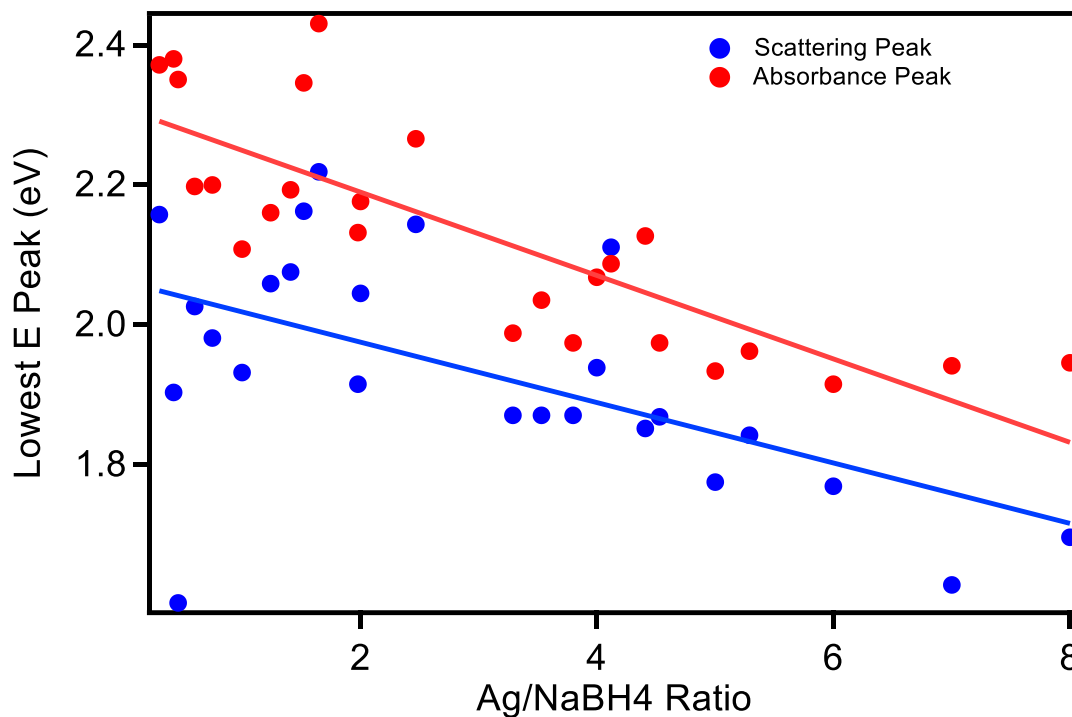


Figure 50: Lowest energy scattering (blue) and absorbance (red) peaks versus Ag:NaBH₄ ratio. A linear fit was performed on each data set highlighting the trend, which is a red shift with increasing ratio and thus the NP size.

As expected, the general trend is that the lower energy peak decreases in energy as the Ag:NaBH₄ ratio increases. The larger synthetic ratio produces larger particles, and thus lower energy plasmon peaks. The scattering spectra of films made with varying synthetic ratios (from 2.09-5.29) are shown in Figure 51.

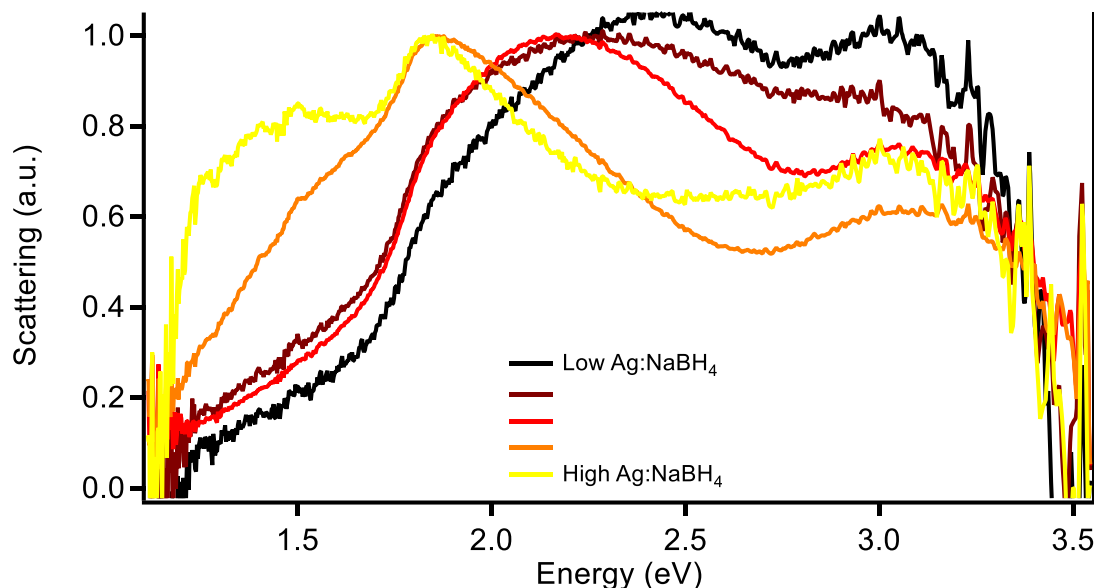


Figure 51: Scattering spectra of film series made with different sizes of Ag NPs. From black to yellow represents an increase in Ag:NaBH₄ ratio and thus the increase in size. There is a red shift in scattering as the NP sizes increase.

The curves from yellow to black represent the scattering trend as the Ag NP size decreases. As the NP size decreases, the monolayer films transverse scattering blue shifts. The longitudinal peak remains the same around 3.1 eV.

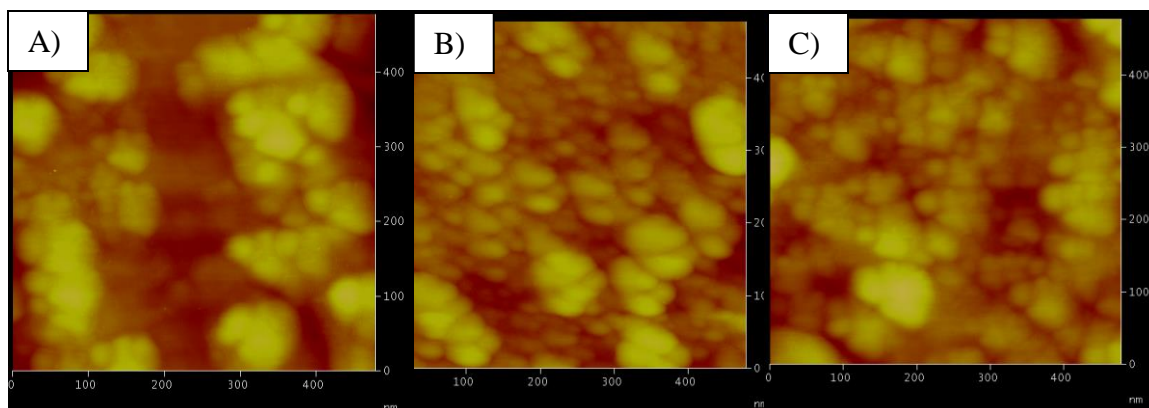
These integrating sphere experiments proved to us that the initial NP size can be used to tune the Ag monolayer film optical properties. This finding enabled us to tune the Ag NP monolayer scattering properties to be optimized at the energies above the MEG threshold of the QD layer. The packing and interparticle spacings can also affect the extinction of the NP films. The coherent plasmon resonance forms when the NPs are closer together. I studied this phenomenon by changing the soaking time of the films in the NP suspensions while keeping the particle size the same.

2.3.3.3 Optical SPR Dependence on Interparticle Spacing

I studied the film soak time in the Ag NPs to see how the inter-particle spacing on the films affected the scattering and absorption. The same size Ag NPs for all the films were used and only the film soaking time was varied. I expected that the longer soaking times would yield more dense particle packing and thus a stronger coherent plasmon resonance.

Initially, I studied the atomic force microscope (AFM) images of all the films as the soaking time changed (Figure 52). In tapping-mode atomic force microscopy, a high aspect ratio probe on a cantilever is oscillated right above the monolayer surface. A piezoelectric stage is moved to raster scan the probe across the surface. A laser beam is directed on the back of the AFM probe so that even the slightest changes in bends that the probe feels is detected. The repulsions the probe feels from the surface of the substrate is recorded and used to generate a topological map of what the probe “feels.” Since AFM is notorious for image distortions and false positives, extra care was always taken in calibrating the instrument, sample preparation, and autotuning the probe to shake off any particles or dust.

I used this data to calculate the particle density (NP/nm²) of 500 x 500 nm areas of the films. Each film was silanized and then soaked in the NP solution for a different amount of time: (Figure 52) A) 10 seconds, B) 600 seconds, and C) 2700 seconds.



10 seconds
78 particles
Density = 0.163 NP/nm^2

600 seconds
140 particles
Density = 0.292 NP/nm^2

2700 seconds
180 particles
Density = 0.376 NP/nm^2

Figure 52: Atomic Force Microscopy (AFM) images of Ag NP films with increasing soak times A) 10 seconds B) 600 seconds and C) 2700 seconds. The AFM area for each film was 500 nm^2 . The particles in each area were counted, and then the particle density was calculated (NP/nm^2).

I counted the approximate number of particles in the same area ($500 \times 500 \text{ nm}$) of each film and calculated the particle density for each soaking time. Next, I plotted the data and compared the particle density (NP/nm^2) determined by AFM, versus the film soak time (Figure 53).

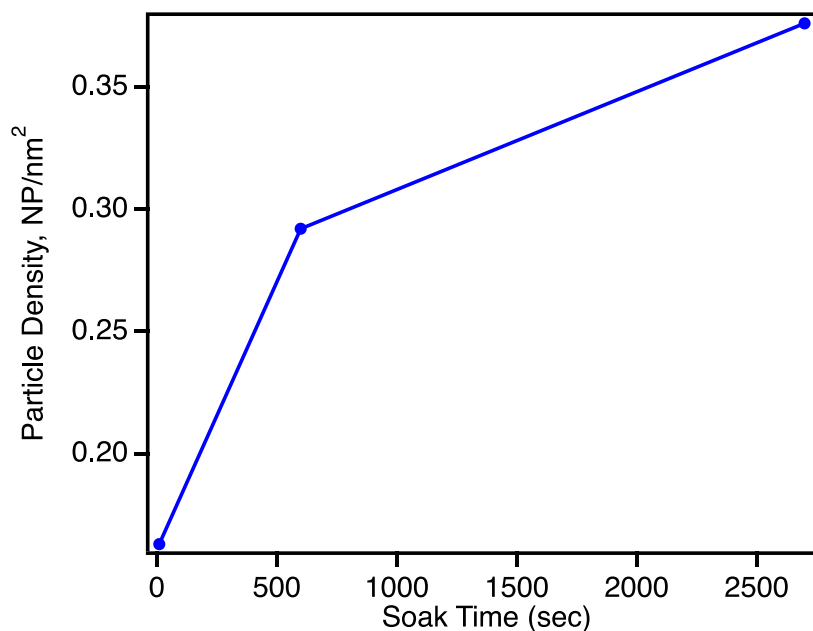


Figure 53: Particle density (NP/nm²) as determined by AFM versus soaking time (seconds) of films with the same size NPs. As the soaking time increased, the particle density increased.

As expected, the longer the films spent in the Ag NP solutions resulted in more NPs on the films. The larger particle density means smaller inter-particle spacing on the films. When the particles are closer together, the SPRs can interact and form a coherent plasmon resonance. To study the optical consequences of these interparticle interactions, I measured the film absorbances at different soaking times (Figure 54) using the aforementioned integrating sphere set-up.

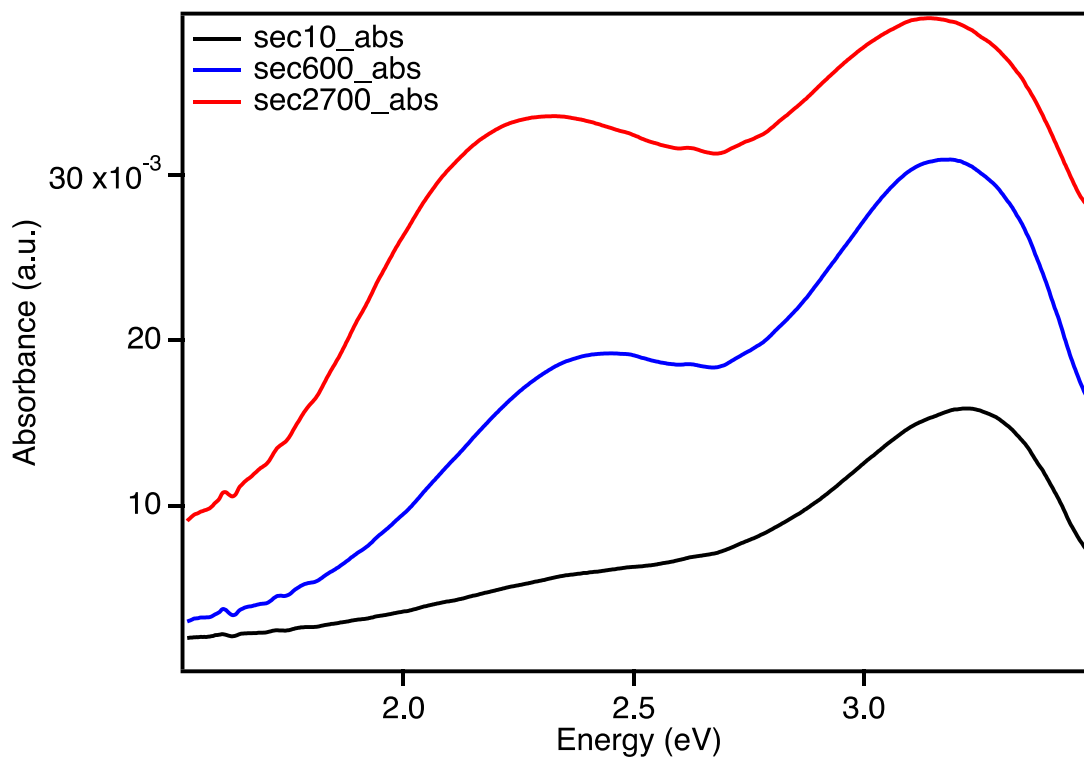


Figure 54: Film absorbance with different NP soaking times: (black) 10 seconds (blue) 600 seconds and (red) 2700 seconds. As the soaking time increases (from black to blue to red) the appearance of a higher order mode appears. This mode may be due to the formation of a coherent plasmon resonance as the interparticle distances decrease.

Figure 54 shows the absorbance of films that have soaked for 10 seconds (black), 600 seconds (blue) and 2700 seconds (red). As the soaking time and thus the particle density increased, the overall absorbance intensity and energy range increased. The lower energy peak that arises and intensifies as the soaking time increases can be attributed to the coherent plasmon resonance formed. Figure 55 shows the corresponding scattering spectra as the soaking time increased.

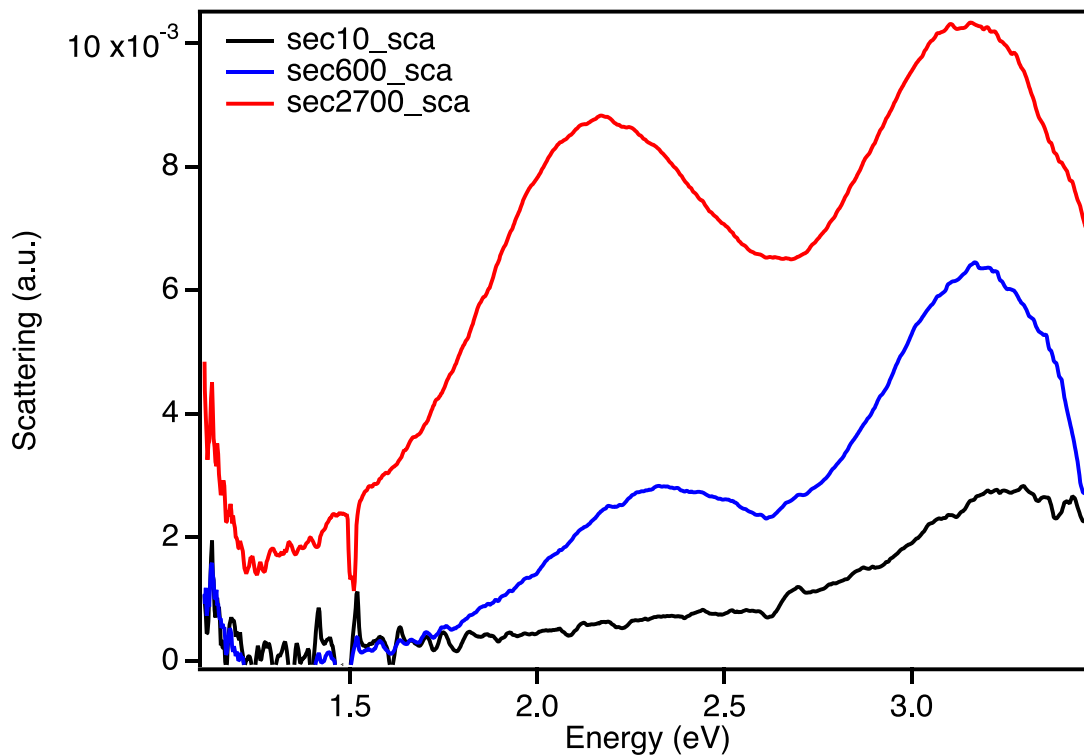


Figure 55: Film scattering with different NP soaking times: (black) 10 seconds (blue) 600 seconds and (red) 2700 seconds. As the soaking time increases (from black to blue to red) the appearance of a higher order mode appears. This mode may be due to the formation of a coherent plasmon resonance as the interparticle distances decrease.

The film absorbance and scattering drastically increase as the soaking time increased. The longitudinal peak may correspond to the coherent SPR because it appears after 600 seconds of soaking and increases in relation to the transverse peak after 2700 seconds. As the particles get closer together, the coherent plasmon increases in strength. With this knowledge, I was able to tune the Ag NP synthesis and the monolayer film fabrication to optimize the film scattering properties for our application of improving the

QD absorption properties. After learning about the Ag NP film application and properties, the next step was to apply the following layer of the film: the dielectric spacer.

2.3.4 Applying Dielectric Spacer and Determine Thicknesses

The enhancement of a fluorophores absorption by a metal NP SPR is known to be highly dependent on the distance between them. This component of the films is extremely important as it determines the QD-NP distance. The dielectric spacer consists of alternating charged polymer layers. The polymer preparation is as follows:

The negatively charged polymer, polystyrene sulfonate (PSS) (Figure 56) was prepared by combining 0.05 g of PSS with 25 mL of DI water and then sonicated for 20 min. The sonication step was vital to ensuring the even distribution and complete dissolution of polymer within the solution. Figure 56 shows the molecular structure of PSS. The sulfonate group on the bottom of the image is responsible for the negative charge of the polymer.

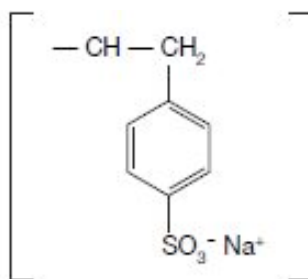


Figure 56: Structure of PSS, poly(sodium 4-styrene-sulfonate). The negatively charged sulfate group provides the polymer charge. The sodium ions are removed from the films by rinsing with water.

The positively charged, polyallyl amine (PAA) polymer (Figure 57) was prepared by first adding 143 uL of PAA to approximately 15 mL of water. A pH meter was calibrated to a

pH of 4, 7, and 10 by using pH buffer solutions. To positively charge the polymer (from Figure 57 A) to B)), the pH was adjusted from about 8.5 to 5.5 with a few drops of concentrated hydrochloric acid (HCl). Altering the pH to 5.5 ensures the protonation of the polymer by HCl. Finally, the concentration was changed by adding enough DI water to make the total volume 25 mL. The polymer solution was then completely mixed by sonication for 20 minutes.

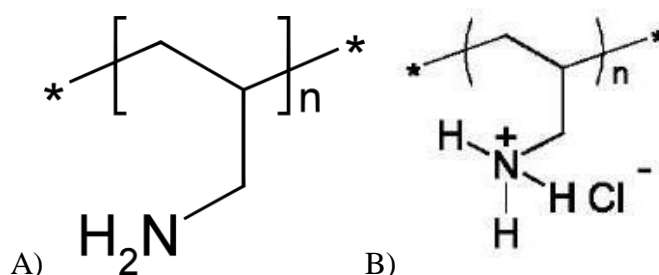


Figure 57: Structure of PAA before A) and after B) protonation by HCl. The pH of the polyallylamine was brought to 5.5 by the addition of HCl. The chlorine ions were washed away from the films by rinsing with water.

The two charged polymer solutions were then ready to be added in alternating layers onto the Ag NP monolayer by a spin coater.

Polymer Application: Each polymer layer was applied by spin coating a 300-uL aliquot onto a 1 x 1-inch slide (containing a monolayer of Ag nanoparticles). Between each layer application, the film was rinsed with two, 300-uL aliquots of milli-q water. The rinsing step was necessary to rinse away all of the excess ions like the sodium from the PSS polymer solution. The spin coater timers were set to 1.5 seconds (for ramp up) and 20 seconds (for spinning). Both speeds were set to 6.

The whole purpose of the polymer layers were to control the distances between the Ag and QD. To approximately determine the thickness added with each polymer

layer, I carried out a study on 0, 2, 4, 6, 8, 10, and 12 polymer layer samples. For every sample, a monolayer of (2:1 ratio) Ag NPs was first applied. I took AFM images of scratched areas of the samples to determine the height of the samples and created a calibration curve.

For the AFM step-height study, each film was scratched with a pair of clean tweezers and then blown off with compressed air. The number of polymer layers per sample ranged from 0-12 layers. I made doubles of each polymer layer thickness, and I performed three step height measurements per sample. An example of an AFM step height measurement is shown in Figure 58.

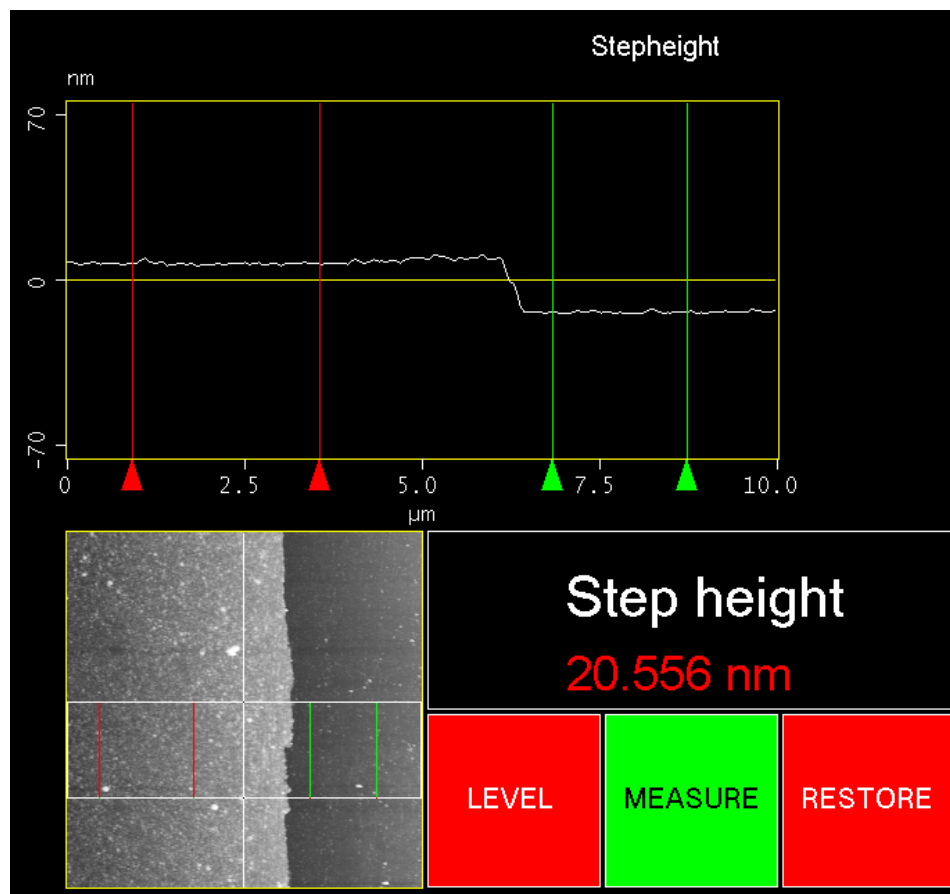


Figure 58: Example of the step-height measurement with AFM. The bottom left image represents the top-down view of the area that was measured. Here, the dark area is where the film was scratched away and the light, bumpy area is the polymer coated NP film. The red and green lines are the areas where the step differential was measured, revealing the thickness of the film.

In the top portion of Figure 58, a cross-sectional image of the step height measurement is shown. The lower left portion of the figure shows the actual AFM image that the step height was taken of. Notice that at this magnification, the scratch is not completely straight. The white spots on the non-scratched (left) side of the image represent the polymer coated Ag NPs. The red and green arrows show exactly where the height changes were measured.

The resulting calibration curve from the study are displayed in Figure 59. For each measurement, I subtracted out the average height of the base, Ag NP monolayer to

get an average polymer film thickness. The measurements with error bars are shown in red. A power law fit function was used to fit the data and the fit function is shown in the bottom right portion of the figure.

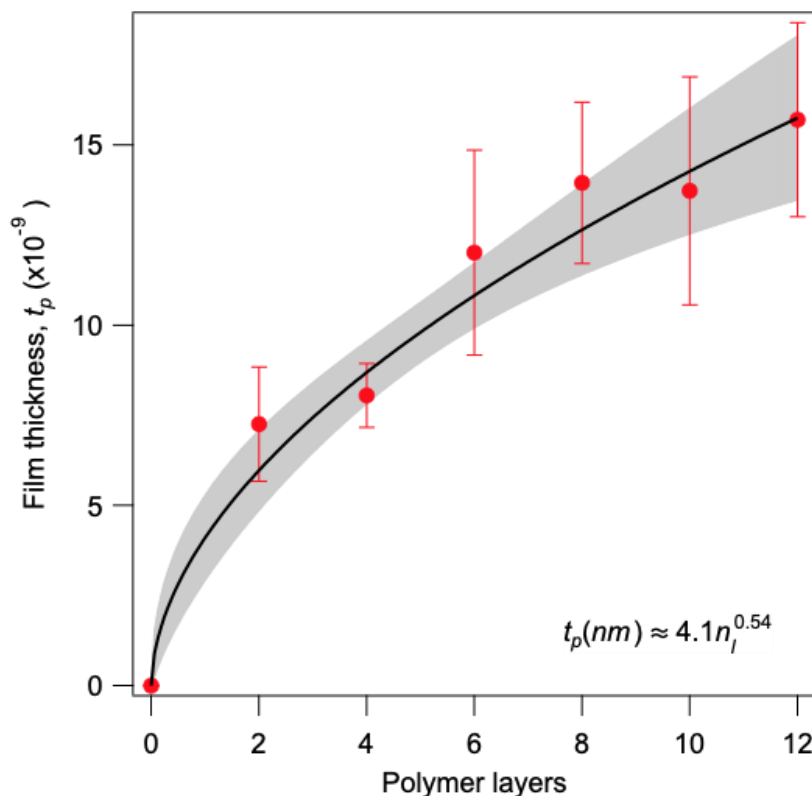


Figure 59: Average film thickness vs number of applied polymer layers. Measurements with error bars are shown in red and a power-law fit function was used to fit these (weighted) data. The gray shaded region indicates a confidence region \pm one standard deviation. The fit function is provided in the bottom right corner.

The shaded gray region represents a confidence interval \pm one standard deviation.

The y-axis represents the polymer heights in nanometers. The film heights had a large margin of error and increased with number of polymer layers. With this data, I estimated the polymer spacer thicknesses of films fabricated in the same exact way. The next portion of the project was to fabricate stable, monodispersed PbSe QDs for the top layer of the films.

2.3.5 Air-Stable PbSe QD Synthesis

Much like Ag NPs, a common issue with core-only PbSe QDs is that they are not very stable in air. I followed the work of Zhang et. al. out of Los Alamos Laboratory to synthesize air stable QDs, which maintain their QY in air for over 30 days.¹⁷⁵ Amazingly, with this procedure, they were able to fabricate PbSe QD solar cells with a record-breaking, 6 % power conversion efficiency!

In this method, they utilize CdSe QDs as an initial template for the PbSe QDs. Their work showed that the high QD stability in air results from the PbSe QDs having chlorine and cadmium ions passivating the QD's surface. The passivation occurs in situ from the cation exchange (between the Pb^{2+} and Cd^{2+}) and the byproduct of the dissolution of PbCl_2 .

The fabrication procedure is as follows: Se Precursor Preparation: A Se precursor solution was made by sonicating 0.3147 g elemental Se in 10 mL octadecene for 25 minutes. CdSe QD Synthesis: The size of the CdSe QDs determines the size of the resulting PbSe QDs. First, 0.5123 g cadmium oxide, 3.5 mL oleic acid, and 31.6 mL octadecene were combined in a clean, 3-neck round bottom flask equipped with a stir bar.

The mixture was heated to 260 °C while stirring rapidly under nitrogen for 20 minutes. Next, the reaction was cooled to 240 °C and 5 mL of the Se precursor was swiftly injected. The formation of QDs caused the reaction to turn bright orange. The flask was then immediately removed from the heat and allowed to cool naturally to room temperature. The QDs were washed with equal parts ethanol, chloroform, then again with ethanol. The resulting CdSe QDs were redispersed in 5 mL of octadecene.

Pb Cation Exchange Step: A flask with 10 mL oleylamine and 0.836 g lead chloride was brought to 80 °C under nitrogen for 30 minutes. The mixture was then heated to 150 °C, and the CdSe QDs in octadecene were injected. The suspension immediately turned dark grey. After 20 seconds, the flask was placed in a water bath. Once the reaction cooled to 75 °C, 10 mL anhydrous hexanes was added. At 40 °C, 8 mL of oleic acid was added and stirred for an additional 15 minutes. The resulting PbSe QDs were washed twice with ethanol and redispersed in anhydrous hexanes for spectroscopic measurements.

I first took TEM images of the PbSe QDs (Figure 60-61). The QDs had an average diameter of 3.306 ± 0.428 nm. Approximately 102 QDs were measured using imageJ. The small size and size distribution of the QDs were desirable to provide a thin, even layer on the Ag NP/polymer films.

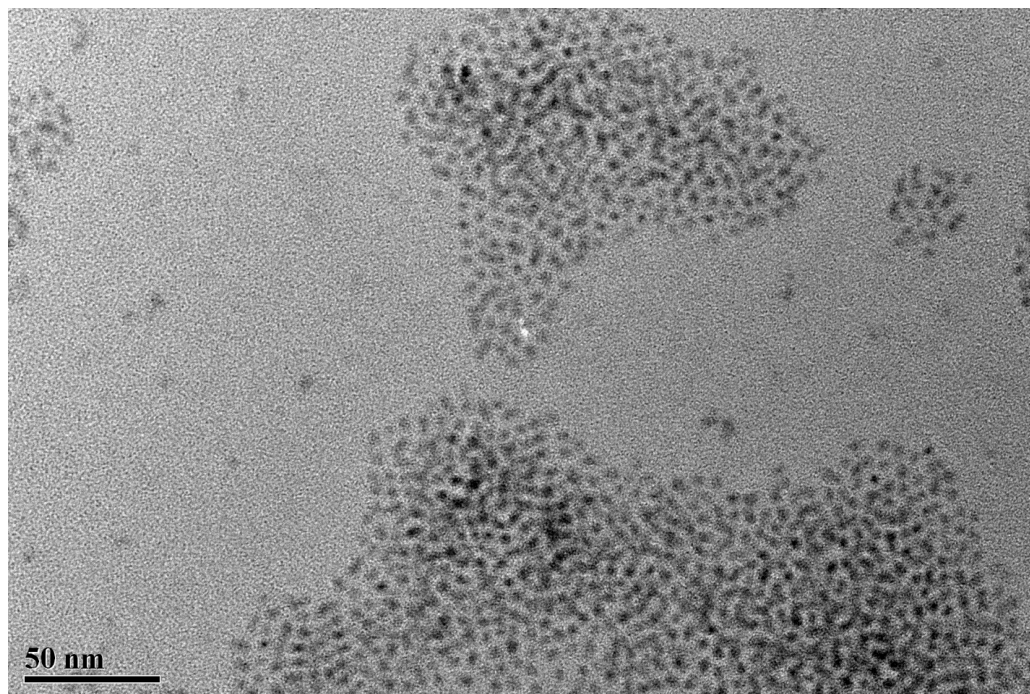


Figure 60: TEM image of air stable PbSe QDs. The scale bar is 50 nm. From this image, the average PbSe QD size was determined to be 3.306 ± 0.428 nm.

The scale bar in Figure 60 is 50 nm. This zoomed out image was captured to show that the QDs all had a similar size and shape. I confirmed that the particles were in fact QDs by taking a closer up image (Figure 61) to view the lattice fringes.

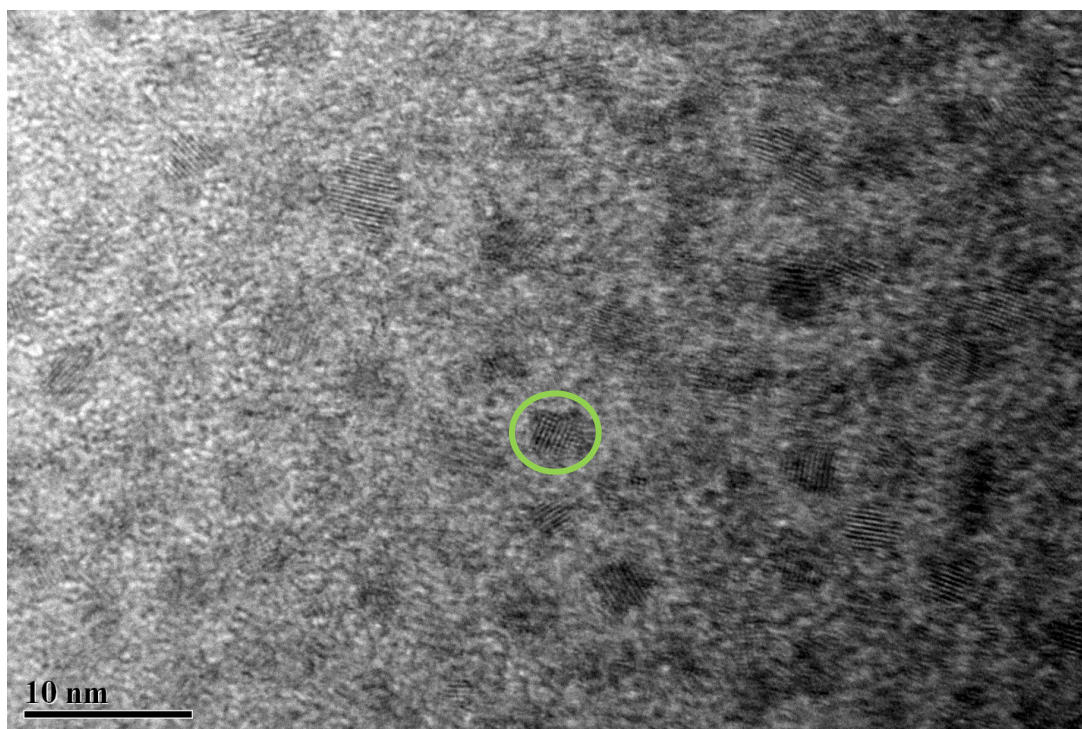


Figure 61: Close-up TEM image of air stable PbSe QDs. The scale bar is 10 nm. The green circle highlights a single QD. The lattice fringes are visible.

The scale bar in Figure 61 is 10 nm. The lattice fringes of the QDs nanocrystals are visible in this figure. The PbSe QDs are uniform, crystalline and highly spatially confined. The size of these QDs are much smaller than the exciton-Bohr radius. The electronic confinement of these QDs provide a favorable condition for wavefunction leakage and consequently, better charge carrier transport for solar cell applications.¹⁷⁵

These particles were used in the film study with and without Ag NPs present. The monoexponential nature of the TRPL data (Figure 62) of these QDs in hexanes supports the monodispersity observed in the TEM.

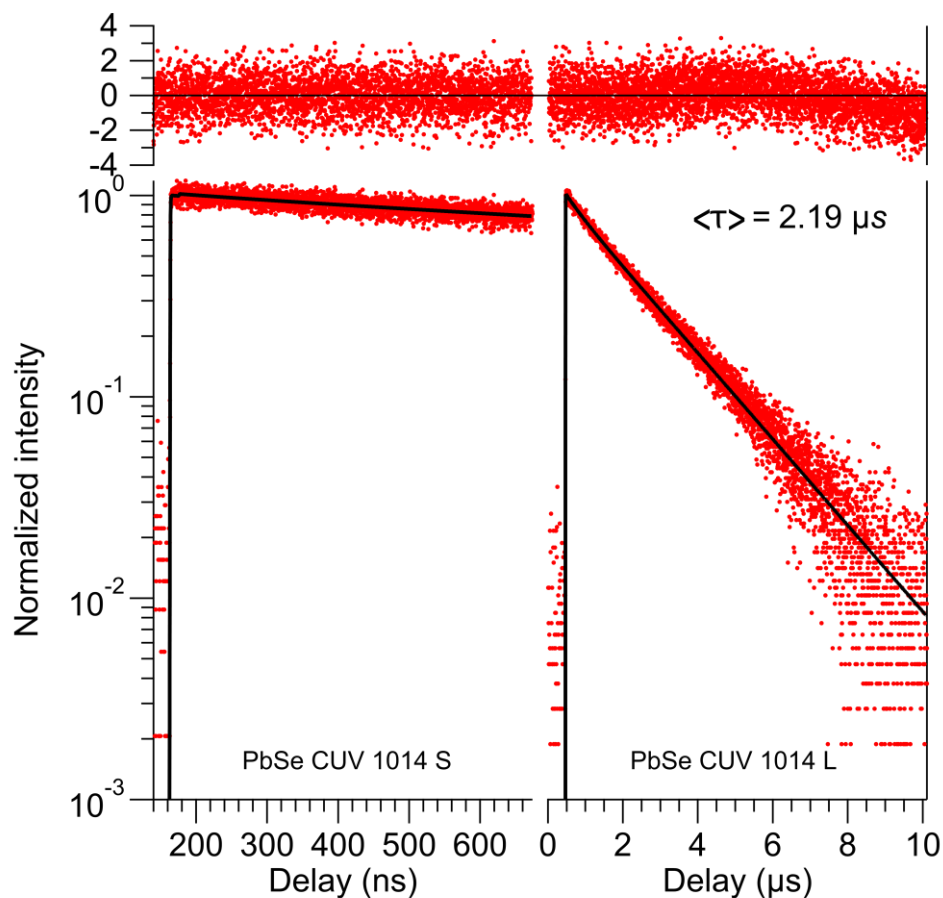


Figure 62: Lifetime decay of PbSe QDs suspended in anhydrous hexanes at 1014 nm emission. The left and right decays are in a small (700 ns) and large (10 μs) time window, respectively.

Figure 61 shows the lifetime data of PbSe QD emission at 1014 nm. The two curves represent different decay time windows. The PbSe QDs suspended in hexanes have a monoexponential lifetime of 2.19 μs . The next step was to assemble monolayer films of Ag NPs and QDs with controlled distances between them.

2.3.6 Complete Film Series Study Example

Many different film studies were carried out. For the sake of clarity, I am going to discuss one film series study. To begin this film study, I made a large batch (280 mL) of 1.75:1 (Ag:NaBH₄) Ag NPs to make 15 Ag NP monolayer films which have scattering that overlap well with the MEG threshold of the PbSe QDs. Of the 15 films, I studied 5

different polymer thicknesses in triplicate. The table below describes the layer contents of each film made.

Sample Label	Ag NP Monolayer?	# Polymer Layers	PbSe QDs
a	✓	0	✓
b	✓	0	✓
c	✓	0	✓
d	✓	2	✓
e	✓	2	✓
f	✓	2	✓
g	✓	4	✓
h	✓	4	✓
i	✓	4	✓
j	✓	6	✓
k	✓	6	✓
l	✓	6	✓
m	✓	8	✓
n	✓	8	✓
o	✓	8	✓
p	X	2	✓
q	X	4	✓
r	X	6	✓
s	X	0	✓
t	X	8	✓

Table 2: QD film series sample details. The sample names and corresponding layer contents are shown in the table. The blue sample labels represent the control samples since no silver monolayer is present, only PbSe QDs on glass or polymer layers.

Five samples (shown in blue) served as controls. These samples had no Ag NP layer but had varying polymer thicknesses. For all samples, 120 μ L of freshly sonicated PbSe QDs were spin coated as the final layer.

2.3.6.1 Integrating Sphere Experiments

To fully study these films, I took the absorbance and scattering at each stage of assembly. I started by taking the absorbance and scattering after the Ag NP application (Figure 63).

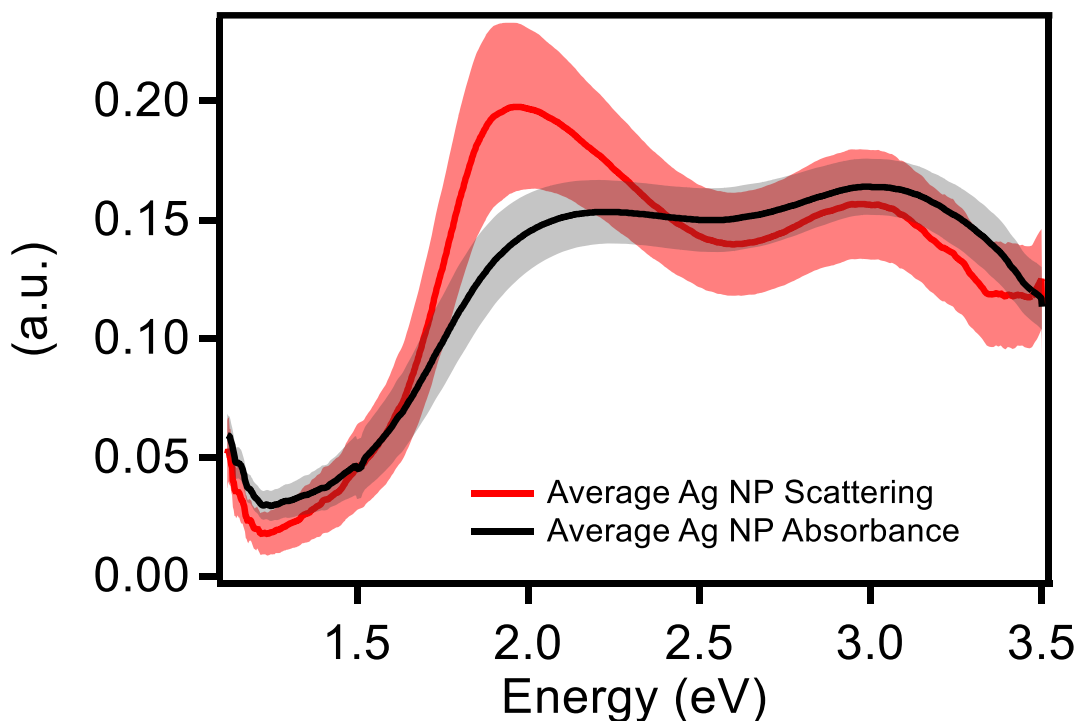


Figure 63: Average absorbance (black) and scattering (red) versus energy (eV) of 15 different Ag NP films made with the same size Ag NPs before polymer and QD application. The shading represents \pm one standard deviation.

At this point, samples a-o should have the same optical properties. Figure 62 shows that all the films have slightly different absorbance (black) and scattering (red) intensities; but keep the same general shape. From this data, the proportion of incident light scattered rather than absorbed was calculated by the equation below.

$$\text{Scattering Proportion} = \frac{\text{Scattering Spectrum}}{\text{Scattering} + \text{Absorption Spectrum}}$$

The scattering proportion is a very important value for our work because it represents the area of the spectrum where the potential of metal enhanced absorption is the greatest. Energies where the scattering trumps the absorption will have scattering proportion values above 0.5.

Figure 64 shows the average scattering proportions of these 15 films. The light green shading represents the standard deviation. At this point, the scattering proportion also remain the same general shape. These films have excellent scattering abilities.

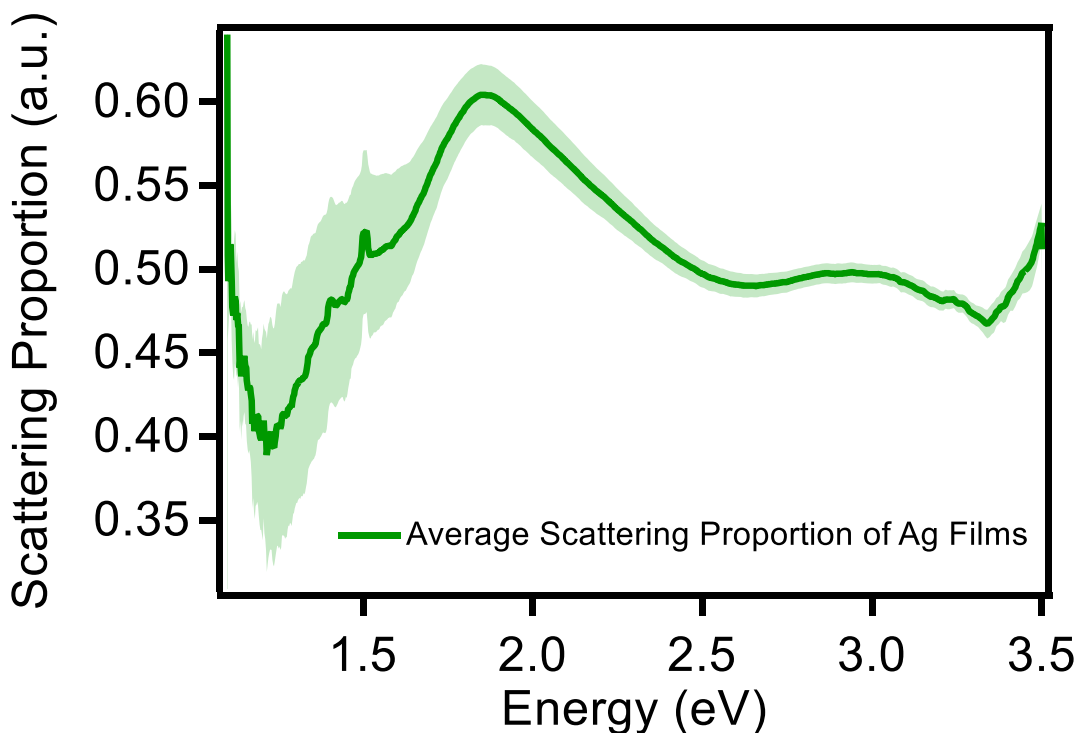


Figure 64: Scattering proportion versus energy (eV) of Ag NP films before polymer and QD application. The shading represents \pm one standard deviation. The areas at which the scattering proportion are greater than 0.5 mean that light at those energies is more likely to be scattered than absorbed by the Ag NPs.

Figure 64 show that the peak scattering proportion is approximately at 1.9 eV. At this energy, 60 % of the light extinguished by the film is scattered, not absorbed. We aim to

tailor this system to create films that scatter more light into the QD layer to boost photoabsorption. Moreover, the scattering properties of these films can be tailored for metal enhanced absorption or metal enhanced fluorescence for just about any fluorophore.

Next, I applied the dielectric spacer polymer layers according to Table 2. I studied the absorbance and scattering properties of the 5 different polymer thicknesses on glass alone (Figure 65). I took these measurements to prove to myself that the polymer optical properties alone are negligible and any changes it may bring to the Ag monolayer are due to the change in dielectric constant of the surrounding media (as predicted by Mie theory). Since these films had optical properties that did not have a trend or vary in shape, I plotted the average absorption (black) and scattering (blue) in Figure 65. The shading represents the standard deviation.

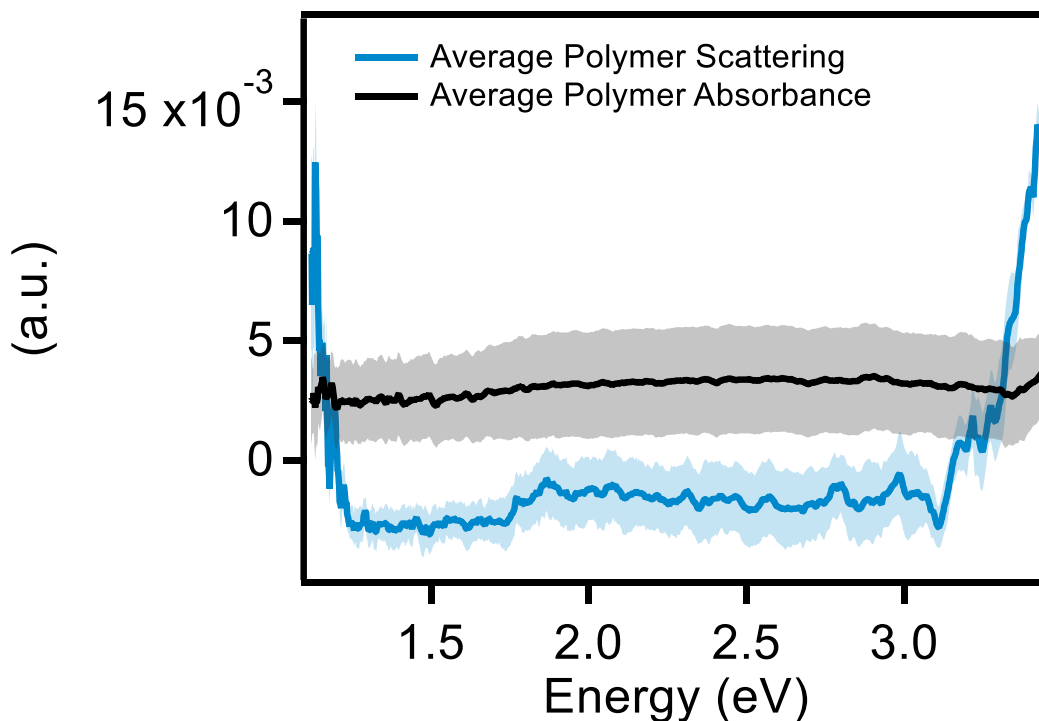


Figure 65: Average absorbance (black) and scattering (blue) versus energy (eV) of plain polymer films of varying thicknesses. The shading represents \pm one standard deviation.

Overall, the scattering and absorption of polymer-only film are very small. Most of the scattering measurements of these films was at/below zero. There is a slight feature in all the scattering spectra around 1.88 eV, while the absorbance remains flat. Though presence of polymer alone does not affect the optical properties much; Mie theory predicts that it should affect the Ag NP films because it will change the surrounding dielectric constant. The effects upon addition of 2 polymer layers are shown in Figure 66.

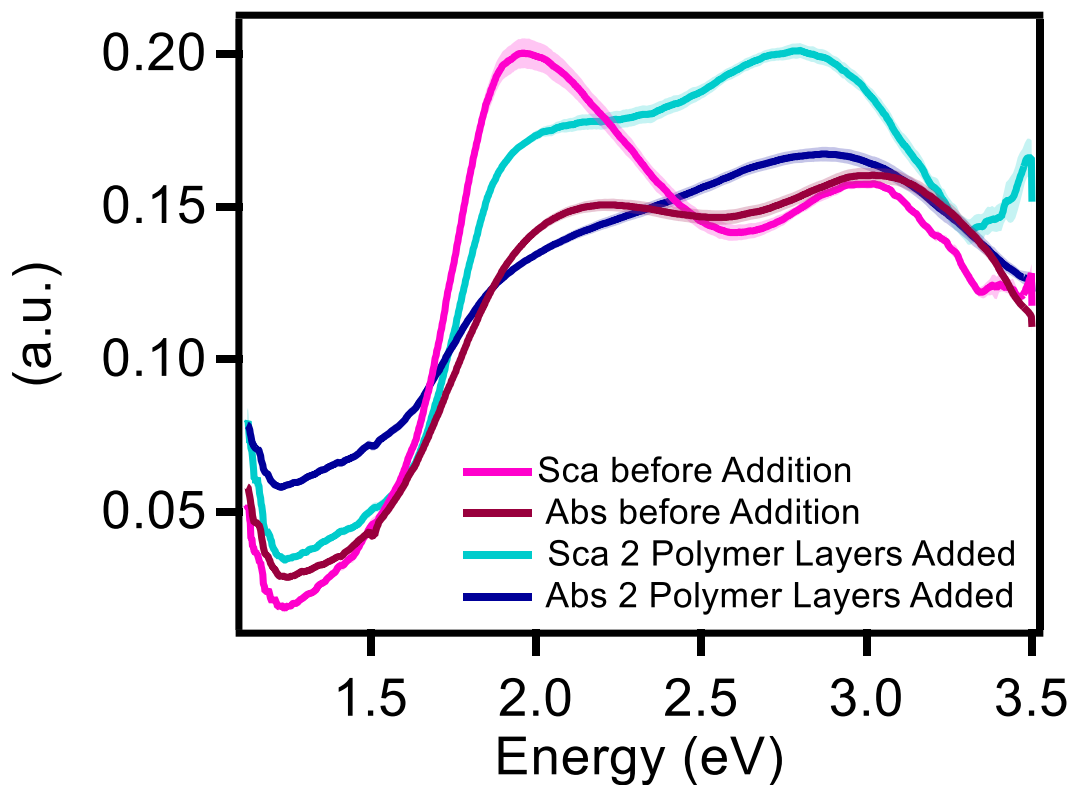


Figure 66: Average absorption (dark) and scattering (light) before (light and dark pink) and after (dark and light blue) two polymer layers added (in triplicate). The shading represents \pm one standard deviation.

In Figure 66, the dark pink and light pink curves are the absorbance and scattering of the films before polymer addition, respectively. The dark blue and light blue curves are the absorbance and scattering of the films after 2 polymer layers were added, respectively. The shape of both the average absorbance and scattering of the films changes upon the polymer addition. The two peaks broaden, come closer together, and are shifted to greater energies. A clearer picture of the implications of the polymer addition in terms of our needs is shown in Figure 67. The average changes in scattering proportion from before (black) to after (blue) two layers of polymer were added are shown here. The shading represents the standard deviation.

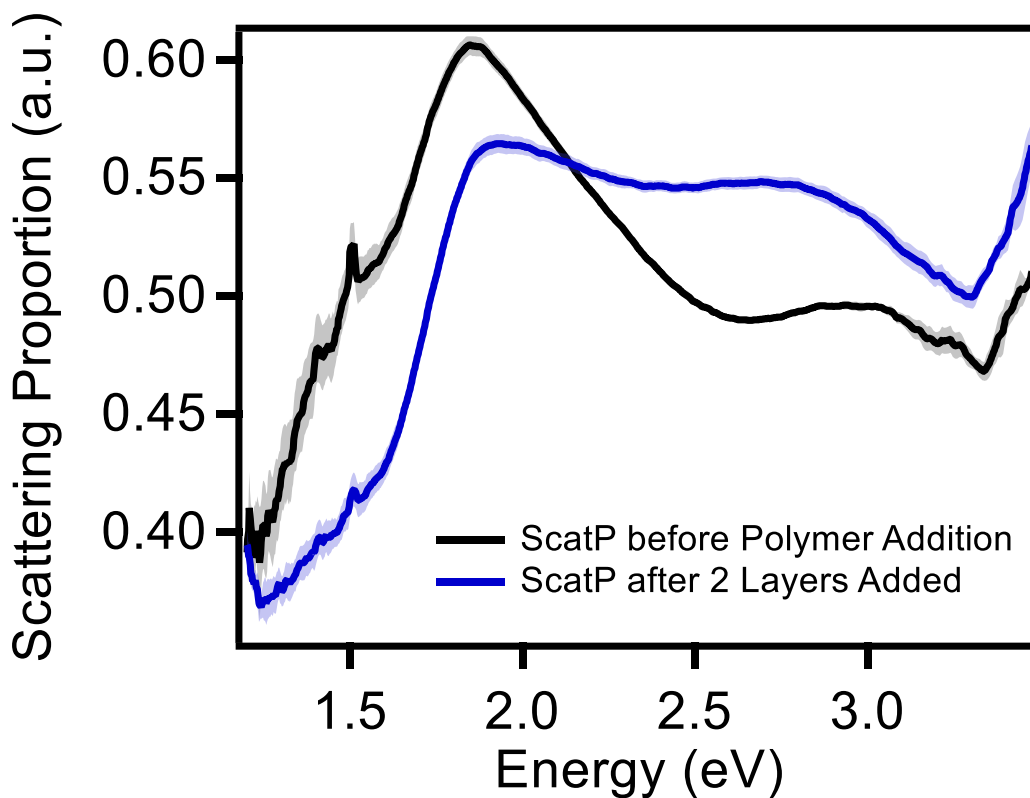


Figure 67: Average scattering proportion changes upon two polymer layer additions. The black curve represents the scattering proportion before polymers were added and the blue curve represents the scattering proportion after 2 polymer layers were added. The shading represents \pm one standard deviation. The change in scattering proportions can be attributed to the change in the NPs surrounding dielectric environment.

After two polymer layers were added, the films scattered less incident light at low energies (0.75 – 2.1 eV) and more light at greater energies (2.1 – 3.5 eV). This effect is great for our application because the MEG threshold ($2.5E_g$) of the PbSe QDs is approximately 2.8 eV. A similar effect can be seen upon the addition of 4, 6, and 8 polymer layers. A “zoomed in” image illustrating this effect is shown in Figure 68. The

shading represents the respective standard deviations.

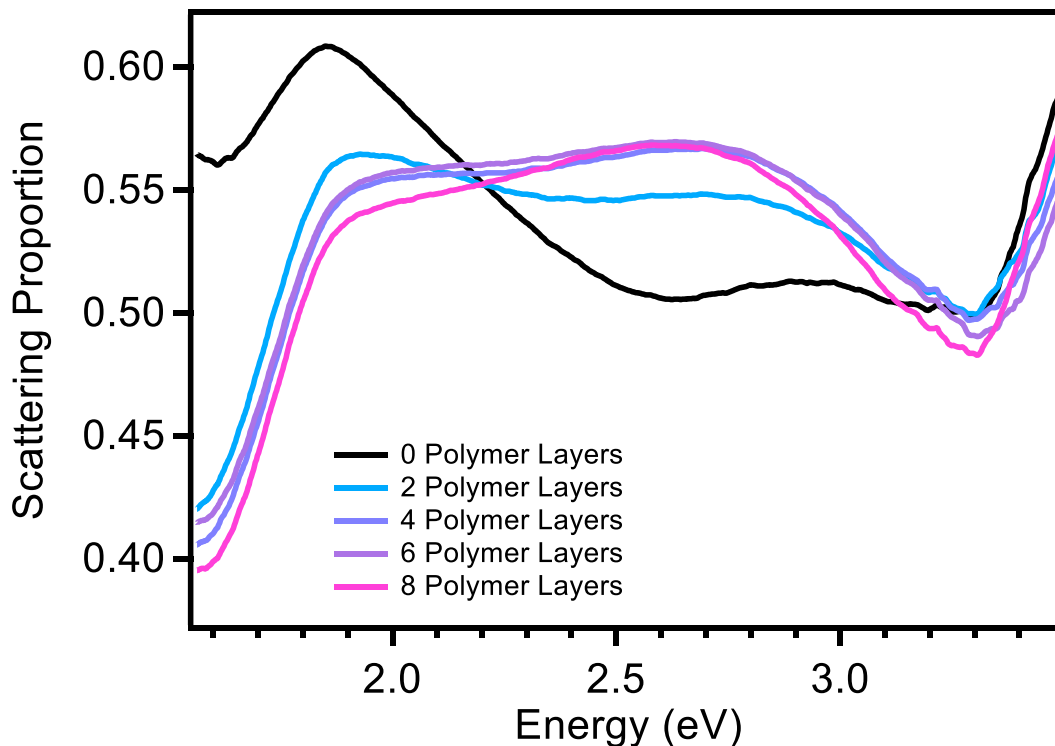


Figure 68: Average scattering proportion of films with different # of polymer layers. The black curve represents the scattering proportion of the Ag NP film before polymer addition. The curves from light blue to pink represent an increase in number of polymer layers.

It is interesting to point out that 2 polymer layer Ag films scatter very well in the red, while 4, 6, and 8 polymer layers scatter better in the blue. Again, as more polymer layers are added, the better the scattering proportion at greater energies. For all samples, the scattering proportion values showed excellent promise for enhancing QD absorption. I spin coated QDs on slides without Ag NPs to see how the QDs alone scatter and absorb light.

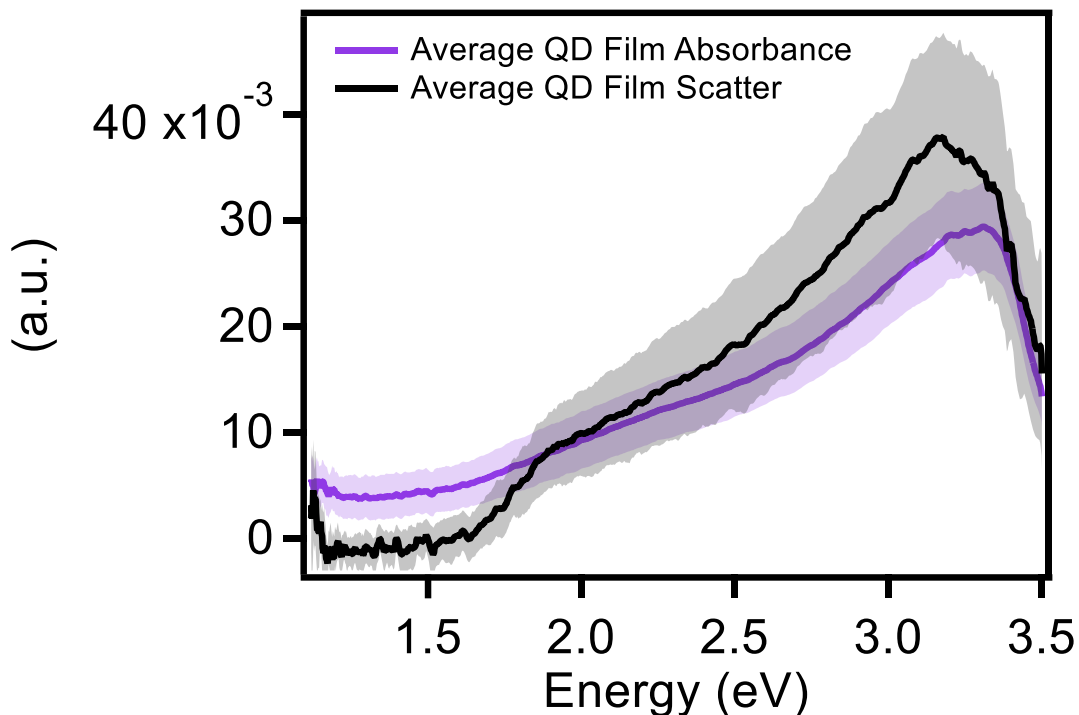


Figure 69: Average absorbance (purple) and scattering (black) versus energy (eV) of QD control films (on 0, 2, 4, 6, and 8 polymer layers). The shading represents \pm one standard deviation.

Figure 69 shows the average absorbance and scattering properties of the control films consisting of QDs spin coated on 0, 2, 4, 6, and 8 polymer layers. The shading represents one standard deviation. There is a small absorption and scattering peak at 3.15 eV. These optical properties are relatively minimal and there are no major spectral differences between the films. The slight variations between films can be attributed to QD loading differences. I was curious to see if there were any synergistic effects when the QDs were couples to the metal NPs.

First, we must take into consideration the change in dielectric constant caused by the QDs on the Ag monolayer. Based on the TEM calibration curve, the synthetic ratio I used should yield approximately 20 nm in diameter Ag NPs. I plugged the radius and

refractive indices of the surrounding media to the Mie equation to the expected spectral changes due to the surroundings (Figure 70).

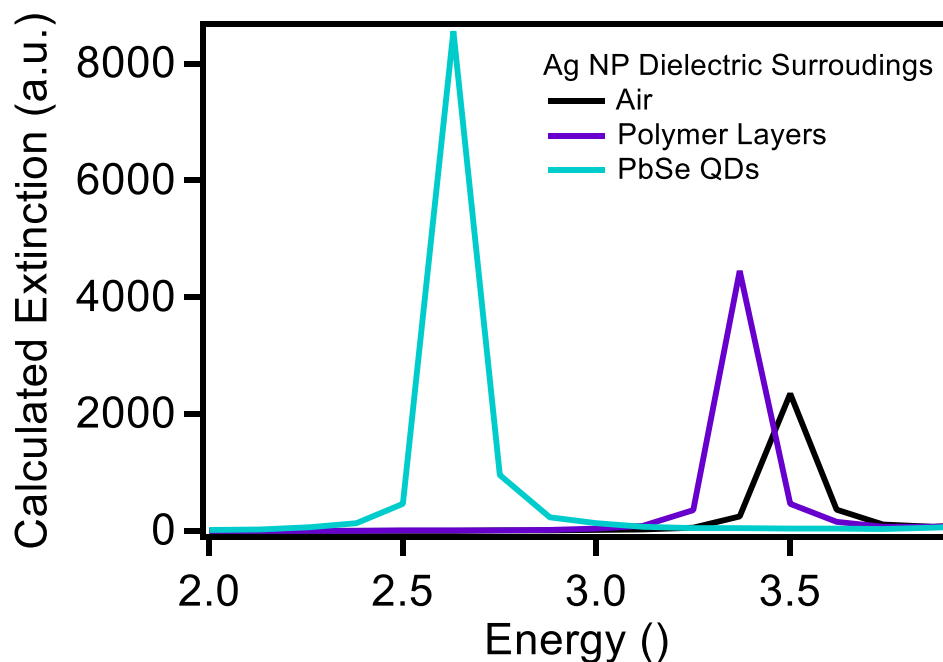


Figure 70: Mie theorized extinction versus energy (eV) of 20 nm diameter Ag NPs in the presence of air (black) PAA and PSS polymer layers (purple) and PbSe QDs (light blue).

Figure 70 shows the theorized extinction of 20 nm diameter Ag NPs in the presence of air (black) PAA and PSS polymer layers (purple) and PbSe QDs (light blue). I did this rough calculation to estimate the spectral shifts that I may observe due to the dielectric constant, not interparticle distances. The data shows that I should expect a strong red shift after the application of (3 nm diameter) PbSe QDs, which have a large dielectric constant.

A synergistic effect due to near-field coupling between NIR QDs and Ag NPs has been seen in the theoretical work of Pelayo Garcia de Arquer et. al. They modeled the extinction enhancement of PbS QDs in the presence of varying concentrations of Ag

NPs.¹⁷⁶ Their work is relevant to ours because they predicted the absorption enhancement NIR QDs caused by a nearby SPR. They calculated and compared the “gain” in absorption of PbS QDs blended in polymer and varying concentrations of Ag NPs as a function of wavelength.¹⁷⁶ The spectral gain was defined as follows:

$$Gain(\lambda) = \frac{Absorbance_{with\ NPs}}{Absorbance_{without\ NPs}}$$

The Ag NPs were within the near field of the QDs (5-10 nm) and were sensitive to concentration changes thus distance. The absorption changes a) and the changes in gain (inset) of Figure 71 shows this effect.

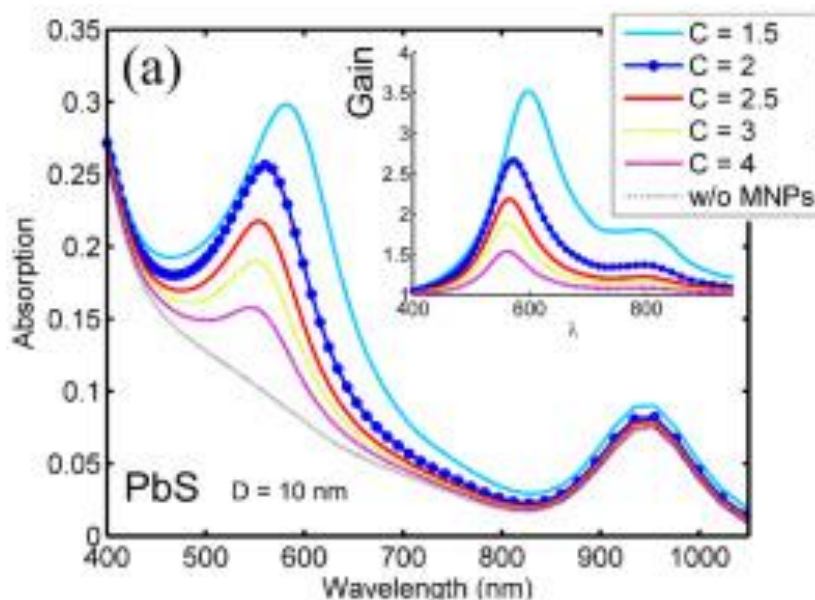


Figure 71: Theoretical absorption changes of Ag NPs in the presence of PbS QDs. Each trace represents a different Ag NP concentration (C) and thus different QD-NP distances. The C values 1.5-4 represent area densities of 20-5 %, respectively. The insets show the respective calculated gain.¹⁷⁶ © de Arquer, F. P. G.; Beck, F. J.; Konstantatos, G., *Absorption Enhancement in Solution Processed Metal-Semiconductor Nanocomposites*. [2011] Optical Society of America.

This theoretical work showed that there is a broadband absorption enhancement of the PbS QDs due to the SPRs in the near field because the gain was observed in energies outside of the SPR, alone. However, the maximum enhancement was found at

energies of the SPR resonance.¹⁷⁶ As expected, this near field coupling absorption enhancement was distance dependent. As the distances became shorter between the QD and NP ($C = 4-1.5$), the gain factors increased.

With our system, we have a more precise control over the NP and QD distance by changing the number of polymer layers between the PbSe QD and Ag NP monolayers. Furthermore, we can separate the extinction gain into absorption and scattering gain. If the SPRs were enhancing the QD absorption, we would expect to see a large gain. We also expect to see a change in gain with respect to QD-NP distances. I calculated the gain in scattering of the films and plotted them in Figure 72 to compare. The dashed red curve corresponds to the red axis on the right and represents the average Ag NP scattering.

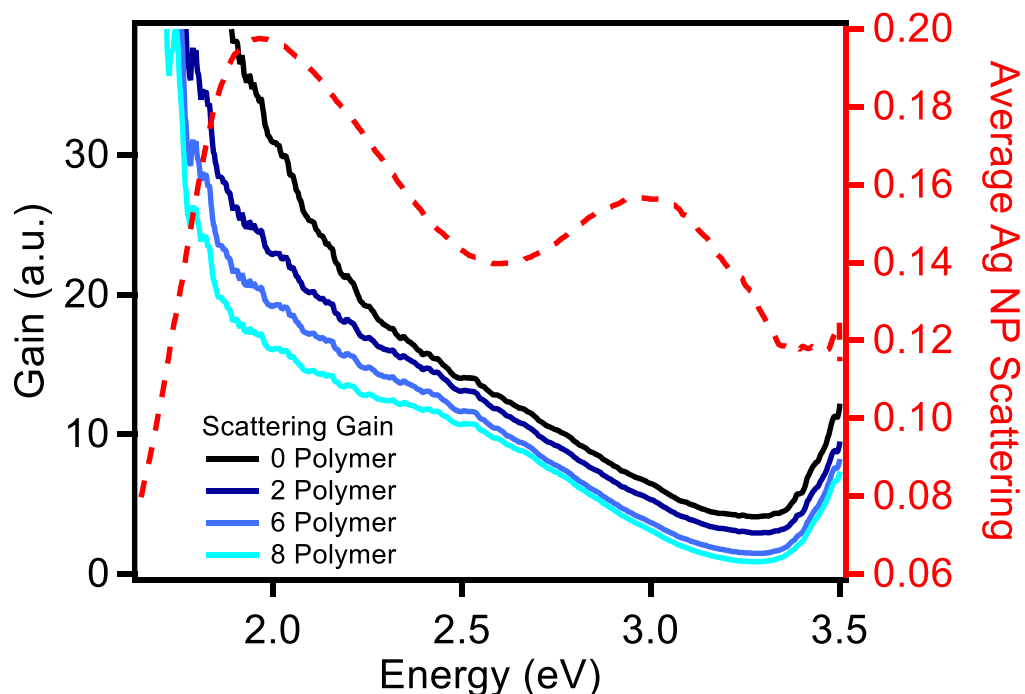


Figure 72: Calculated scattering gain versus energy. From black to light blue represents an increase in NP-QD distance. The red curve corresponds to the right axis and represents the average Ag NP scattering.

Just as the theoretical work on PbS QDs showed, we found an increase in the scattering gain as the QD-NP distance increased (black curve to light blue). The black curve represents a film without any spacer between the Ag and QD monolayers. This showed the greatest scattering gain. Since we are most interested in the absorption enhancement, I also calculated the absorption gain (Figure 73). Here, I show only 0, 2, and 8 polymer spacings for clarity purposes.

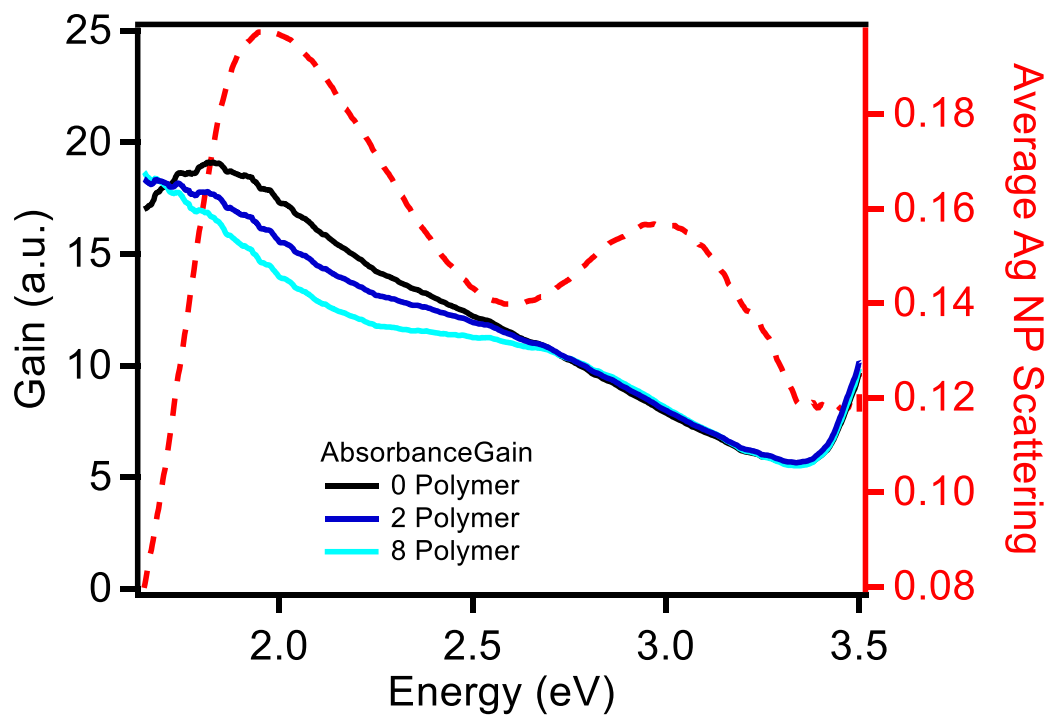


Figure 73: Calculated absorbance gain versus energy. From black to light blue represents an increase in NP-QD distance. The red curve corresponds to the right axis and represents the average Ag NP scattering.

As the spacing between the QD and NP increases (black curve to light blue), the absorption gain decreases. The gain for the zero spacing (black curve) clearly shows a peak corresponding to the Ag NP scattering peak. The red shift is due to inter-particle

interactions and the change in dielectric constant. The signature of the Ag NPs in the absorption gain seems to diminish as the spacings become large (light blue).

From these data, I also calculated the “QD contribution” by subtracting the [Ag + polymer] spectra from the corresponding [Ag + polymer + QD] spectra. If there were no synergistic effects, then the resulting spectra should look just like the QDs alone in Figure 68. The calculation was performed to observe possibly coupling trends and is described again below.

$$qd\ contribution_{abs} = (Ag + Polymer + QD)_{abs} - (Ag + Polymer)_{abs}$$

Figures 74 and 75 show the resulting QD contribution to the film scattering and absorbance, respectively. Right away, it is apparent that the spectra in Figure 74 look nothing like the QDs alone. I plotted the average Ag NP scattering (red curve) which corresponds to the right axis to compare the curve shapes.

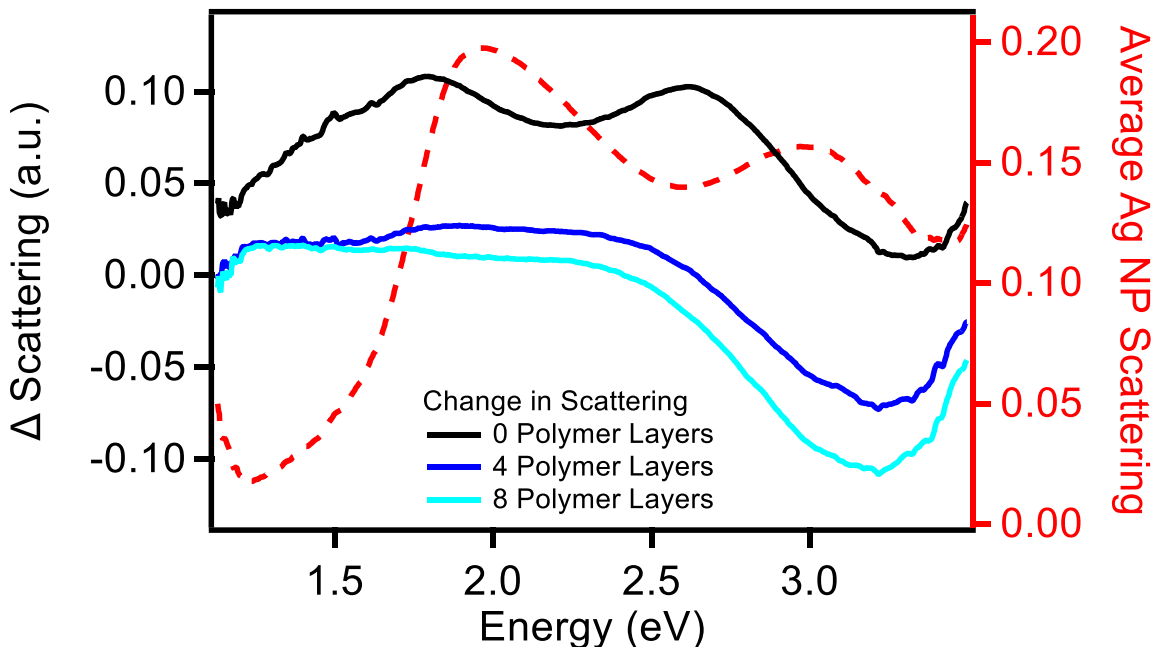


Figure 74: Change in film scattering versus energy (eV) with increasing polymer spacer thickness. The red curve corresponds to the right axis and represents the average Ag NP scattering. The black, dark blue, and light blue curves represent 0, 4, and 8 polymer spacer layers between QD and NP, respectively.

Figure 74 shows the scattering contribution from the QD-NP interactions. The closer the QDs are to the Ag layer (from light blue curve to the black), the more the spectral shape resembles the average Ag NP scattering alone (red curve). This suggests that the Ag NP scattering is “enhanced” by the presence of QDs; possibly due to near field coupling. The red shift in the peaks seen from the red to the black curve was predicted due to the changes in dielectric constant brought on by the presence of PbSe QDs. This synergistic effect suggests that there is more coupling via scattering between QD and NP when they are closer together.

The same analysis was done on the absorbance contribution and is shown in Figure 75. The red curve represents the average PbSe QD absorbance and corresponds to the red axis. The other two curves represent the change in Ag NP absorbance brought on

by the presence of QDs when there is no spacing (black) and when there is great spacing (blue).

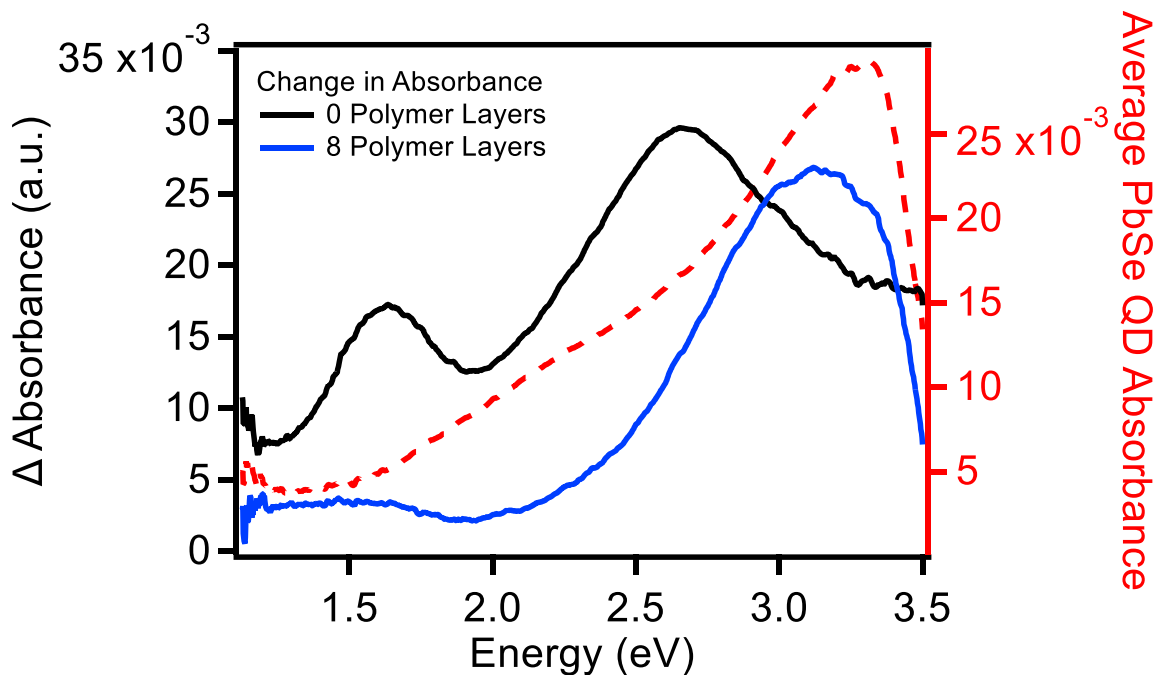


Figure 75: Change in film absorbance versus energy (eV) with increasing polymer spacer thickness. The black and dark blue curves represent 0 and 8 polymer spacer layers between QD and NP, respectively. The red curve corresponds to the right axis and represents the average PbSe QD absorbance.

I plotted the average PbSe QD absorbance (red) to point out that as the spacings get far apart between the Ag NP and QD (blue curve), the change in absorbance due to QDs look just like the QDs alone. This told us that there is little to no near field coupling when the two layers are far apart. This makes sense because 8 polymer layers represents a spacing of approximately 14 nm; which is out of the near field.

In contrast, change in absorbance due to the presence of QDs when there is no particle spacings (black curve) shows some near-field coupling effects. To show this, I plotted the same change in absorption data, but this time with the average Ag NP absorbance (red) on the right axis in Figure 76.

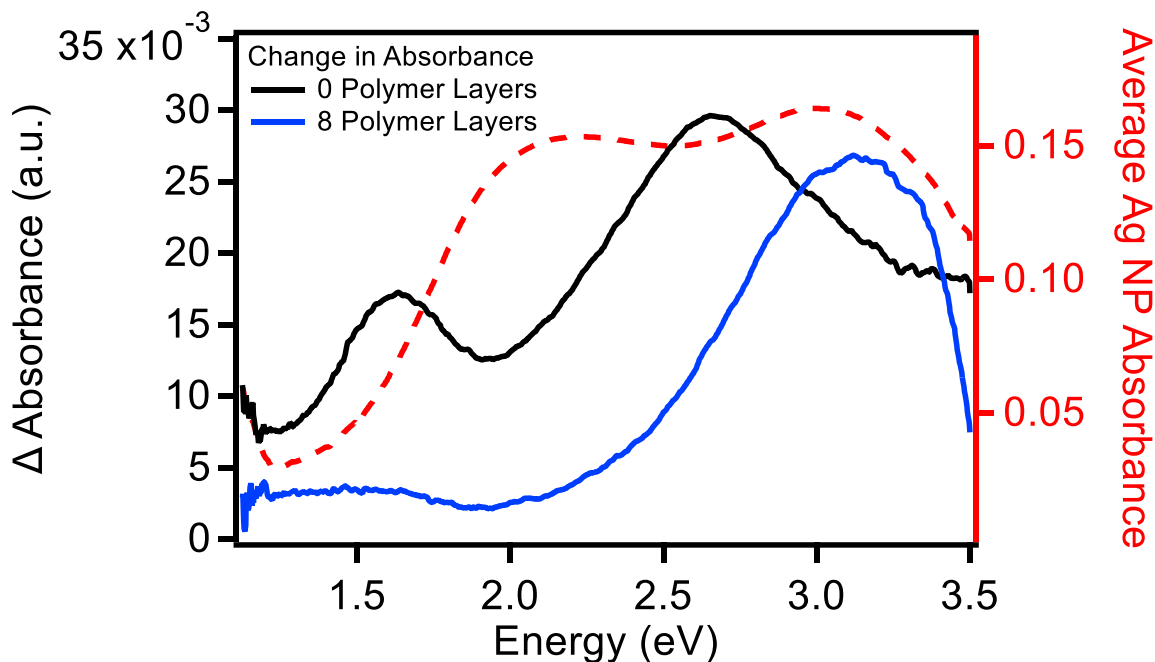


Figure 76: Change in film absorbance versus energy (eV) with increasing polymer spacer thickness. The black and dark blue curves represent 0 and 8 polymer spacer layers between QD and NP, respectively. The red curve corresponds to the right axis and represents the average Ag NP absorbance.

Figure 76 shows that the QD contribution to the absorbance broadens and looks more like the Ag NP absorbance alone as QDs are closer to the Ag layer. The two peaks are red shifted due to the change in dielectric constant of the surrounding media due to the PbSe QDs. Figure 77 shows the trend in scattering proportion of the films when there is no spacing (black) 4 polymer layer spacing (dark blue) and 8 polymer layer spacing (light blue) between the QDs and NPs.

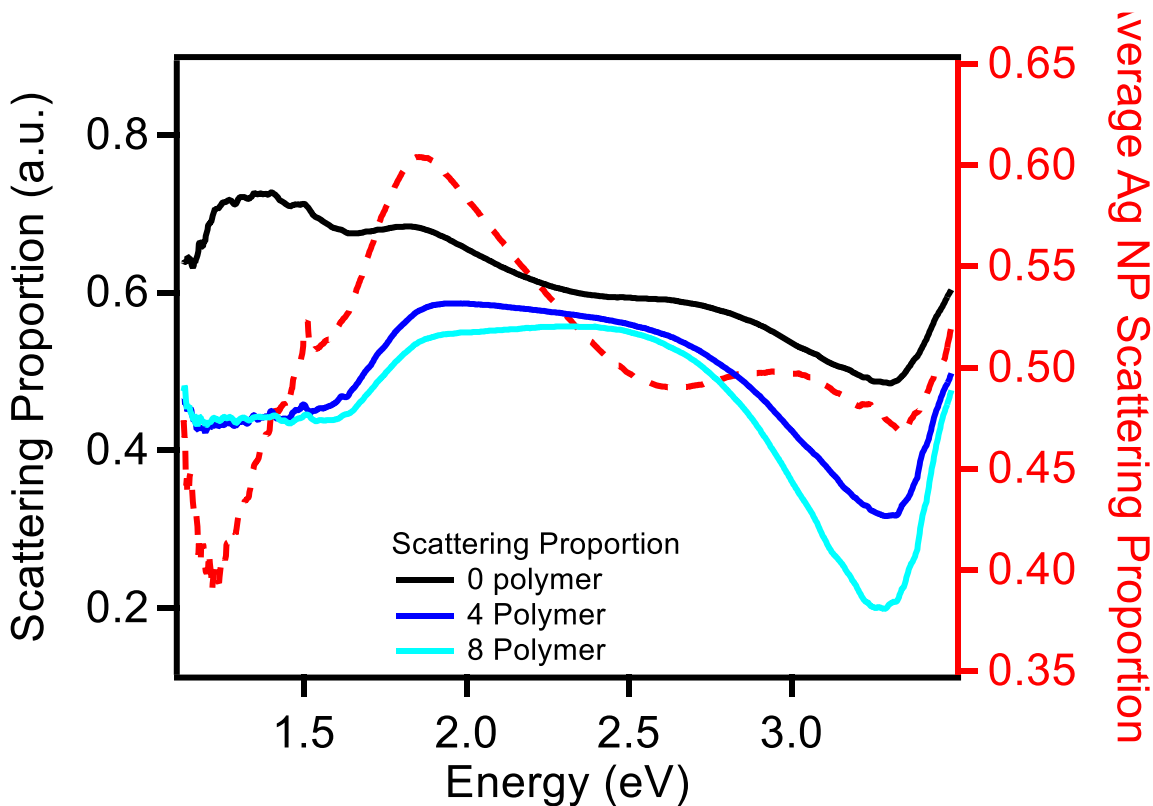


Figure 77: Scattering proportion versus energy (eV) of total films as the QD-NP distances get smaller (light blue to black). The red curve corresponds to the right axis and represents the average Ag NP scattering proportion.

Figure 77 shows that the overall scattering proportion of the films increase as the NP-QD spacings decrease. This may be due to the near field coupling between the two layers. Furthermore, there is an appearance of more scattering proportion peaks as the layers get closer (black). I plotted the average Ag NP scattering proportion in red (corresponds to the red axis).

The data in Figures 75-77 suggest that there is a synergistic, coupling effect between the metal NPs and QDs. This effect gets progressively more pronounced the closer the layers get together. We can already see absorption and scattering enhancement of the total films because the NP and QD coupling. This is a very interesting finding

because we only expected to see NP-QD coupling through the fluorescence of the QDs, not merely the extinction of the Ag NPs. The next step was to determine the photoluminescence excitation changes of the QDs in the presence of Ag NPs.

2.3.6.2 Steady State Emission

Steady state emission studies of the PbSe QDs give information on the QD bandgap energy (E_g). The MEG threshold, or the minimum energy needed to generate multiple excitons, can be determined by multiplying the bandgap energy by 2.5. To see possible changes in intensity and shape, these studies were carried out on PbSe QD films with and without the presence of Ag monolayers. I studied the photoluminescence at excitation energies above (410 nm) and below (565 nm) the MEG threshold ($>2.5E_g = 450\text{nm}$) of the QDs. This means that PbSe QD excitations at energies above 450 nm can generate multiple excited states per one photon absorbed. The at both excitation energies, the emission peak of the QDs on glass lies at 1.1 eV.

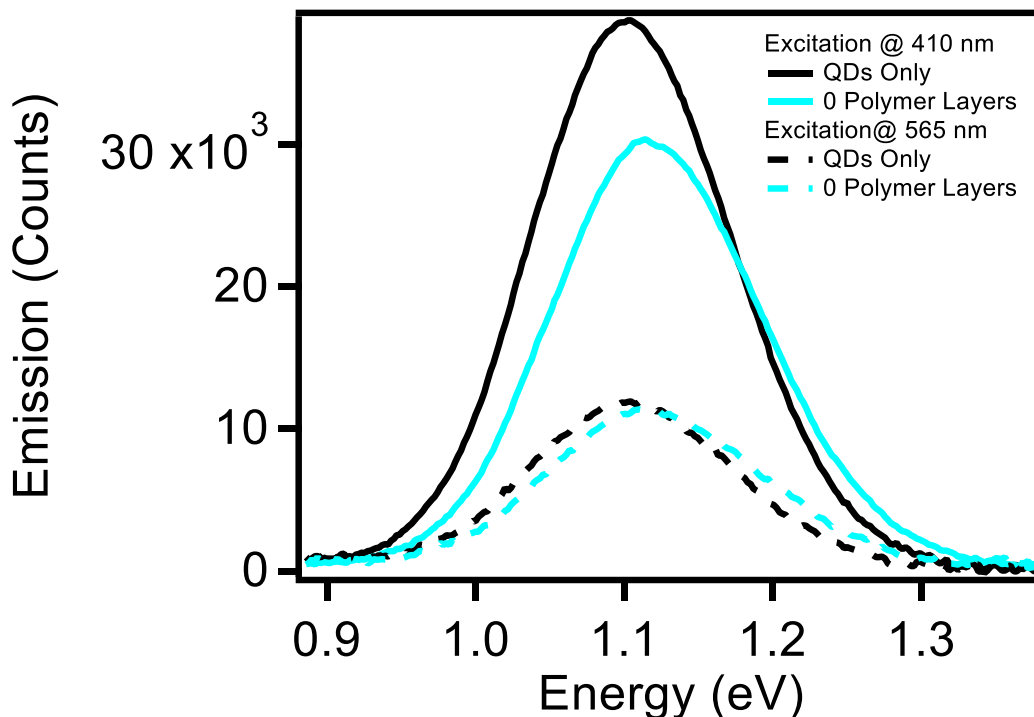


Figure 78: Steady state emission of PbSe QD films in the absence (black) and presence (blue) of Ag NPs. The dashed curves represent the respective PL when excited at energies below the MEG threshold (565 nm), while the solid curves represent the PL when excited at energies above the MEG threshold (410 nm, capable of generating multiple excitons).

Figure 78 shows the steady state PL of PbSe QD films in the absence (black) and presence (blue) of Ag NPs. The dashed curves represent the respective PL when excited at energies below the MEG threshold, while the solid curves represent the PL when excited at energies above the MEG threshold (410 nm). The “0 layer” data means that no spacer layer between the Ag and PbSe QDs was implemented. Right away, it is apparent that the change in dielectric constant caused by the Ag NPs causes a slight blue shift in emission energies (comparing the blue vs black). This means that the strong electric field caused by the Ag NPs SPR is affecting the excitonic transitions in the PbSe QDs. It is important to note that according to the radiating plasmon model, metal enhanced

fluorescence should not occur because there is no overlap between the metal NP SPR and the QD emission.¹⁵¹

Since the QDs absorb more at 410 as compared to 565 nm, one cannot deduce anything about MEG from this data alone. Other optical studies like PLE and time resolved photoluminescence studies were needed to observe absorption enhancement in the QDs.

2.3.6.3 Photoluminescence Excitation Studies

To demonstrate absorption enhancement in these QDs I studied the PbSe PLE spectra with and without the Ag NPs. The scattering of the Ag NPs is strong and would add to the absorbance spectra regardless of QD absorption enhancement. For this reason, we also looked at the presence and intensity of the Ag plasmon peak in the excitation spectrum of the NIR QD emission. The PbSe QD PLE at 1175 nm emission without (black) and with (blue) the presence of Ag NPs is shown in Figure 79. Dark blue to light blue curves represent an increase in polymer spacing.

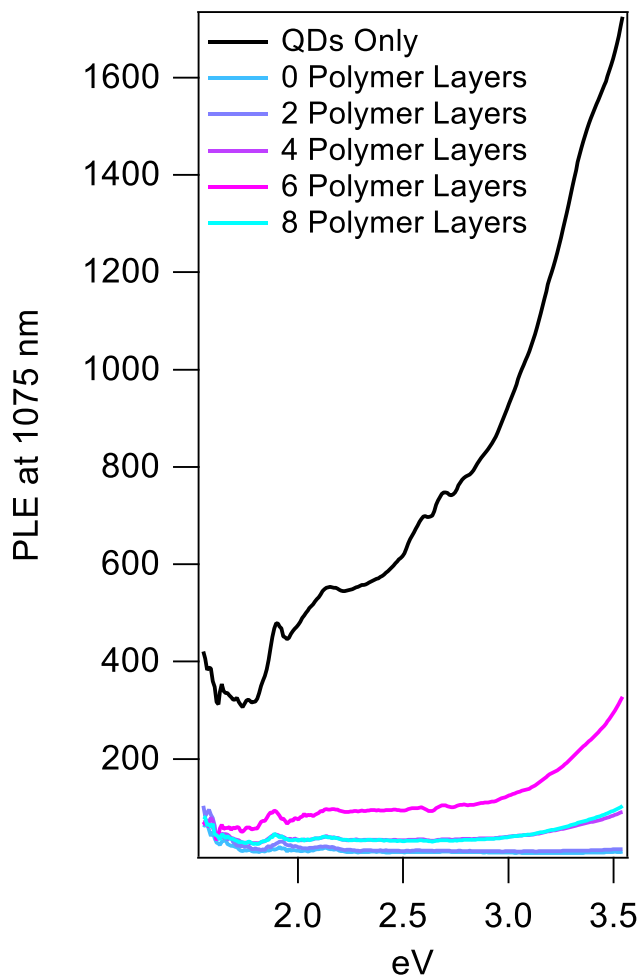


Figure 79: PLE of QD films in the absence (black) and presence (blue) of Ag NPs. The dark blue curve represents an 8-polymer layer QD-NP distance and the light blue curve represents a shorter, 2-polymer layer distance.

Figure 79 shows that no matter the polymer spacing, the QD PLE at 1075 nm is drastically quenched due to the presence of Ag NPs. This may be due to the energy transfer from QD to the metal this also may be due to MEG (which is an extremely fast process). The quenching is to a lesser degree as the QD-NP spacings increase (from dark to light blue). To see the spectral shape differences due to the presence of Ag NPs, I normalized the PLE data to a peak at 1.8 eV (Figure 80). I also plotted the average Ag NP scattering proportion (red) on the right axis to see if there were any similarities present.

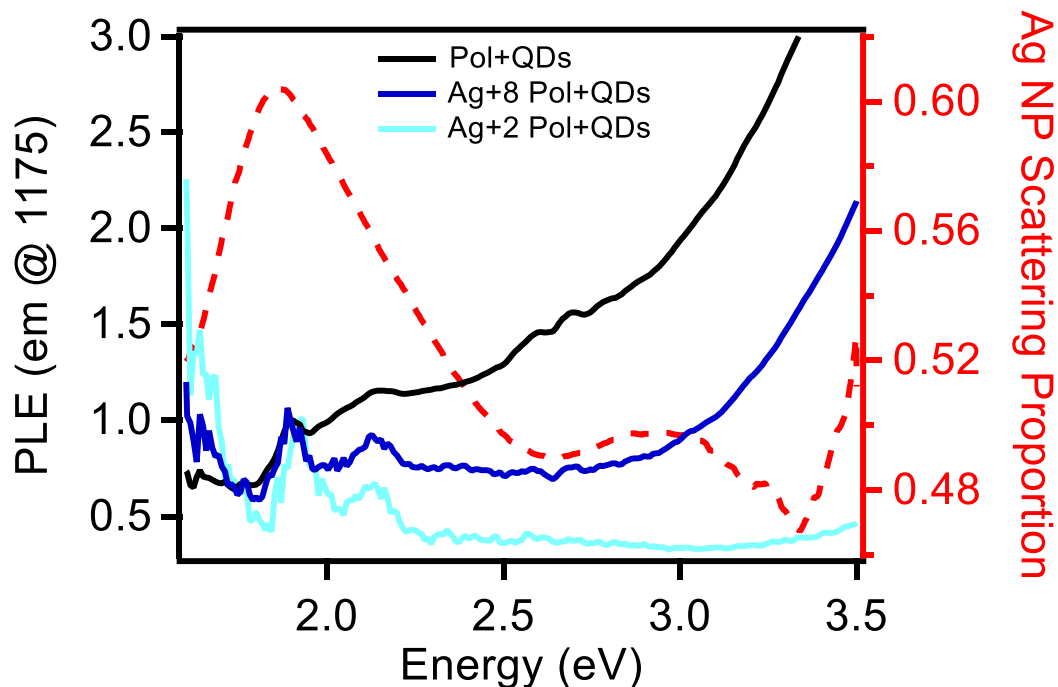


Figure 80: Normalized PLE of QD films in the absence (black) and presence (blue) of Ag NPs. The dark blue curve represents an 8-polymer layer QD-NP distance and the light blue curve represents a shorter, 2-polymer layer distance. The red curve corresponds to the right axis and represents the average Ag NP scattering proportion.

The normalized data in Figure 80 shows that in the presence of NPs (blue curves) compared to without (black) the relative PLE at the scattering proportion maximum (around 2 eV). In this region, the relative QD PLE is greater in the presence compared to other areas of the spectrum. This suggests that although there is quenching/energy transfer into the metal; there is a positive affect on the PLE by the metal in the regions of interest.

To make this effect clearer, the data in the presence of Ag NPs was divided by the data without. To really see how the PLE is changing due to Ag NPs, I performed the calculation below.

$$\text{Average Contribution of Ag NPs to QD PLE} = \frac{\text{Average PLE of QDs with Ag}}{\text{Average PLE of QDs on glass}}$$

I generated Figure 81 to possibly see a correlation of the Average PLE contribution and the Ag film scattering proportion. On the right axis (red), I plotted the average Ag NP scattering proportion for comparison. A signature would prove that the Ag NP film was affecting the emission of the QDs.

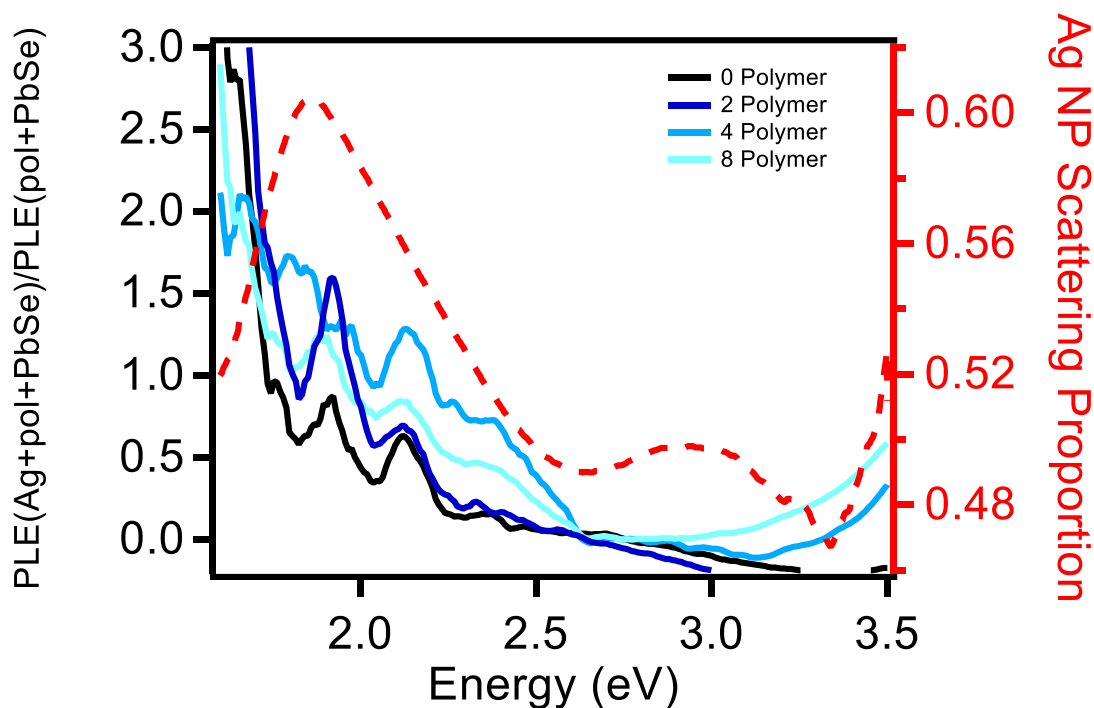


Figure 81: [PLE of QDs with Ag/PLE of QDs alone] The curves from black to light blue represent an increase in Ag-QD spacing. The PLE ratio data were smoothed with a boxcar width of 5 and the background was subtracted for clarity purpose. The red curve corresponds to the right axis and represents the Ag NP scattering proportion.

In each of PLE ratios, there is a slight shoulder from 1.7-2.6 eV. Interestingly, these shoulders appear to correspond to the Ag NP scattering proportion peak at the same energies. This further suggests that there is an absorption enhancement caused by the Ag NP monolayer scattering properties. For completeness, non-averaged PLE data for each polymer thickness (with the same scale) are shown in Figure 82.

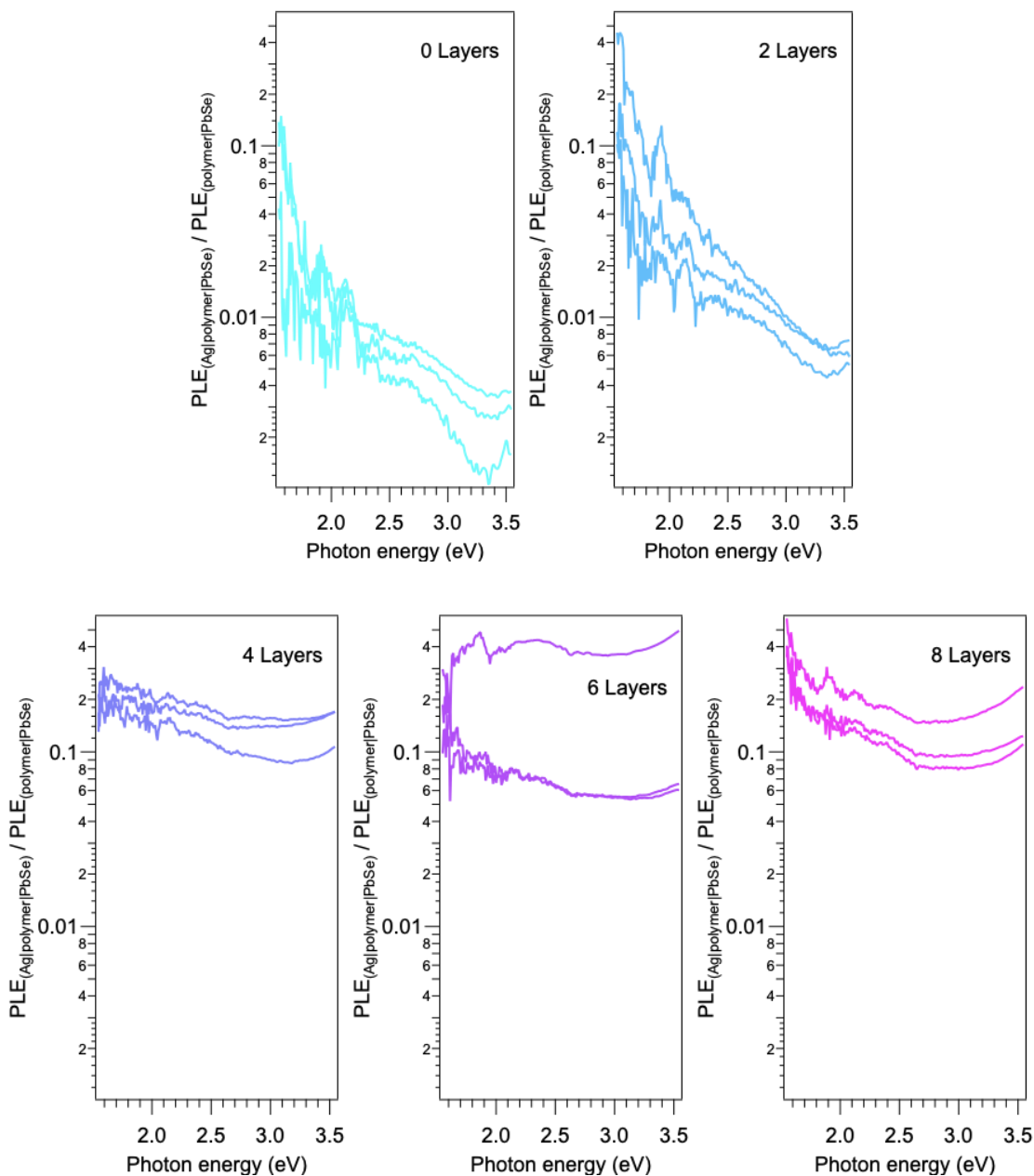


Figure 82: Comparison of PL enhancement versus photon energy (eV) in triplicate of different Ag-QD distances: 0 (light blue), 2 (medium blue), 4 (dark blue), 6 (purple) and 8 layers (pink). Ratio values above 1 would be indicative of enhancement. These values are all less than 1 because the energy transfer from QDs into the metal have not been accounted for.

Figure 82 shows the PLE ratio as the number of polymer layers increase. The 6 polymer layer data set appears to have an outlier with a very large PLE enhancement due

to the Ag NPs. All of the ratios are less than one, so there is no apparent PLE enhancement due to Ag. The enhancement does show a distance dependence, rising at 4, 6, and 8 polymer layers.

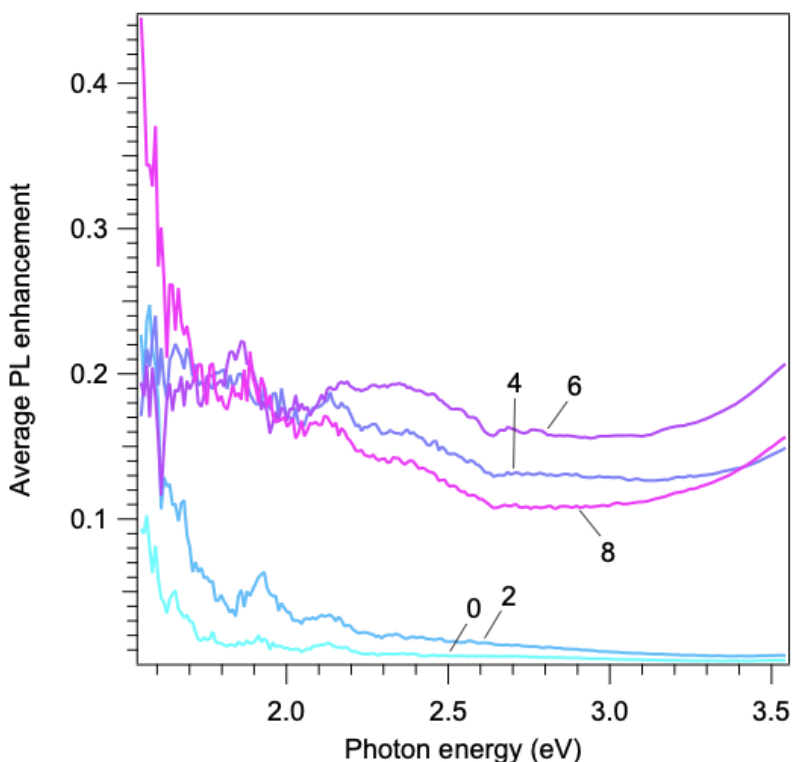


Figure 83: Comparison average PL enhancement averages of different Ag-QD distances: 0 (light blue), 2 (medium blue), 4 (dark blue), 6 (purple) and 8 layers (pink). For clarity, the number of polymer layers are next to the respective curves. Ratio values above 1 would be indicative of enhancement. These values are all less than 1 because the energy transfer from QDs into the metal have not been accounted for.

In general, as the polymer layers increase there is an observed feature that appears in the 1.8-2.5 eV region, which corresponds to the Ag NP scattering proportion. When the Ag NPs are very close to the QDs (0 and 2 layers) the PL enhancement is very low and flat at high energies. Conversely, when the QDs are further from the Ag NPs (4, 6, and 8 layers) there is a rise in PL at high excitation energies. This is very interesting

because this rise begins at around the MEG threshold ($2.5E_g = 2.75$ eV). This rise could be an indication of MEG, but more studies need to be done.

Since the observed PbSe QD PLE quenching due to the Ag NPs suggested energy transfer from the QD to NP, we wanted to look at the excited state dynamics through time resolved photoluminescence studies.

2.3.6.4 Time Resolved Photoluminescence Studies

The charge carrier dynamics of the PbSe QDs are expected to change in the presence of a SPR. In this study, the films were excited by 410 nm light and the emission wavelength probed was 1075 nm. The distance dependence of the fluorescence lifetime is shown in Figure 84.

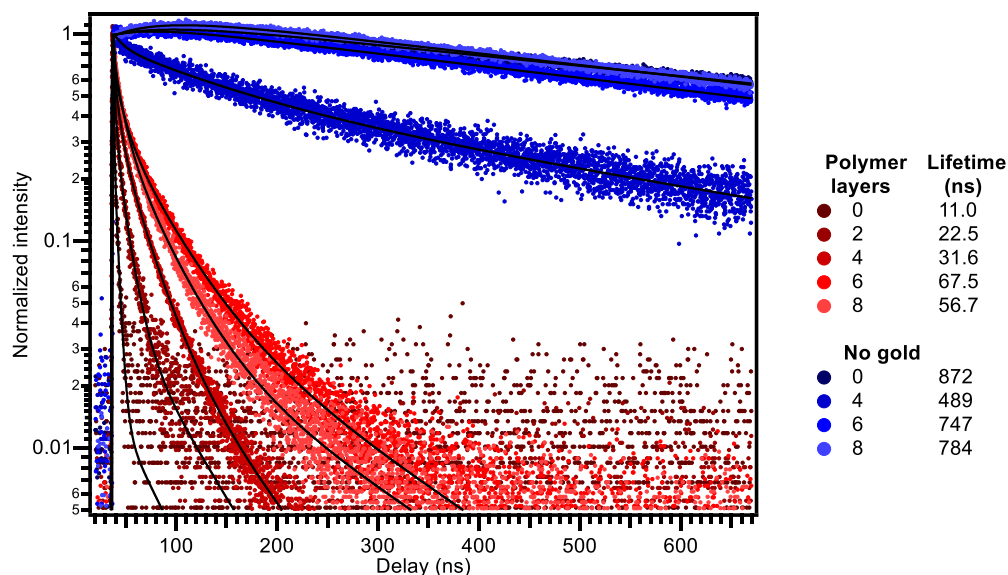


Figure 84: Distance-dependent time resolved photoluminescence decays of NP-QD films. The blue curves represent the lifetimes of PbSe QDs on polymer alone, and the red curves represent different polymer spacings between QD and NP. The shortness of lifetime with increasing proximity from QD-NP corresponds to more energy transfer into the metal.

When no NPs are present (blue curve), the decay is very long (around 800 ns) and appears close to monoexponential. As the QDs get closer to the metal NP (from light pink

to dark red), the lifetime shortens drastically and begins to appear multiexponential. This provides further evidence that the QD and NP are coupled to a greater degree as they get closer in proximity. The shortness of lifetime may be a result of the energy transfer to the NP. The plasmons then cannot radiate that energy due to wave vector mismatching at the monolayer interface, so the energy is then lost as heat.¹⁵¹ To explore this trend further, Figure 85 shows the lifetimes (sec) versus polymer layers.

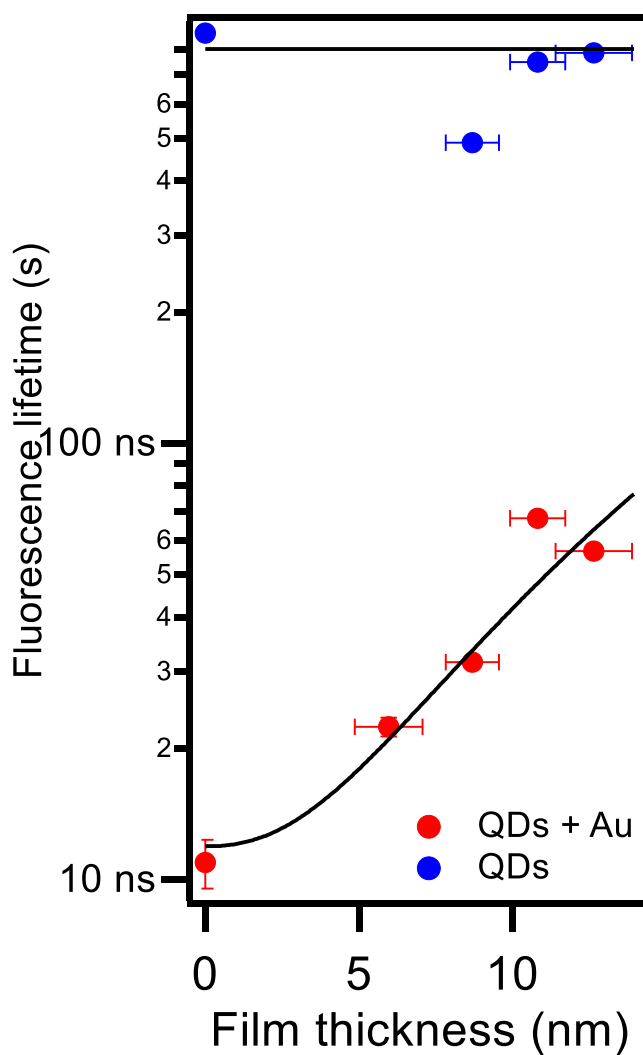


Figure 85: Fluorescence lifetime of QDs versus distance between NP and QD (red) and QDs alone (blue). The shortness of lifetime with increasing proximity from QD-NP corresponds to more energy transfer into the metal.

The lifetime trend appears to exponential increase as the polymer spacer increases. It should be noted that the y axis is on a logarithmic scale. The closer the QD is to the plasmon, the easier that the plasmon can couple into non-radiative pathways of the QDs. This shortness of lifetime can possibly result in longer lasting films due to less chances for photooxidation to occur.

2.3.7 Excitation Enhancement Calculations

An important goal of this work was to show that silver NP films induce an excitation enhancement into the PbSe QDs. The problem is, we have relied on the photoluminescence excitation (PLE) data to monitor this enhancement. This is a problem because the photoluminescence (PL) yield drops as the particles get close to the Ag NPs due to energy transfer into the Ag films. So, in order to estimate absorption enhancement, we corrected the PL intensities for distance-dependent non-radiative losses. We did this by measuring the PL lifetimes as a function of the distance between NPs and QDs (section 2.3.6.4).

In the absence of the metals, the PL quantum yield, ϕ , is given by:

$$\phi_{QD} = \frac{k_r}{k_r + k_{nr}}$$

Where k_r and k_{nr} are the radiative and non-radiative exciton recombination rates. When the QDs are near silver, an additional non-radiative decay channel, k_{Ag} , appears. The PL quantum yield is now given by:

$$\phi_{QD+Ag} = \frac{k_r}{k_r + k_{nr} + k_{Ag}}$$

The quantum dot emission rates, k_{QD} and k_{QD+Ag} are given by:

$$k_{QD} = k_r + k_{nr}$$

$$k_{QD+Ag} = k_r + k_{nr} + k_{Ag}$$

So, the quantum yields in the presence and absence of Ag NPs can be rewritten as:

$$\phi_{QD} = \frac{k_r}{k_{QD}}$$

$$\phi_{QD+Ag} = \frac{k_r}{k_{QD+Ag}}$$

The ratio of emission intensities, I_{QD+Ag}/I_{QD} measured with and without Ag NPs is given by the quantum yield ratios

$$\frac{I_{QD+Ag}}{I_{QD}} = \frac{\phi_{QD+Ag}}{\phi_{QD}} = \frac{\frac{k_r}{k_{QD+Ag}}}{\frac{k_r}{k_{QD}}} = \frac{k_{QD}}{k_{QD+Ag}}$$

The following equation is expressing the ratio of emission intensities in terms of PL lifetimes:

$$\frac{I_{QD+Ag}}{I_{QD}} = \frac{\tau_{QD+Ag}}{\tau_{QD}}$$

So, we can write a lifetime-normalized PL ratio, R , which we equate to the excitation enhancement:

$$R = \frac{I_{QD+Ag}}{I_{QD}} \frac{\tau_{QD}}{\tau_{QD+Ag}}$$

If there is no excitation enhancement then $R = 1$, but if $R > 1$ then the Ag NPs cause increased photoabsorption in the PbSe QDs.

Figure 86 shows the calculated excitation enhancement vs energy of 0 (light blue), 2 (blue), 4 (dark blue), 6 (purple) and 8 (pink) layers of polymer between QD and NP. If there is no excitation enhancement, the value for excitation enhancement is 1. If the value on the y-axis is greater than one, then there is an absorption enhancement caused by the presence of Ag NPs. Each curve shows at least some excitation enhancement (least of all when the Ag NPs are close to the QDs.)

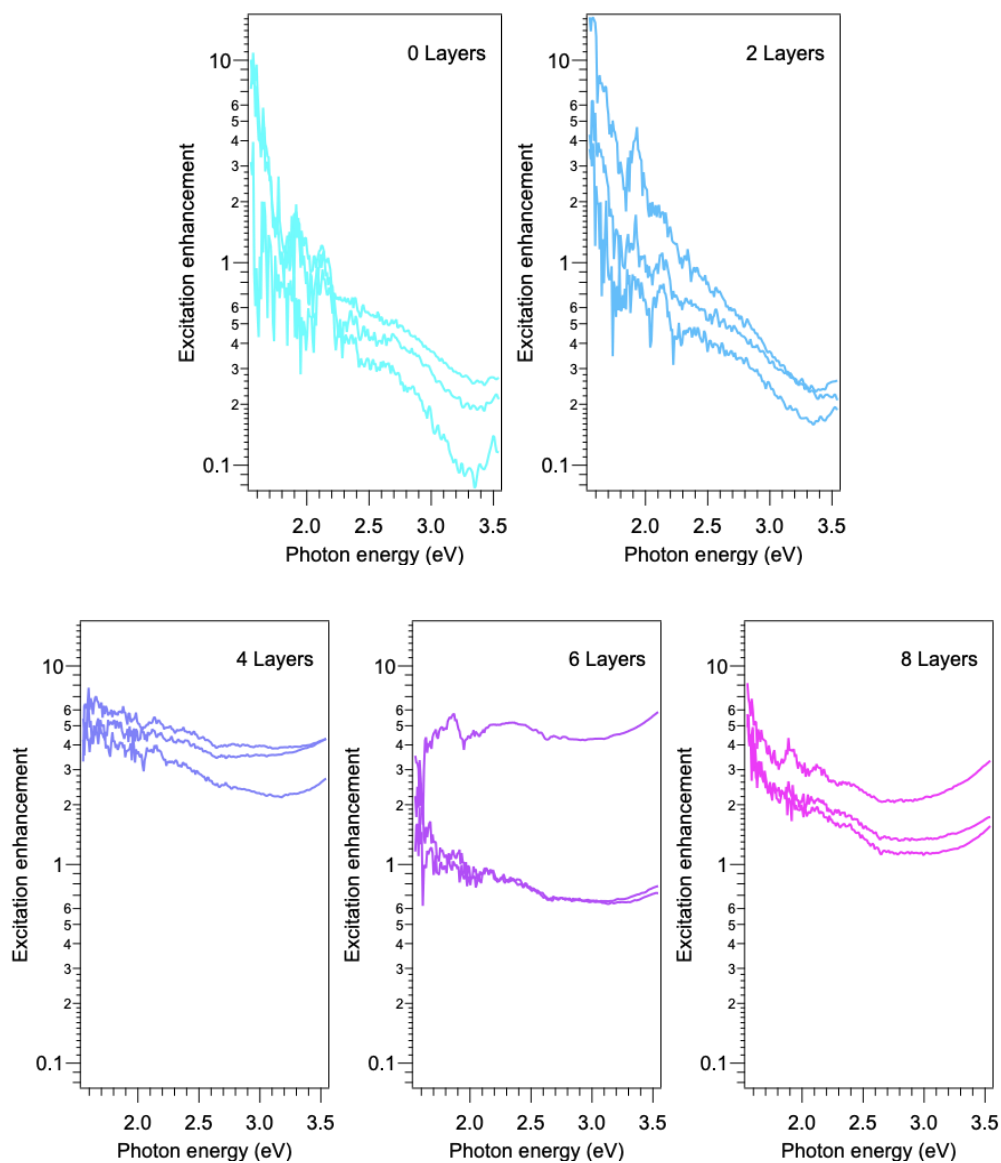


Figure 86: Calculated excitation enhancement vs energy of 0 (light blue), 2 (blue), 4 (dark blue), 6 (purple) and 8 (pink) layers of polymer between QD and NP. If there is no excitation enhancement, the value for excitation enhancement is 1. If the value on the y-axis is greater than one, then there is an absorption enhancement caused by the presence of Ag NPs.

The MEG threshold for the QDs is 2.75 eV. It is interesting that around that energy and above (in the 4, 6, and 8 layer spacing cases), a slight rise in excitation enhancement is observed. The same trend was observed in the PL enhancement. Figure

87 shows the same data, but each thickness was averaged on the same plot for comparison. For clarity, the number of polymer layers is next to each respective curve.

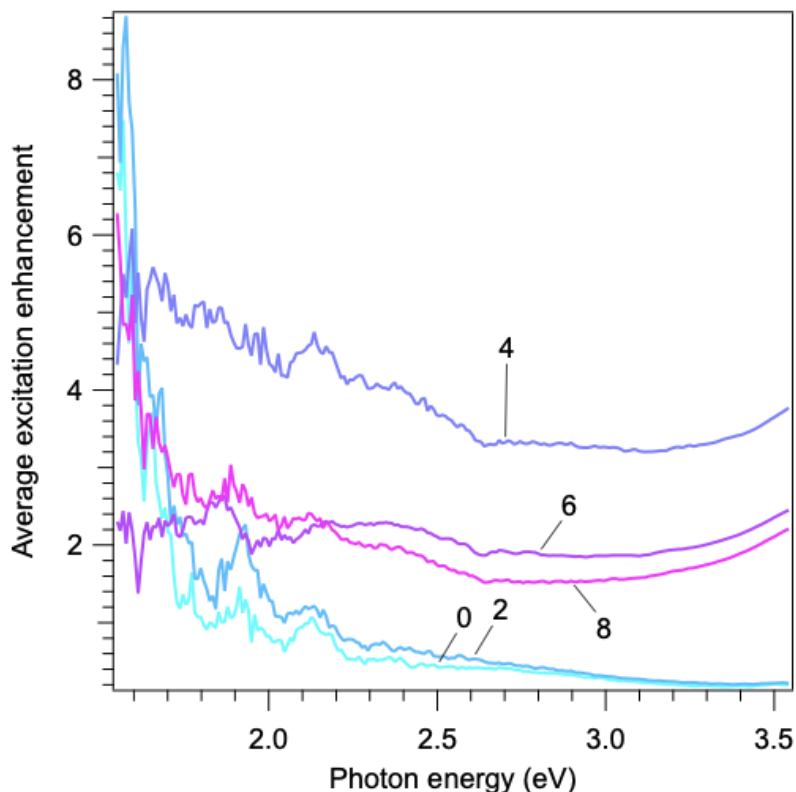


Figure 87: Calculated average excitation enhancement vs energy of 0 (light blue), 2 (blue), 4 (dark blue), 6 (purple) and 8 (pink) layers of polymer between QD and NP. For clarity, the number of polymer layers is next to each respective curve. If there is no excitation enhancement, the value for excitation enhancement is 1. If the value on the y-axis is greater than one, then there is an absorption enhancement caused by the presence of Ag NPs.

Figure 87 shows that when the spacings between the Ag and NP are above 4, there is a broadband excitation enhancement in the QDs. It is important to note that in these curves (pink, purple, and blue) there is a drastic rise in enhancement at excitation energies above the MEG threshold of the QDs (2.75 eV).

These results agree with the theoretical work of Lee et. al. on the origin of enhanced optical absorption in solar cells.¹⁷⁷ They found that the enhancement arose from

the metal NP scattering and the enhanced optical fields caused from the SPR. Just like we observed experimentally, their work predicted absorption enhancement at wavelengths over a broad optical range, longer than the SPR wavelengths, due to the absorption of light scattered by the NPs.¹⁷⁷ More recent work has also found that metal NPs enhance absorption at long wavelengths due to the increased electromagnetic field and the scattering by the metal NPs.¹⁷⁸

The same data is shown in a different way to highlight and compare the absorption enhancement at different polymer thicknesses and excitation energies in Figure 88. This shows the excitation enhancement values versus film thickness (nm). The enhancement values were taken at different excitation energies: 2.0 eV (red), 2.5 eV (yellow), 3.0 eV (green), and 3.5 eV (blue).

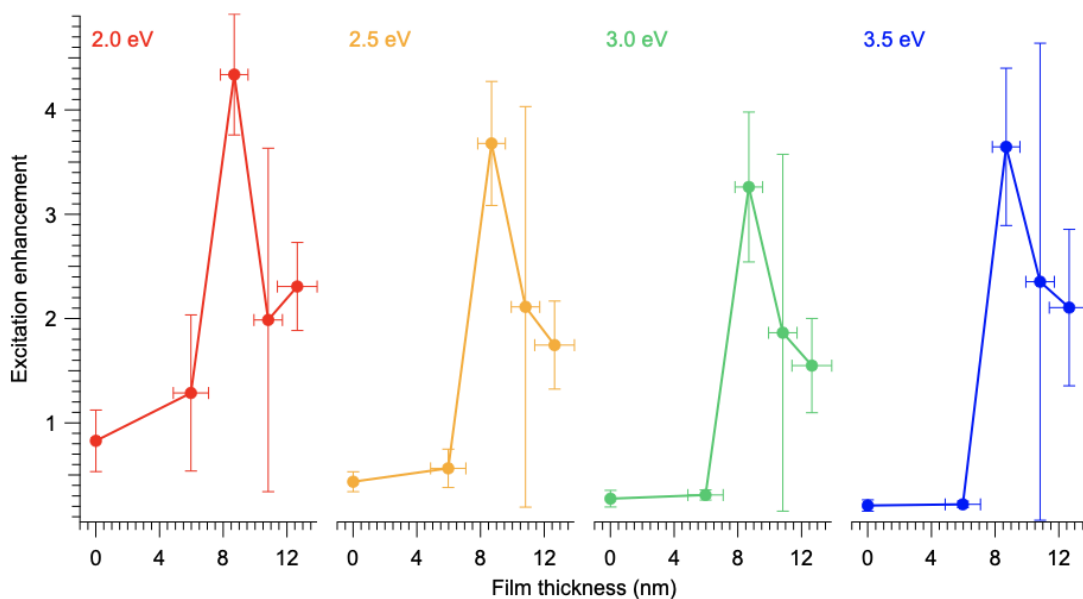


Figure 88: Excitation enhancement values versus film thickness (nm). The enhancement values were taken at different excitation energies: 2.0 eV (red), 2.5 eV (yellow), 3.0 eV (green), and 3.5 eV (blue). The MEG threshold for the QDs is around 2.75 eV.

Figure 88 shows that the excitation enhancement has a distance and frequency dependence. At all excitation energies, the greatest excitation enhancement was observed when the Ag NPs were 6 polymer spacings, or approximately 8 nm away from the QDs. This optimal QD-NP thickness agrees with Tobias et. al. where they looked at metal enhanced fluorescence in CdSe QDs.¹⁷⁹ The first two points in each plot flatten out. This may be because the scattering proportion of the QDs with 2 polymer layers scatters best in the red, not the blue. This is not surprising because near field coupling enhancement is notoriously distance dependent.

It is also very interesting that from the green curve to blue (excitation energies at 3-3.5 eV) there is an increase in excitation enhancement at polymer thicknesses greater than 2. This could possibly be due to MEG. Though MEG happens very quickly in QDs alone, Sharonda LeBlanc et. al. found that they could measure biexciton emission in CdSe QDs coupled to Ag films.¹⁵⁹

CHAPTER 2.4 SUMMARY/CONCLUSIONS

We are interested in the development of novel, more efficient, cheaper, and thinner solar devices than the current state-of-the-art. The advantages and disadvantages of the latest solar energy technologies have been highlighted. Lead-based QDs have specific properties and potential for efficiency improvements in solar cells such as MEG. To increase the quantum yield, long term stability, and charge separation in these QDs; we will implement a synthetic approach to yield highly passivated QDs by chlorine and cadmium.

Instead of trying to improve the efficiency of MEG, we wanted to find a way to maximize the utility of MEG by increasing the amount of light absorption above the MEG threshold. We were able to achieve this by placing surface plasmons in metal nanoparticles near our QDs. Our scattering, absorption, photoluminescence excitation and lifetime data supported that we increase the light absorption above the MEG threshold in the lead-based semiconductors. We were able to achieve this by using the light concentration and scattering abilities of surface plasmon resonances in colloidal silver nanoparticles.

This research will add to our understanding of interactions between metal SPRs and QD excitons. If we could develop a way to enhance the absorption rates of the QDs above the MEG threshold then this project could also act as a stepping-stone to more efficient solar cells. Furthermore, exciton-plasmon coupling could be a general strategy for increasing absorption rates in solar cells, enabling thinner (and cheaper) devices. This

research is important for the development of low cost, high efficiency solar cells in addition to a wide range of optoelectronic applications.

CHAPTER 2.5 FUTURE WORK

Future directions of this research can involve different metals for the SPR (like higher energy Ag NPs) and even different shapes of the metal SPR. Metallic nanorods have longitudinal and transverse modes that we can possibly use to push more light at the direct band edge and above the MEG threshold, simultaneously! Specific experiments that could directly support our work include the measurement of biexciton lifetimes.

2.5.1 Measure Biexciton Lifetimes

In order to learn about the effects of SPRs on MEG in PbSe QDs, time-resolved fluorescence at the single particle and ensemble level should be recorded. Then, we can distinguish biexciton PL using photon-correlation spectroscopy for single particles and multi-pulse time resolved PL (developed in the Jones group) for ensemble samples.

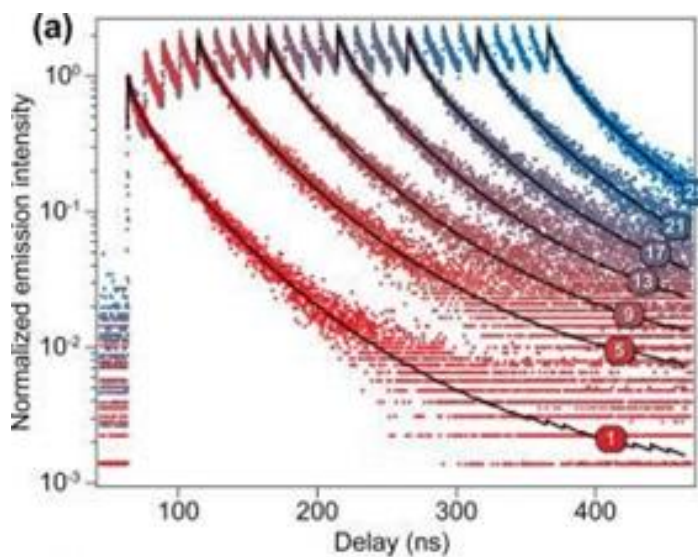


Figure 89: An example of multi pulse time-resolved fluorescence decays (CdSe QDs).¹⁸⁰ Reprinted (adapted) with permission from (Singh, G.; Guericke, M. A.; Song, Q.; Jones, M., A Multipulse Time-Resolved Fluorescence Method for Probing Second-Order Recombination Dynamics in Colloidal Quantum Dots. *Journal of Physical Chemistry C* 2014, 118 (26), 14692-14702.). Copyright (2014) American Chemical Society.

This multi-pulse technique (Figure 89) allows us to selectively resolve and characterize PL from multiply excited states in ensemble QD samples.¹⁸⁰ Analyzing the data built up from the multipulse time resolved PL can be used to model processes like QD charging. This specific technique operates on the 80 GHz laser pulses, which are 12 ns apart.

Unfortunately, that means any process that happens within this time period cannot be probed. By shortening and controlling the time between two pulses using a mechanical delay line on the laser table, we can perform two-pulse TRPL experiments.

Two-Pulse time resolved photoluminescence lifetimes

We can perform 2-pulse lifetime experiments to pump and probe the samples much like transient absorption. After the laser light comes through the second modulator, it is split into two paths using a beam splitter. One path goes to the sample, while the other goes through an electronically controlled delay stage.

By varying the time between pulses, we can look for a biexciton decay signature in the TRPL and eventually model biexciton lifetimes. The Jones laser table is already set up and aligned for this 2-pulse experiment with a beam splitter, two paths, and a delay line.

Once the biexciton lifetimes are modeled within our samples, we can observe any differences, or enhancements of biexciton lifetimes caused by the presence of the Ag SPR. Eventually with this technique, we may be able to answer questions like: How does the excited state (exciton, biexciton, trion, etc) on QD affect coupling strength?

These spectroscopic experiments will allow us to determine if we can use the SPR of Ag to act as an antenna to push more light above the MEG threshold in near IR absorbing PbX QDs.

REFERENCES

1. Donega, C. D., Synthesis and properties of colloidal heteronanocrystals. *Chemical Society Reviews* **2011**, *40* (3), 1512-1546.
2. Ellingson, R. J.; Beard, M. C.; Johnson, J. C.; Yu, P. R.; Micic, O. I.; Nozik, A. J.; Shabaev, A.; Efros, A. L., Highly efficient multiple exciton generation in colloidal PbSe and PbS quantum dots. *Nano Letters* **2005**, *5* (5), 865-871.
3. Moreels, I.; Lambert, K.; Smeets, D.; De Muynck, D.; Nollet, T.; Martins, J. C.; Vanhaecke, F.; Vantomme, A.; Delerue, C.; Allan, G.; Hens, Z., Size-Dependent Optical Properties of Colloidal PbS Quantum Dots. *Acs Nano* **2009**, *3* (10), 3023-3030.
4. Kelly, K. L.; Coronado, E.; Zhao, L. L.; Schatz, G. C., The optical properties of metal nanoparticles: The influence of size, shape, and dielectric environment. *Journal of Physical Chemistry B* **2003**, *107* (3), 668-677.
5. Lewis, N. S., Toward cost-effective solar energy use. *Science* **2007**, *315* (5813), 798-801.
6. Hussein, A. K., Applications of nanotechnology in renewable energies-A comprehensive overview and understanding. *Renewable & Sustainable Energy Reviews* **2015**, *42*, 460-476.
7. SEIA Solar Industry Data. <http://www.seia.org/research-resources/solar-industry-data>.
8. Green, M. A.; Hishikawa, Y.; Dunlop, E. D.; Levi, D. H.; Hohl-Ebinger, J.; Yoshita, M.; Ho-Baillie, A. W. Y., Solar cell efficiency tables (Version 53). *Progress in Photovoltaics* **2019**, *27* (1), 3-12.
9. Atwater, H. A.; Polman, A., Plasmonics for improved photovoltaic devices. *Nature Materials* **2010**, *9* (3), 205-213.

10. Imamura, K.; Nonaka, T.; Onitsuka, Y.; Irishika, D.; Kobayashi, H., Light trapping of crystalline Si solar cells by use of nanocrystalline Si layer plus pyramidal texture. *Applied Surface Science* **2017**, *395*, 50-55.
11. Hu, F. Q.; Sun, Y.; Zha, J. W.; Chen, K. X.; Zou, S.; Fang, L.; Su, X. D., Pre-texturing multi-crystalline silicon wafer via a two-step alkali etching method to achieve efficient nanostructured solar cells. *Solar Energy Materials and Solar Cells* **2017**, *159*, 121-127.
12. El-Amin, A. A., Use of Etching to Improve Efficiency of the Multicrystalline Silicon Solar Cell by Using an Acidic Solution. *Silicon* **2017**, *9* (1), 39-45.
13. Wu, L.; Zhang, H. M.; Qin, F. F.; Bai, X. G.; Ji, Z. Y.; Huang, D., Performance enhancement of pc-Si solar cells through combination of anti-reflection and light-trapping: Functions of AAO nano-grating. *Optics Communications* **2017**, *385*, 205-212.
14. Es, F.; Baytemir, G.; Kulakci, M.; Turan, R., Metal-assisted nano-textured solar cells with SiO₂/Si₃N₄ passivation. *Solar Energy Materials and Solar Cells* **2017**, *160*, 269-274.
15. Al-Taay, H. F.; Mahdi, M. A.; Parlevliet, D.; Jennings, P., Fabrication and Characterization of Solar Cells Based on Silicon Nanowire Homo Junctions. *Silicon* **2017**, *9* (1), 17-23.
16. Shahraki, M.; Salehi, M. R.; Abiri, E., Omnidirectional broadband absorption enhancement in laterally assembled quadrangle silicon nanowire solar cells. *Journal of Modern Optics* **2017**, *64* (1), 23-31.
17. Xu, Z. P.; Huangfu, H. C.; He, L.; Wang, J. Z.; Yang, D.; Guo, J. W.; Wang, H. Y., Light-trapping properties of the Si inclined nanowire arrays. *Optics Communications* **2017**, *382*, 332-336.

18. Badar, M. S.; Saleem, M. R., Improved absorption efficiency of silicon (Si) solar cells through Resonant Waveguide Gratings (RWGs) - A hybrid design of RWG and Si solar cell. *Optik* **2017**, *128*, 50-56.

19. Xing, Y. P.; Zhang, K. L.; Zhao, J. S.; Han, P. D.; Yang, Z. C.; Yuan, Y. J.; Ding, Q., Antireflection and absorption properties of silicon parabolic-shaped nanocone arrays. *Optik* **2017**, *128*, 133-138.

20. Gammoudi, H.; Belkhiria, F.; Helali, S.; Ben Assaker, I.; Gammoudi, I.; Morote, F.; Souissi, A.; Karyouli, M.; Amlouk, M.; Cohen-Bouhacina, T.; Chtourou, R., Chemically grafted of single-walled carbon nanotubes onto a functionalized silicon surface. *Journal of Alloys and Compounds* **2017**, *694*, 1036-1044.

21. Stegemann, B.; Gad, K. M.; Balamou, P.; Sixtensson, D.; Vossing, D.; Kasemann, M.; Angermann, H., Ultra-thin silicon oxide layers on crystalline silicon wafers: Comparison of advanced oxidation techniques with respect to chemically abrupt SiO₂/Si interfaces with low defect densities. *Applied Surface Science* **2017**, *395*, 78-85.

22. Matsumoto, T.; Nakajima, H.; Irishika, D.; Nonaka, T.; Imamura, K.; Kobayashi, H., Ultrathin SiO₂ layer formed by the nitric acid oxidation of Si (NAOS) method to improve the thermal-SiO₂/Si interface for crystalline Si solar cells. *Applied Surface Science* **2017**, *395*, 56-60.

23. Collavini, S.; Volker, S. F.; Delgado, J. L., eUnderstanding the Outstanding Power Conversion Efficiency of Perovskite-Based Solar Cells. *Angewandte Chemie-International Edition* **2015**, *54* (34), 9757-9759.

24. Burschka, J.; Pellet, N.; Moon, S. J.; Humphry-Baker, R.; Gao, P.; Nazeeruddin, M. K.; Gratzel, M., Sequential deposition as a route to high-performance perovskite-sensitized solar cells. *Nature* **2013**, *499* (7458), 316-+.

25. Stranks, S. D.; Eperon, G. E.; Grancini, G.; Menelaou, C.; Alcocer, M. J. P.; Leijtens, T.; Herz, L. M.; Petrozza, A.; Snaith, H. J., Electron-Hole Diffusion Lengths Exceeding 1 Micrometer in an Organometal Trihalide Perovskite Absorber. *Science* **2013**, *342* (6156), 341-344.

26. Zhou, H. P.; Chen, Q.; Li, G.; Luo, S.; Song, T. B.; Duan, H. S.; Hong, Z. R.; You, J. B.; Liu, Y. S.; Yang, Y., Interface engineering of highly efficient perovskite solar cells. *Science* **2014**, *345* (6196), 542-546.
27. Zheng, H. G.; Dai, J., Temperature-dependent photoluminescence properties of HC(NH₂)₂ PbI₃ perovskite nanorods. *Materials Letters* **2017**, *188*, 232-234.
28. Kim, S.; Chung, T.; Bae, S.; Lee, S. W.; Lee, K. D.; Kim, H.; Lee, S.; Kang, Y.; Lee, H. S.; Kim, D., Improved performance and thermal stability of perovskite solar cells prepared via a modified sequential deposition process. *Organic Electronics* **2017**, *41*, 266-273.
29. Wang, P.; Zhao, J. J.; Liu, J. X.; Wei, L. Y.; Liu, Z. H.; Guan, L. H.; Cao, G. Z., Stabilization of organometal halide perovskite films by SnO₂ coating with inactive surface hydroxyl groups on ZnO nanorods. *Journal of Power Sources* **2017**, *339*, 51-60.
30. Lu, J. J.; Wan, M. X.; Wen, P.; Luo, F.; Liu, X.; Wen, J.; Hu, C. Y.; Guo, J., Investigation on the high pressure annealing induced re crystallization mechanism of CH₃NH₃PbI₃ film. *Journal of Alloys and Compounds* **2017**, *694*, 1365-1370.
31. Yuan, J. L.; Li, B.; Hao, C. J., Study on cobalt doped tin based perovskite material with enhanced air stability. *Materials Science in Semiconductor Processing* **2017**, *57*, 95-98.
32. Huang, X.; Guo, H.; Wang, K.; Liu, X. B., Ionic liquid induced surface trap-state passivation for efficient perovskite hybrid solar cells. *Organic Electronics* **2017**, *41*, 42-48.
33. Zou, Y.; Meng, Q.; Mao, H. Y.; Zhu, D. B., Substrate effect on the interfacial electronic structure of thermally-evaporated CH₃NH₃PbI₃ perovskite layer. *Organic Electronics* **2017**, *41*, 307-314.
34. Zhang, S. F.; Zhang, C. M.; Bi, E. B.; Miao, X. L.; Zeng, H. B.; Han, L. Y., Organic-inorganic halide perovskite solar cell with CH₃NH₃PbI₂Br as hole conductor. *Journal of Power Sources* **2017**, *339*, 61-67.

35. Zhang, F.; Zhao, X. M.; Yi, C. Y.; Bi, D. Q.; Bi, X. D.; Wei, P.; Liu, X. C.; Wang, S. R.; Li, X. G.; Zakeeruddin, S. M.; Gratzel, M., Dopant-free star-shaped hole-transport materials for efficient and stable perovskite solar cells. *Dyes and Pigments* **2017**, *136*, 273-277.
36. Choi, H.; Heo, J. H.; Ha, S.; Kwon, B. W.; Yoon, S. P.; Han, J.; Kim, W. S.; Im, S. H.; Kim, J., Facile scalable synthesis of MoO₂ nanoparticles by new solvothermal cracking process and their application to hole transporting layer for CH₃NH₃PbI₃ planar perovskite solar cells. *Chemical Engineering Journal* **2017**, *310*, 179-186.
37. Dai, S. M.; Tian, H. R.; Zhang, M. L.; Xing, Z.; Wang, L. Y.; Wang, X.; Wang, T.; Deng, L. L.; Xie, S. Y.; Huang, R. B.; Zheng, L. S., Pristine fullerenes mixed by vacuum-free solution process: Efficient electron transport layer for planar perovskite solar cells. *Journal of Power Sources* **2017**, *339*, 27-32.
38. Okamoto, Y.; Fukui, R.; Fukazawa, M.; Suzuki, Y., SrTiO₃/TiO₂ composite electron transport layer for perovskite solar cells. *Materials Letters* **2017**, *187*, 111-113.
39. Ji, G. W.; Zhao, B.; Song, F.; Zheng, G. H. J.; Zhang, X. N.; Shen, K. C.; Yang, Y. G.; Chen, S.; Gao, X. Y., The energy level alignment at the CH₃NH₃PbI₃/pentacene interface. *Applied Surface Science* **2017**, *393*, 417-421.
40. Brinkmann, K. O.; Zhao, J.; Pourdavoud, N.; Becker, T.; Hu, T.; Olthof, S.; Meerholz, K.; Hoffmann, L.; Gahlmann, T.; Heiderhoff, R.; Oszajca, M. F.; Luechinger, N. A.; Rogalla, D.; Chen, Y.; Cheng, B.; Riedl, T., Suppressed decomposition of organometal halide perovskites by impermeable electron-extraction layers in inverted solar cells. *Nature Communications* **2017**, *8*.
41. Zhang, Q. H.; Hu, W. D.; Wang, X. F.; Chen, G.; Zhang, J. P.; Xiao, L. X.; Miyasaka, T., Fullerene Multiadducts as Electron Collection Layers for Perovskite Solar Cells. *Chemistry Letters* **2017**, *46* (1), 101-103.
42. New tandem perovskite solar cell could outrank silicon's efficiency and stability. *American Ceramic Society Bulletin* **2017**, *96* (1), 18-18.

43. Hadrich, M.; Kraft, C.; Loffler, C.; Metzner, H.; Reislohner, U.; Witthuhn, W., Pathways to thin absorbers in CdTe solar cells. *Thin Solid Films* **2009**, *517* (7), 2282-2285.
44. Bosio, A.; Romeo, N.; Mazzamuto, S.; Canevari, V., Polycrystalline CdTe thin films for photovoltaic applications. *Progress in Crystal Growth and Characterization of Materials* **2006**, *52* (4), 247-279.
45. Ferekides, C. S.; Balasubramanian, U.; Mamazza, R.; Viswanathan, V.; Zhao, H.; Morel, D. L., CdTe thin film solar cells: device and technology issues. *Solar Energy* **2004**, *77* (6), 823-830.
46. Beach, J. D.; McCandless, B. E., Materials challenges for CdTe and CuInSe₂ photovoltaics. *Mrs Bulletin* **2007**, *32* (3), 225-229.
47. Amin, N.; Isaka, T.; Okamoto, T.; Yamada, A.; Konagai, M., Prospects of thickness reduction of the CdTe layer in highly efficient CdTe solar cells towards 1 μm. *Japanese Journal of Applied Physics Part 1-Regular Papers Short Notes & Review Papers* **1999**, *38* (8), 4666-4672.
48. Compaan, A. D.; Gupta, A.; Lee, S. Y.; Wang, S. L.; Drayton, J., High efficiency, magnetron sputtered CdS/CdTe solar cells. *Solar Energy* **2004**, *77* (6), 815-822.
49. Versluys, J.; Clauws, P.; Nollet, P.; Degrave, S.; Burgelman, M., DLTS and admittance measurements on CdS/CdTe solar cells. *Thin Solid Films* **2003**, *431*, 148-152.
50. Uda, H.; Ikegami, S.; Sonomura, H., Properties of CdS/CdTe solar cells with Cu₂Te-Au contacts. *Japanese Journal of Applied Physics Part 1-Regular Papers Short Notes & Review Papers* **1997**, *36* (9A), 5549-5550.
51. Pena, J. L.; Riech, I.; Rejon, V.; Ieee, Study of CdS/CdTe solar cells activated with N-O-2-CHClF₂ gas mixture. *2014 Ieee 40th Photovoltaic Specialist Conference (Pvsc)* **2014**, 1679-1681.

52. Lv, B.; Huang, L.; Fu, M.; Zhang, F. M.; Wu, X. S., Effects of oxidation and CdCl₂ treatment on the electronic properties of CdTe polycrystalline films. *Materials Chemistry and Physics* **2015**, *165*, 49-54.
53. Wada, T.; Hashimoto, Y.; Nishiwaki, S.; Satoh, T.; Hayashi, S.; Negami, T.; Miyake, H., High-efficiency CIGS solar cells with modified CIGS surface. *Solar Energy Materials and Solar Cells* **2001**, *67* (1-4), 305-310.
54. Bhattacharya, R. N.; Oh, M. K.; Kim, Y., CIGS-based solar cells prepared from electrodeposited precursor films. *Solar Energy Materials and Solar Cells* **2012**, *98*, 198-202.
55. Elbar, M.; Tobbeche, S.; Merazga, A., Effect of top-cell CGS thickness on the performance of CGS/CIGS tandem solar cell. *Solar Energy* **2015**, *122*, 104-112.
56. Versluys, J.; Clauws, R.; Nollet, P.; Degrave, S.; Burgelman, M., Characterization of deep defects in CdS/CdTe thin film solar cells using deep level transient spectroscopy. *Thin Solid Films* **2004**, *451*, 434-438.
57. Limmanee, A.; Songtraï, S.; Udomdachanut, N.; Kaewniyompanit, S.; Sato, Y.; Nakaishi, M.; Kittisontirak, S.; Sriprapha, K.; Sakamoto, Y., Degradation analysis of photovoltaic modules under tropical climatic conditions and its impacts on LCOE. *Renewable Energy* **2017**, *102*, 199-204.
58. Gour, K. S.; Singh, O. P.; Bhattacharyya, B.; Parmar, R.; Husale, S.; Senguttuvan, T. D.; Singh, V. N., Enhanced photoresponse of Cu₂ZnSn(S, Se)₄ based photodetector in visible range. *Journal of Alloys and Compounds* **2017**, *694*, 119-123.
59. Elisa, M.; Iordanescu, C. R.; Vasiliu, I. C.; Feraru, I. D.; Epurescu, G.; Filipescu, M.; Plapcianu, C.; Bartha, C.; Trusca, R.; Peretz, S., Synthesis and characterization of PLD glass phosphate films doped with CdS. *Journal of Materials Science* **2017**, *52* (5), 2895-2901.
60. Han, S.; Liu, S. M.; Lu, Y. M.; Cao, P. J.; Liu, W. J.; Zeng, Y. X.; Jia, F.; Liu, X. K.; Zhu, D. L., High performance solar-blind ultraviolet photo detector based on

mixed-phase MgZnO thin film with different interfaces deposited by PLD method. *Journal of Alloys and Compounds* **2017**, *694*, 168-174.

61. Li, X. R.; Cao, H. Y.; Dong, Y. C.; Yue, F. Y.; Chen, Y.; Xiang, P. H.; Sun, L.; Yang, P. X.; Chu, J. H., Investigation of Cu₂ZnSnS₄ thin films with controllable Cu composition and its influence on photovoltaic properties for solar cells. *Journal of Alloys and Compounds* **2017**, *694*, 833-840.

62. Ghosh, A.; Thangavel, R.; Gupta, A., Solution-processed Cd free kesterite Cu₂ZnSnS₄ thin film solar cells with vertically aligned ZnO nanorod arrays. *Journal of Alloys and Compounds* **2017**, *694*, 394-400.

63. Hillhouse, H. W.; Beard, M. C., Solar cells from colloidal nanocrystals: Fundamentals, materials, devices, and economics. *Current Opinion in Colloid & Interface Science* **2009**, *14* (4), 245-259.

64. Zhang, Z. H.; Liu, C. Y.; Li, Z. Q.; Zhang, X. Y.; Long, Y. B.; Ruan, S. P.; Guo, W. B.; Zhang, L., Improved performance of inverted polymer solar cells using CdSSe/ZnS quantum dots. *Materials Letters* **2017**, *188*, 244-247.

65. Alivisatos, A. P., Perspectives on the physical chemistry of semiconductor nanocrystals. *Journal of Physical Chemistry* **1996**, *100* (31), 13226-13239.

66. Liu, H. C.; Duboz, J. Y.; Dudek, R.; Wasilewski, Z. R.; Fafard, S.; Finnie, P., Quantum dot infrared photodetectors. *Physica E-Low-Dimensional Systems & Nanostructures* **2003**, *17* (1-4), 631-633.

67. Nurunnabi, M.; Cho, K. J.; Choi, J. S.; Huh, K. M.; Lee, Y. H., Targeted near-IR QDs-loaded micelles for cancer therapy and imaging. *Biomaterials* **2010**, *31* (20), 5436-5444.

68. Kumar, M.; Vezzoli, S.; Wang, Z.; Chaudhary, V.; Ramanujan, R. V.; Gurzadyan, G. G.; Annalisa, B. F.; Soci, C., Hot exciton cooling and multiple exciton generation in PbSe quantum dots. *Physical Chemistry Chemical Physics* **2016**, *18* (45), 31107-31114.

69. Kang, I.; Wise, F. W., Electronic structure and optical properties of PbS and PbSe quantum dots. *Journal of the Optical Society of America B-Optical Physics* **1997**, *14* (7), 1632-1646.
70. Pichaandi, J.; van Veggel, F., Near-infrared emitting quantum dots: Recent progress on their synthesis and characterization. *Coordination Chemistry Reviews* **2014**, *263*, 138-150.
71. Du, H.; Chen, C. L.; Krishnan, R.; Krauss, T. D.; Harbold, J. M.; Wise, F. W.; Thomas, M. G.; Silcox, J., Optical properties of colloidal PbSe nanocrystals. *Nano Letters* **2002**, *2* (11), 1321-1324.
72. Wehrenberg, B. L.; Wang, C. J.; Guyot-Sionnest, P., Interband and intraband optical studies of PbSe colloidal quantum dots. *Journal of Physical Chemistry B* **2002**, *106* (41), 10634-10640.
73. Dabbousi, B. O.; RodriguezViejo, J.; Mikulec, F. V.; Heine, J. R.; Mattoussi, H.; Ober, R.; Jensen, K. F.; Bawendi, M. G., (CdSe)ZnS core-shell quantum dots: Synthesis and characterization of a size series of highly luminescent nanocrystallites. *Journal of Physical Chemistry B* **1997**, *101* (46), 9463-9475.
74. Mir, I. A.; Rawat, K.; Bohidar, H. B., Cadmium-free aqueous synthesis of ZnSe and ZnSe@ZnS core-shell quantum dots and their differential bioanalyte sensing potential. *Materials Research Express* **2016**, *3* (10).
75. Chen, Z. H.; Yeung, S. Y.; Li, H.; Qian, J. C.; Zhang, W. J.; Li, Y. Y.; Bello, I., Controlled growth of ZnO/Zn_{1-x}Pb_xSe core-shell nanowires and their interfacial electronic energy alignment. *Nanoscale* **2012**, *4* (10), 3154-3161.
76. Isarov, M.; Grumbach, N.; Maikov, G. I.; Tilchin, J.; Jang, Y.; Sashchiuk, A.; Lifshitz, E., THE EFFECT OF LOW TEMPERATURE COATING AND ANNEALING ON STRUCTURAL AND OPTICAL PROPERTIES OF CdSe/CdS CORE/SHELL QDs. *Lithuanian Journal of Physics* **2015**, *55* (4), 297-304.

77. Liu, N.; Yang, P., Hydrothermal Synthesis of High-Quality Type-II CdTe/CdSe Core/Shell Quantum Dots with Dark Red Emission. *Journal of Nanoscience and Nanotechnology* **2014**, *14* (8), 5817-5823.
78. Miszta, K.; Dorfs, D.; Genovese, A.; Kim, M. R.; Manna, L., Cation Exchange Reactions in Colloidal Branched Nanocrystals. *Acs Nano* **2011**, *5* (9), 7176-7183.
79. Akhtar, J.; Afzaal, M.; Banski, M.; Podhorodecki, A.; Syperek, M.; Misiewicz, J.; Bangert, U.; Hardman, S. J. O.; Graham, D. M.; Flavell, W. R.; Binks, D. J.; Gardonio, S.; O'Brien, P., Controlled Synthesis of Tuned Bandgap Nanodimensional Alloys of $\text{PbS}_x\text{Se}_{1-x}$. *Journal of the American Chemical Society* **2011**, *133* (14), 5602-5609.
80. Zaiats, G.; Yanover, D.; Vaxenburg, R.; Tilchin, J.; Sashchiuk, A.; Lifshitz, E., PbSe-Based Colloidal Core/Shell Heterostructures for Optoelectronic Applications. *Materials* **2014**, *7* (11), 7243-7275.
81. Pietryga, J. M.; Werder, D. J.; Williams, D. J.; Casson, J. L.; Schaller, R. D.; Klimov, V. I.; Hollingsworth, J. A., Utilizing the lability of lead selenide to produce heterostructured nanocrystals with bright, stable infrared emission. *Journal of the American Chemical Society* **2008**, *130* (14), 4879-4885.
82. Pandey, A.; Guyot-Sionnest, P., Slow Electron Cooling in Colloidal Quantum Dots. *Science* **2008**, *322* (5903), 929-932.
83. Pandey, G.; Rao, K.; Palit, D. K.; Mittal, J. P., Generation and mesolysis of PhSeSiR_3 (center dot-): Mechanistic studies by laser flash photolysis and application for bimolecular group transfer radical reactions. *Journal of Organic Chemistry* **1998**, *63* (12), 3968-3978.
84. Murray, C. B.; Sun, S. H.; Gaschler, W.; Doyle, H.; Betley, T. A.; Kagan, C. R., Colloidal synthesis of nanocrystals and nanocrystal superlattices. *Ibm Journal of Research and Development* **2001**, *45* (1), 47-56.
85. Shockley, W.; Queisser, H. J., DETAILED BALANCE LIMIT OF EFFICIENCY OF P-N JUNCTION SOLAR CELLS. *Journal of Applied Physics* **1961**, *32* (3), 510-&.

86. Hanna, M. C.; Nozik, A. J., Solar conversion efficiency of photovoltaic and photoelectrolysis cells with carrier multiplication absorbers. *Journal of Applied Physics* **2006**, *100* (7).
87. Nozik, A. J., Spectroscopy and hot electron relaxation dynamics in semiconductor quantum wells and quantum dots. *Annual Review of Physical Chemistry* **2001**, *52*, 193-231.
88. Shabaev, A.; Efros, A. L.; Nozik, A. J., Multiexciton generation by a single photon in nanocrystals. *Nano Letters* **2006**, *6* (12), 2856-2863.
89. Schaller, R. D.; Agranovich, V. M.; Klimov, V. I., High-efficiency carrier multiplication through direct photogeneration of multi-excitons via virtual single-exciton states. *Nature Physics* **2005**, *1* (3), 189-194.
90. Rupasov, V. I.; Klimov, V. I., Carrier multiplication in semiconductor nanocrystals via intraband optical transitions involving virtual biexciton states. *Physical Review B* **2007**, *76* (12), 6.
91. Nozik, A. J., Quantum dot solar cells. *Physica E-Low-Dimensional Systems & Nanostructures* **2002**, *14* (1-2), 115-120.
92. Schaller, R. D.; Klimov, V. I., High efficiency carrier multiplication in PbSe nanocrystals: Implications for solar energy conversion. *Physical Review Letters* **2004**, *92* (18), 4.
93. Cho, B.; Peters, W. K.; Hill, R. J.; Courtney, T. L.; Jonas, D. M., Bulklike Hot Carrier Dynamics in Lead Sulfide Quantum Dots. *Nano Letters* **2010**, *10* (7), 2498-2505.
94. Trinh, M. T.; Limpens, R.; de Boer, W.; Schins, J. M.; Siebbeles, L. D. A.; Gregorkiewicz, T., Direct generation of multiple excitons in adjacent silicon nanocrystals revealed by induced absorption. *Nature Photonics* **2012**, *6* (5), 316-321.

95. Timmerman, D.; Izeddin, I.; Stallinga, P.; Yassievich, I. N.; Gregorkiewicz, T., Space-separated quantum cutting with silicon nanocrystals for photovoltaic applications. *Nature Photonics* **2008**, *2* (2), 105-109.
96. Schaller, R. D.; Sykora, M.; Pietryga, J. M.; Klimov, V. I., Seven excitons at a cost of one: Redefining the limits for conversion efficiency of photons into charge carriers. *Nano Letters* **2006**, *6* (3), 424-429.
97. Beard, M. C.; Luther, J. M.; Midgett, A. G.; Semonin, O. E.; Johnson, J. C.; Nozik, A. J.; Ieee, THIRD GENERATION PHOTOVOLTAICS: MULTIPLE EXCITON GENERATION IN COLLOIDAL QUANTUM DOTS, QUANTUM DOT ARRAYS, AND QUANTUM DOT SOLAR CELLS. In *35th Ieee Photovoltaic Specialists Conference*, 2010; pp 370-375.
98. Shabaev, A.; Hellberg, C. S.; Efros, A. L., Efficiency of Multiexciton Generation in Colloidal Nanostructures. *Accounts of Chemical Research* **2013**, *46* (6), 1242-1251.
99. Cunningham, P. D.; Boercker, J. E.; Foos, E. E.; Lumb, M. P.; Smith, A. R.; Tischler, J. G.; Melinger, J. S., Enhanced Multiple Exciton Generation in Quasi-One-Dimensional Semiconductors. *Nano Letters* **2011**, *11* (8), 3476-3481.
100. Aerts, M.; Bielewicz, T.; Klinke, C.; Grozema, F. C.; Houtepen, A. J.; Schins, J. M.; Siebbeles, L. D. A., Highly efficient carrier multiplication in PbS nanosheets. *Nature Communications* **2014**, *5*.
101. Rowland, C. E.; Fedin, I.; Zhang, H.; Gray, S. K.; Govorov, A. O.; Talapin, D. V.; Schaller, R. D., Picosecond energy transfer and multiexciton transfer outpaces Auger recombination in binary CdSe nanoplatelet solids. *Nature Materials* **2015**, *14* (5), 484-489.
102. Faraday, M., The Bakerian Lecture: Experimental Relations of Gold (and Other Metals) to Light. *Philos. Trans.* **1857**, *147*, 145-181.
103. Schwartzberg, A. M.; Zhang, J. Z., Novel optical properties and emerging applications of metal nanostructures. *Journal of Physical Chemistry C* **2008**, *112* (28), 10323-10337.

104. Mie, G., Articles on the optical characteristics of turbid tubes, especially colloidal metal solutions. *Annalen Der Physik* **1908**, 25 (3), 377-445.
105. Liz-Marzan, L. M., Nanometals formation and color. *Materials Today* **2004**, 7 (2), 26-31.
106. Garnett, J. C. M., Colours in Metal Glasses, in Metallic Films, and in Metallic Solutions. II. *Philos. Trans. R. Soc. London* **1904**, 205, 385.
107. Thapaliya, E. R.; Raymo, F. M.; Garcia-Amoros, J., Fluorescence activation with the plasmonic assistance of silver nanoparticles. *Inorganica Chimica Acta* **2017**, 468, 82-90.
108. Das, G. M.; Ringne, A. B.; Dantham, V. R.; Easwaran, R. K.; Laha, R., Numerical investigations on photonic nanojet mediated surface enhanced Raman scattering and fluorescence techniques. *Optics Express* **2017**, 25 (17), 19822-19831.
109. Lu, Y.; Liu, G. L.; Lee, L. P., High-density silver nanoparticle film with temperature-controllable interparticle spacing for a tunable surface enhanced Raman scattering substrate. *Nano Letters* **2005**, 5 (1), 5-9.
110. Shen, C. M.; Hui, C.; Yang, T. Z.; Xiao, C. W.; Tian, J. F.; Bao, L. H.; Chen, S. T.; Ding, H.; Gao, H. J., Monodisperse Noble-Metal Nanoparticles and Their Surface Enhanced Raman Scattering Properties. *Chemistry of Materials* **2008**, 20 (22), 6939-6944.
111. Du, H.; Disney, M. D.; Miller, B. L.; Krauss, T. D., Hybridization-based unquenching of DNA hairpins on Au surfaces: Prototypical "molecular beacon" biosensors. *Journal of the American Chemical Society* **2003**, 125 (14), 4012-4013.
112. Tawa, K.; Nakayama, T.; Kintaka, K., Optimal Structure of a Plasmonic Chip for Sensitive Bio-Detection with the Grating-Coupled Surface Plasmon-Field Enhanced Fluorescence (GC-SPF). *Materials* **2017**, 10 (9).

113. Anker, J. N.; Hall, W. P.; Lyandres, O.; Shah, N. C.; Zhao, J.; Van Duyne, R. P., Biosensing with plasmonic nanosensors. *Nature Materials* **2008**, *7* (6), 442-453.
114. Liedberg, B.; Nylander, C.; Lundstrom, I., SURFACE-PLASMON RESONANCE FOR GAS-DETECTION AND BIOSENSING. *Sensors and Actuators* **1983**, *4* (2), 299-304.
115. Kabashin, A. V.; Evans, P.; Pastkovsky, S.; Hendren, W.; Wurtz, G. A.; Atkinson, R.; Pollard, R.; Podolskiy, V. A.; Zayats, A. V., Plasmonic nanorod metamaterials for biosensing. *Nature Materials* **2009**, *8* (11), 867-871.
116. Wang, Y. H.; Ge, S. G.; Zhang, L. N.; Yu, J. H.; Yan, M.; Huang, J. D., Visible photoelectrochemical sensing platform by in situ generated CdS quantum dots decorated branched-TiO₂ nanorods equipped with Prussian blue electrochromic display. *Biosensors & Bioelectronics* **2017**, *89*, 859-865.
117. Selvan, S. T.; Tan, T. T. Y.; Yi, D. K.; Jana, N. R., Functional and Multifunctional Nanoparticles for Bioimaging and Biosensing. *Langmuir* **2010**, *26* (14), 11631-11641.
118. Bardhan, R.; Lal, S.; Joshi, A.; Halas, N. J., Theranostic Nanoshells: From Probe Design to Imaging and Treatment of Cancer. *Accounts of Chemical Research* **2011**, *44* (10), 936-946.
119. Sharma, P.; Brown, S.; Walter, G.; Santra, S.; Moudgil, B., Nanoparticles for bioimaging. *Advances in Colloid and Interface Science* **2006**, *123*, 471-485.
120. Gu, X. F.; Qiu, T.; Zhang, W. J.; Chu, P. K., Light-emitting diodes enhanced by localized surface plasmon resonance. *Nanoscale Research Letters* **2011**, *6*.
121. Cho, C. Y.; Kwon, M. K.; Lee, S. J.; Han, S. H.; Kang, J. W.; Kang, S. E.; Lee, D. Y.; Park, S. J., Surface plasmon-enhanced light-emitting diodes using silver nanoparticles embedded in p-GaN. *Nanotechnology* **2010**, *21* (20).

122. Sergelen, K.; Liedberg, B.; Knoll, W.; Dostalek, J., A surface plasmon field-enhanced fluorescence reversible split aptamer biosensor. *Analyst* **2017**, *142* (16), 2995-3001.
123. Johansson, P.; Xu, H. X.; Kall, M., Surface-enhanced Raman scattering and fluorescence near metal nanoparticles. *Physical Review B* **2005**, *72* (3).
124. Wang, Y.; Wu, L.; Wong, T. I.; Bauch, M.; Zhang, Q. W.; Zhang, J. L.; Liu, X. H.; Zhou, X. D.; Bai, P.; Dostalek, J.; Liedberg, B., Directional fluorescence emission co-enhanced by localized and propagating surface plasmons for biosensing. *Nanoscale* **2016**, *8* (15), 8008-8016.
125. He, J.; Wang, S.; Chen, J. W.; Wu, F.; Dai, J. N.; Long, H. L.; Zhang, Y.; Zhang, W.; Feng, Z. C.; Zhang, J.; Du, S. D.; Ye, L.; Chen, C. Q., Localized surface plasmon enhanced deep UV-emitting of AlGaIn based multi-quantum wells by Al nanoparticles on SiO₂ dielectric interlayer. *Nanotechnology* **2018**, *29* (19).
126. Meng, Y.; Wu, X. Y.; Xiong, Z. Y.; Lin, C. Y.; Xiong, Z. H.; Blount, E.; Chen, P., Electrode quenching control for highly efficient CsPbBr₃ perovskite light-emitting diodes via surface plasmon resonance and enhanced hole injection by Au nanoparticles. *Nanotechnology* **2018**, *29* (17).
127. Chandrakalavathi, T.; Peta, K. R.; Jeyalakshmi, R., Enhanced UV photoresponse with Au nanoparticles incorporated rGO/Si heterostructure. *Materials Research Express* **2018**, *5* (2).
128. Deng, L. L.; Zhou, Z. J.; Jia, B. L.; Zhou, H. W.; Peng, L.; Shang, W. J.; Feng, J.; Chen, S. F., Improved electron injection and efficiency in blue organic light-emitting diodes using coupled electric field near cathode. *Organic Electronics* **2018**, *53*, 346-352.
129. Kinkhabwala, A.; Yu, Z.; Fan, S.; Avlasevich, Y.; Muellen, K.; Moerner, W. E., Large single-molecule fluorescence enhancements produced by a bowtie nanoantenna. *Nature Photonics* **2009**, *3* (11), 654-657.

130. Yuan, H. F.; Khatua, S.; Zijlstra, P.; Yorulmaz, M.; Orrit, M., Thousand-fold Enhancement of Single-Molecule Fluorescence Near a Single Gold Nanorod. *Angewandte Chemie-International Edition* **2013**, *52* (4), 1217-1221.
131. Gerber, S.; Reil, F.; Hohenester, U.; Schlagenhaufen, T.; Krenn, J. R.; Leitner, A., Tailoring light emission properties of fluorophores by coupling to resonance-tuned metallic nanostructures. *Physical Review B* **2007**, *75* (7).
132. Li, X. H.; Choy, W. C. H.; Huo, L. J.; Xie, F. X.; Sha, W. E. I.; Ding, B. F.; Guo, X.; Li, Y. F.; Hou, J. H.; You, J. B.; Yang, Y., Dual Plasmonic Nanostructures for High Performance Inverted Organic Solar Cells. *Advanced Materials* **2012**, *24* (22), 3046-3052.
133. Wang, D. H.; Kim, D. Y.; Choi, K. W.; Seo, J. H.; Im, S. H.; Park, J. H.; Park, O. O.; Heeger, A. J., Enhancement of Donor-Acceptor Polymer Bulk Heterojunction Solar Cell Power Conversion Efficiencies by Addition of Au Nanoparticles. *Angewandte Chemie-International Edition* **2011**, *50* (24), 5519-5523.
134. Kislov, D. A., Effect of plasmonic silver nanoparticles on the photovoltaic properties of Graetzel solar cells. In *4th International Conference of Photonics and Information Optics, Phio 2015*, Evtikhiev, N. N., Ed. 2015; Vol. 73, pp 114-120.
135. He, J. W.; Li, S. S.; Xu, K. L.; Tang, B.; Yang, H. Q.; Wang, Q.; Li, H., Binding properties of the natural red dye carthamin with human serum albumin: Surface plasmon resonance, isothermal titration microcalorimetry, and molecular docking analysis. *Food Chemistry* **2017**, *221*, 650-656.
136. Smith, S. J.; Purcell, E. M., VISIBLE LIGHT FROM LOCALIZED SURFACE CHARGES MOVING ACROSS A GRATING. *Physical Review* **1953**, *92* (4), 1069-1069.
137. Haerberle, O., Reciprocity theorem for Smith-Purcell radiation. *Optics Communications* **1997**, *141* (5-6), 237-242.

138. Gerard, J. M.; Sermage, B.; Gayral, B.; Legrand, B.; Costard, E.; Thierry-Mieg, V., Enhanced spontaneous emission by quantum boxes in a monolithic optical microcavity. *Physical Review Letters* **1998**, *81* (5), 1110-1113.
139. Cai, B. Y.; Li, X. P.; Zhang, Y. N.; Jia, B. H., Significant light absorption enhancement in silicon thin film tandem solar cells with metallic nanoparticles. *Nanotechnology* **2016**, *27* (19).
140. Wang, S. J.; Zhang, B. P., SPR propelled visible-active photocatalysis on Au-dispersed Co₃O₄ films. *Applied Catalysis a-General* **2013**, *467*, 585-592.
141. Katerski, A.; Karber, E.; Acik, I. O.; Dolgov, L.; Mere, A.; Sildos, I.; Mikli, V.; Krunk, M., Modification of light absorption in thin CuInS₂ films by sprayed Au nanoparticles. *Nanoscale Research Letters* **2014**, *9*.
142. Beck, F. J.; Polman, A.; Catchpole, K. R., Tunable light trapping for solar cells using localized surface plasmons. *Journal of Applied Physics* **2009**, *105* (11).
143. Blake, P.; Obermann, J.; Harbin, B.; Roper, D. K., Enhanced Nanoparticle Response From Coupled Dipole Excitation for Plasmon Sensors. *Ieee Sensors Journal* **2011**, *11* (12), 3332-3340.
144. Willett, D. R.; Chumanov, G., LSPR Sensor Combining Sharp Resonance and Differential Optical Measurements. *Plasmonics* **2014**, *9* (6), 1391-1396.
145. Gunnarsson, L.; Rindzevicius, T.; Prikulis, J.; Kasemo, B.; Kall, M.; Zou, S. L.; Schatz, G. C., Confined plasmons in nanofabricated single silver particle pairs: Experimental observations of strong interparticle interactions. *Journal of Physical Chemistry B* **2005**, *109* (3), 1079-1087.
146. Liu, X. O.; Atwater, M.; Wang, J. H.; Huo, Q., Extinction coefficient of gold nanoparticles with different sizes and different capping ligands. *Colloids and Surfaces B-Biointerfaces* **2007**, *58* (1), 3-7.

147. Yu, W. W.; Qu, L. H.; Guo, W. Z.; Peng, X. G., Experimental determination of the extinction coefficient of CdTe, CdSe and CdS nanocrystals (vol 15, pg 2854, 2003). *Chemistry of Materials* **2004**, *16* (3), 560-560.
148. Manai, L.; Rezgui, B. D.; Bou, A.; Barakel, D.; Torchio, P.; Zaghouani, R. B.; Palais, O.; Bessais, B., Enhanced light trapping using plasmonic nanoparticles. In *Tunisia-Japan Symposium: R&D of Energy and Material Sciences for Sustainable Society*, Akimoto, K.; Suzuki, Y.; Islam, M. M., Eds. 2015; Vol. 596.
149. Stuart, H. R.; Hall, D. G., Island size effects in nanoparticle-enhanced photodetectors. *Applied Physics Letters* **1998**, *73* (26), 3815-3817.
150. Geddes, C. D.; Lakowicz, J. R., Metal-enhanced fluorescence. *Journal of Fluorescence* **2002**, *12* (2), 121-129.
151. Lakowicz, J. R., Radiative decay engineering 5: metal-enhanced fluorescence and plasmon emission. *Analytical Biochemistry* **2005**, *337* (2), 171-194.
152. Sharma, A.; Khanna, R., Pattern formation in unstable thin liquid films. *Physical Review Letters* **1998**, *81* (16), 3463-3466.
153. Haynes, C. L.; Van Duyne, R. P., Nanosphere lithography: A versatile nanofabrication tool for studies of size-dependent nanoparticle optics. *Journal of Physical Chemistry B* **2001**, *105* (24), 5599-5611.
154. Ott, A.; Ring, S.; Yin, G.; Calvet, W.; Stannowski, B.; Lu, Y.; Schlatmann, R.; Ballauff, M., Efficient plasmonic scattering of colloidal silver particles through annealing-induced changes. *Nanotechnology* **2014**, *25* (45).
155. Fitzgerald, J. P. S.; Karg, M., Plasmon resonance coupling phenomena in self-assembled colloidal monolayers. *Physica Status Solidi a-Applications and Materials Science* **2017**, *214* (8).

156. Zhang, J.; Fu, Y.; Chowdhury, M. H.; Lakowicz, J. R., Plasmon-coupled fluorescence probes: Effect of emission wavelength on fluorophore-labeled silver particles. *Journal of Physical Chemistry C* **2008**, *112* (25), 9172-9180.
157. Dey, S.; Zhou, Y.; Tian, X.; Jenkins, J. A.; Chen, O.; Zou, S.; Zhao, J., An experimental and theoretical mechanistic study of biexciton quantum yield enhancement in single quantum dots near gold nanoparticles. *Nanoscale* **2015**, *7* (15), 6851-6858.
158. Fu, Y.; Zhang, J.; Lakowicz, J. R., Large enhancement of single molecule fluorescence by coupling to hollow silver nanoshells. *Chemical Communications* **2012**, *48* (78), 9726-9728.
159. LeBlanc, S. J.; McClanahan, M. R.; Jones, M.; Moyer, P. J., Enhancement of Multiphoton Emission from Single CdSe Quantum Dots Coupled to Gold Films. *Nano Letters* **2013**, *13* (4), 1662-1669.
160. Shaik, F.; Peer, I.; Jain, P. K.; Amirav, L., Plasmon-Enhanced Multicarrier Photocatalysis. *Nano Letters* **2018**, *18* (7), 4370-4376.
161. Achermann, M., Exciton-Plasmon Interactions in Metal-Semiconductor Nanostructures. *Journal of Physical Chemistry Letters* **2010**, *1* (19), 2837-2843.
162. Amirav, L.; Alivisatos, A. P., Photocatalytic Hydrogen Production with Tunable Nanorod Heterostructures. *Journal of Physical Chemistry Letters* **2010**, *1* (7), 1051-1054.
163. Aouani, H.; Itzhakov, S.; Gachet, D.; Devaux, E.; Ebbesen, T. W.; Rigneault, H.; Oron, D.; Wenger, J., Colloidal Quantum Dots as Probes of Excitation Field Enhancement in Photonic Antennas. *Acs Nano* **2010**, *4* (8), 4571-4578.
164. Bermudez Urena, E.; Kreuzer, M. P.; Itzhakov, S.; Rigneault, H.; Quidant, R.; Oron, D.; Wenger, J., Excitation Enhancement of a Quantum Dot Coupled to a Plasmonic Antenna. *Advanced Materials* **2012**, *24* (44), OP314-+.
165. Dey, S.; Zhao, J., Plasmonic Effect on Exciton and Multiexciton Emission of Single Quantum Dots. *Journal of Physical Chemistry Letters* **2016**, *7* (15), 2921-2929.

166. Zhang, J. T.; Tang, Y.; Lee, K.; Min, O. Y., Nonepitaxial Growth of Hybrid Core-Shell Nanostructures with Large Lattice Mismatches. *Science* **2010**, *327* (5973), 1634-1638.
167. Tobias, A.; Qing, S.; Jones, M., Synthesis, Characterization, and Functionalization of Hybrid Au/CdS and Au/ZnS Core/Shell Nanoparticles. *Jove-Journal of Visualized Experiments* **2016**, (109).
168. Lee, D.; Kim, W. D.; Lee, S.; Bae, W. K.; Lee, S.; Lee, D. C., Direct Cd-to-Pb Exchange of CdSe Nanorods into PbSe/CdSe Axial Heterojunction Nanorods. *Chemistry of Materials* **2015**, *27* (15), 5295-5304.
169. Zhang, Y.; Dai, Q. Q.; Li, X. B.; Cui, Q. Z.; Gu, Z. Y.; Zou, B.; Wang, Y. D.; Yu, W. W., Formation of PbSe/CdSe Core/Shell Nanocrystals for Stable Near-Infrared High Photoluminescence Emission. *Nanoscale Research Letters* **2010**, *5* (8), 1279-1283.
170. Jeon, C. H.; Lee, Y. S.; Yee, K. J.; Han, J. K.; Bu, S. D., Strain effect on the visible emission in PbTiO₃ nanotubes: Template and wall-thickness dependence. *Current Applied Physics* **2015**, *15* (2), 115-119.
171. Jiang, Z. J.; Kelley, D. F., Stranski-Krastanov Shell Growth in ZnTe/CdSe Core/Shell Nanocrystals. *Journal of Physical Chemistry C* **2013**, *117* (13), 6826-6834.
172. Gong, K.; Kelley, D. F., Lattice Strain Limit for Uniform Shell Deposition in Zincblende CdSe/CdS Quantum Dots. *Journal of Physical Chemistry Letters* **2015**, *6* (9), 1559-1562.
173. Polte, J., Fundamental growth principles of colloidal metal nanoparticles - a new perspective. *Crystengcomm* **2015**, *17* (36), 6809-6830.
174. Grillet, N.; Manchon, D.; Cottancin, E.; Bertorelle, F.; Bonnet, C.; Broyer, M.; Lerme, J.; Pellarin, M., Photo-Oxidation of Individual Silver Nanoparticles: A Real-Time Tracking of Optical and Morphological Changes. *Journal of Physical Chemistry C* **2013**, *117* (5), 2274-2282.

175. Zhang, J. B.; Gao, J. B.; Church, C. P.; Miller, E. M.; Luther, J. M.; Klimov, V. I.; Beard, M. C., PbSe Quantum Dot Solar Cells with More than 6% Efficiency Fabricated in Ambient Atmosphere. *Nano Letters* **2014**, *14* (10), 6010-6015.
176. de Arquer, F. P. G.; Beck, F. J.; Konstantatos, G., Absorption Enhancement in Solution Processed Metal-Semiconductor Nanocomposites. *Optics Express* **2011**, *19* (21), 21038-21049.
177. Lee, J. Y.; Peumans, P., The origin of enhanced optical absorption in solar cells with metal nanoparticles embedded in the active layer. *Optics Express* **2010**, *18* (10), 10078-10087.
178. Ahn, K. J., Enhanced photon absorption of organic solar cells by three-dimensional metallic structures. *Journal of the Korean Physical Society* **2015**, *67* (12), 2101-2104.
179. Tobias, A. K.; Jones, M., Metal-Enhanced Fluorescence from Quantum Dot-Coupled Gold Nanoparticles. *Journal of Physical Chemistry C* **2019**, *123* (2), 1389-1397.
180. Singh, G.; Guericke, M. A.; Song, Q.; Jones, M., A Multipulse Time-Resolved Fluorescence Method for Probing Second-Order Recombination Dynamics in Colloidal Quantum Dots. *Journal of Physical Chemistry C* **2014**, *118* (26), 14692-14702.